Engineering Organic and Perovskite based Solar Cells

A dissertation submitted in partial fulfilment of requirements for the degree of

Doctor of Philosophy

by

Ritesh Kant Gupta

Roll No. 166153004

Centre for Nanotechnology

Indian Institute of Technology Guwahati

Guwahati-781039, Assam, India

September 2021

Statement

I do hereby declare that the work incorporated in this thesis entitled, "**Engineering Organic and Perovskite based Solar Cells**" is the result of investigations carried out by me under the guidance of Prof. Parameswar Krishnan Iyer, at the Centre for Nanotechnology, Indian Institute of Technology Guwahati, Guwahati, Assam, India.

In keeping with the general practice of reporting scientific observations, due acknowledgements have been made wherever the work described is based on the findings of other investigators. I further declare that this work has not been submitted in part or full to any other university or institute for award of any degree or diploma.

Ritesh Kant Gupta

IIT Guwahati — Ritesh Kant Gupta

September 2021

Dr. Parameswar K. Iyer
Professor, Department of Chemistry and
Center for Nanotechnology
Indian Institute of Technology Guwahati
Guwahati-781039, Assam, India
http://www.iitg.ac.in/chemistry/fac/pki/

Phone : +91-361-2582314
Fax : +91-361-2690762
:+91-361-2582349
E-mail: pki@iitg.ac.in

Certificate

This is to certify that the work included in this thesis entitled "**Engineering Organic and Perovskite based Solar Cells**" by Mr. Ritesh Kant Gupta, Centre for Nanotechnology, Indian Institute of Technology Guwahati has been carried out under my supervision. I further certify that this work has not been submitted to any other University or Institution in part or full for the award of any degree or diploma.

Place: IIT Guwahati

Date: 28 September 2021

Parameswar Krishnan Iyer

Thesis supervisor

Department of Chemistry

Indian Institute of Technology Guwahati

Guwahati – 781039, Assam, India

Dedicated to my teachers

Table of Contents

Acknowledgement

I am delighted to put across my heartfelt appreciation and gratefulness to everyone who in one way or the other have contributed in the completion of this thesis. Many individuals have supported me in this truly unforgettable and amazing journey. I have tried to list everyone who have sincerely helped and guided me in the completion of this thesis. I thank each person from the bottom of my heart.

First of all, I am extremely beholden to my supervisor and mentor Prof. Parameswar Krishnan Iyer for providing me a precious opportunity to work in his group. His continuous support, valuable suggestions, scientific guidance, deep insights, and motivation have encouraged me to take up the tasks and introduced me to a field that I knew little about. I earnestly thank him for having trust in me and giving me total freedom in choosing the direction of my research. I feel fortunate to have him as my guide who has always motivated me with his hard work, dedication and optimism. He has been ever patient with me and was always available to provide his very useful opinion regarding my thesis work.

Besides my supervisor, I am highly indebted to my doctoral committee members, Dr. Partho Sarathi Gooh Pattader, Prof. Perumal Alagarsamy, Dr. Kalyan Raidongia and Dr. Uday Narayan Maiti for assessing my research work regularly. Their invaluable suggestions and crucial comments during all my seminars helped me broaden my research from various perspectives and improve my thesis.

My sincere thanks also goes to Dr. Arun Tej M., Department of EEE, IIT Guwahati. I found him available whenever I was having a query related to the charge transport kinetics of any electronic devices. Also, timely advices and remarks from Prof. Mohammad Qureshi, Department of Chemistry, IIT Guwahati, on the experiment techniques were very useful in understanding them better.

I sincerely express my gratitude towards all my teachers especially Mrs Sumita Pal (Miss), Mrs Arpita Majumder (Didi), Mr. Kalyan Ashish Khan (Bhaiya), Mr. Kalyan Sinha Roy, Mr. Amitava Chatterjee, Dr. Devmalya Banerjee and Dr. Hirok Chaudhuri for imbibing good values and knowledge in me.

I am also thankful to all the research scholars and staff of the Centre for Nanotechnology, IIT Guwahati for their kind cooperation and support. Further, I am grateful to Department of Chemistry and Central Instrument Facility, IIT Guwahati for allowing me to access their facility for the various experimentations as and when required. I am indebted to the staff of Student Affairs, Academic Affairs and Finance sections of IIT Guwahati for being kind enough to advise and help in their respective roles. I also appreciate the efforts of Pathak Ji, Core 1 Xerox Centre, and his staff, Haloi Da and Gautam Da, for their endless help during my stay at IIT Guwahati.

I had the best of the times working with Adil Bhaiya and Rabi who were my core solar team members. Both of them deserve the best and utmost respect for their hard work, diligence and indispensable input into the overall research work. Also, I learnt a lot from Ashish Bhaiya and Radha Bhaiya regarding various aspects of organic solar cells during my earlier days at IIT Guwahati. Further, the research experience gathered along with Anwesha, Ramesh Bhaiya and Maimur Da is also worth mentioning.

I would also like to acknowledge all my other lab mates including Sameer Bhaiya, Suresh Bhaiya, Priyanka Mam, Dip Bhaiya, Anamika Dey Madam, Gopi Bhaiya, Sayan Da, Arvin Bhaiya, Rahul Bhaiya, Raman Bhaiya, Nehal, Paromita, Retwik, Biki, Raj, Priyam, Debika, Dibash, Mayur, and Geetmani Da for their timely assistance and support. I also had a great learning experience with Sahu Sir, Bikoshita, Priyanka and Swapna while they completed their summer internship project with me. I would also like to thank each one of them for creating a pleasant laboratory atmosphere and making my days memorable.

I was privileged to be part of the organizing team of ICANN2017 and ICANN2019 conferences. I had the opportunity to interact with the topmost scientists across the world and discuss my research work with them. I am extremely appreciative for the valuable inputs received from Prof. Han Young Woo, Korea University, Prof. Shyam Pandey, Kyushu Institute of Technology and Dr. Ankur Solanki, Pandit Deendayal Energy University.

I was also fortunate to be working in the Organic Electronics Laboratory of IIT Guwahati which houses all the sophisticated instruments. I have learnt a lot to keep these instruments in working conditions through proper maintenance. During all the maintenance activities, I have received ample support from various engineers. I would like to thank Mr. R.

K. Tripathi, RVL Scientific & Engineering Pvt. Ltd., Mr. T. P. Kundu, IKA India Pvt. Ltd., Mr. Subrata Sardar, Silsil International Pvt. Ltd. and Mr. M. Nandan, Bat-Sol Equipments & Technology. They have extended all possible help as and when required. Further, I am also grateful to Dr. Prasad Gosavi and Mr. Rajkumar Somendrajit Singh, Anton Paar India Pvt. Ltd. for helping me with the GIWAX measurements in the organic solar cell work.

I extend my sincere thanks to my cycling group comprising of Rahul Bhaiya, Nilanjan Da and Anwesha. All our weekend cycling trips will be one of the most memorable times that I will be taking back from IIT Guwahati. I am genuinely gratified to the moments spent with Nystha, Nirmal, Rabi, Atanu and Himangshu. All the discussions beyond work with all these friends helped me focus more on the research.

Also, I would like to thank my friends Ritwik, Kaka, Navadeep Bhai, Vivek Bhai, Suresh, Anish, and Hrishi from NIT Durgapur. All of them helped me understand the true sense of joining as a PhD student at IIT Guwahati after Masters.

Further, I acknowledge Debdipta, Sayantan, Vivek, Ankit, Aakash, Prateek and Sarbojit from the bottom of my heart. Thank you guys for helping me right from the beginning of knowing each other and provide all the moral support time and again.

Finally, I would like to express admiration towards my go to person, Sankalpita, who has spent endless number of days wishing for the bests of the world for me. I believe this is the best I could have done for her – complete a PhD. At the end, I want to thank my parents, brother and sister-in-law for their prayers, sacrifice and struggle. It is because of them I am able to live my dream and complete my higher education from a prestigious institute. They have always given me the strength to chase my dreams which was immensely needed.

I express gratitude towards each individual for extending their support, encouragement and remembering me in their prayers.

Ritesh Kant Gupta

Ritesh Kant Gupta

[This page was intentionally left blank]

Thesis Abstract

It has become utmost necessary to address the energy crisis and reduce the carbon emission simultaneously. Therefore, exploration of various renewable energy sources is now the need of the hour. Among all the renewable energy sources, solar energy is considered to be the most sustainable owing to its ample availability on the surface of earth. The first and second generations of solar cell has been already commercialized and is being utilized to reduce the load on the current method of energy production through fossil fuels. However, to further consolidate the efforts, commercial utilization of the third and fourth generations of solution processable solar cells are also important. The organic solar cell (OSC) and perovskite solar cell (PSC) are the front runners among all the solution processed photovoltaic technology owing to its various advantages and PCE reaching beyond 18% and 25% respectively. Further, both these solar cells offers ease of fabrication with low-cost and abundant materials ensuring that they can be significant contributor to commercial photovoltaic technology in the near future.

This thesis is broadly organized into two parts. The first part (comprising of one chapter) and second part (comprising of three chapters) focuses on fabrication of OSC and PSC, respectively. Two techniques have been employed in this thesis work for the fabrication of solar cells: (i) hot-casting technique in the first two working chapters, and (ii) room temperature anti-solvent method in the remaining two working chapters. At first, hot-casting technique is used to develop OSC through regulation of morphology and thickness. Highest power conversion efficiency (PCE) of 9.13% was obtained for a thick active layer film. Thereafter, hot-casting technique is again implemented to fabricated mixed-halide PSC by varying the ration of methyl ammonium bromide in the precursor solution. The modified PSC resulted in PCE of 18.08% which also displayed large micrometer sized grain and reduced nanometer sized grain boundaries to minimize the recombination of the photo-generated charges. Further, trifluoro acetic acid is used as additive in perovskite solution to regulate the crystallization, minimize ion migration and charge recombination in PSC. As a result, champion 20.10% PCE was obtained in the modified device. Finally, p-toluene sulphonic acid is utilized to control the crystallization kinetics of the perovskite bulk and also passivate the traps. Simultaneously, polystyrene is used to increase the moisture resistance

and reduce the surface defects of the perovskite films. This dual-passivation strategy resulted in champion PCE of 20.62% with superior ambient stability.

The efforts made in this thesis highlights the usefulness of various device engineering to develop OSCs and PSCs to regulate the morphology and crystallization of the photo-active layer to achieve highly efficient, stable and repeatable solar cells. The thesis provides the basis for facilitating the commercialization of OSC and PSC in the near future.

List of Figures

List of Tables

Chapter 1

Introduction

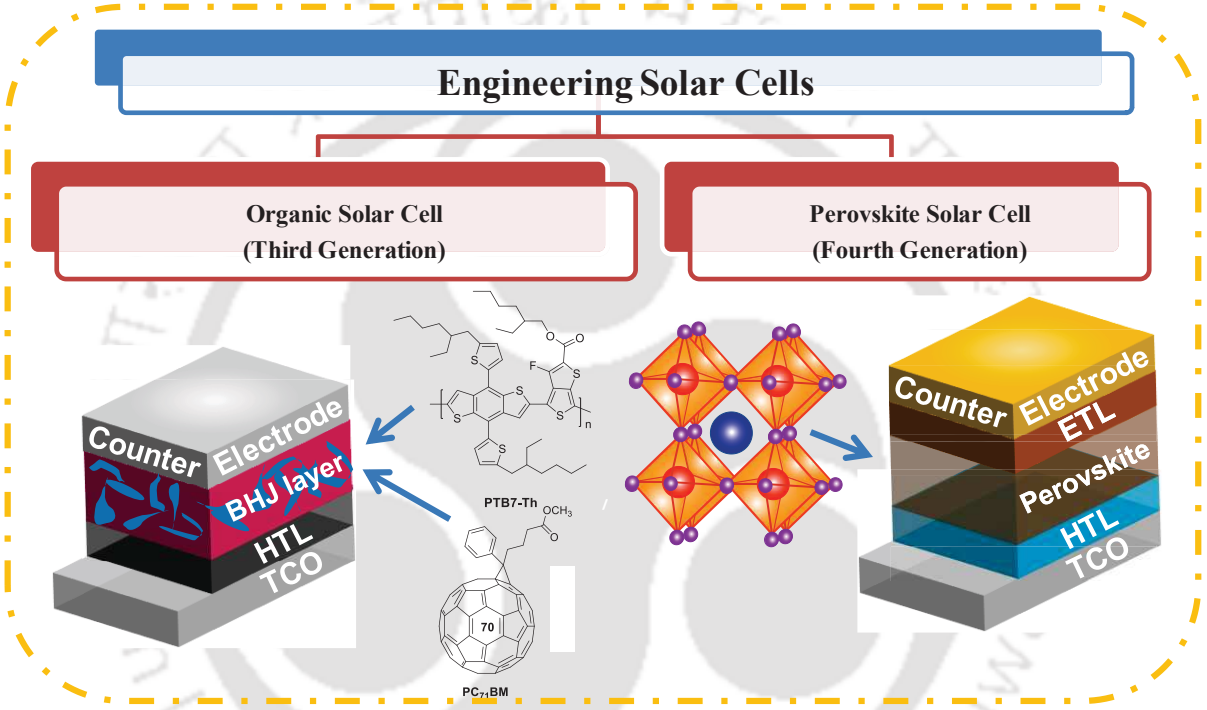

[This page was intentionally left blank]

Abstract

Today, electricity is one of the basic necessities of human beings. It is required for our entire daily needs such as lighting, entertainment, cooking food, etc. Even electricity is an indispensable necessity for improved standard of living demands development through setting up of new industries and modern transport facilities. However, most of the electricity produced these days is through fossil fuels which are limited and creates lots of pollution resulting in many cities turning inhabitable. Thus, there is an urgent need to increase the use of clean, renewable and sustainable energy sources such as solar, wind, tidal, etc. for electricity generation. Solar energy has become one of the most promising sources of energy for production of electricity and has attracted various research groups for its exploration in various ways. In this introduction chapter, the importance of solar energy exploration has been discussed. Thereafter, the history of the development of solar cells including the four generations of solar cells is covered. The various parameters to define the efficacy of any solar cells device has been explained briefly. Then, the development of organic solar cell and perovskite solar cell, which are the main focus of this thesis, has been reported. The working principle, different device architectures and various engineering aspects to improve the device performance has been discussed elaborately for few types of photovoltaic devices. Lastly, the chapter ends with a synopsis of the thesis.

1.1 Overview

With the enhancement in per capita income and lifestyle, energy sector has seen tremendous growth owing to its increasing global demand at 1.8% per annum. It is expected that, by the end of next decade, approximately 20 TW of energy would be required to fulfill all industrial, commercial, agricultural, transportation and domestic usages.[1] Currently, fossil fuels such as coal, oil and natural gas are the sources for majority of the energy production across the world. All these sources are non-renewable in nature and the increasing consumption will lead to shortage of these sources which in turn would increase the cost per unit of the energy consumption. Also, fossil fuels offer a major disadvantage by contributing to greenhouse gases which are leading to global warming and air pollution.[2] The most harmful for the environment is the energy production from coal because it has many more harmful combustion products than other sources of fossil fuels.[3, 4] Another disadvantage is extraction of these fossil fuels which causes accidents and loss of human life.[5] Currently, India is fourth in energy consumption among all countries behind Russia, United States of America and China.[6] Like all other nations which are thriving to improve its standard of living, India also depends on fossil fuels for more than 90% for its electricity generation.[7] As per a recent report in 2021, India consists of 22 polluted cities among the top 30 polluted cities in the world and most of them because of very poor air quality index.[8] This calls for a paradigm shift for the energy production technology towards renewable sources such geothermal, nuclear energy, wind, biomass and solar energy which can lead all renewable energy sources in electricity generation.

Solar energy is one of the best alternate sources of energy to power the earth. With its renewable nature and approximately 89000 TW striking the surface of the earth every year, the 20 TW projected energy requirements can be fulfilled by installing solar panels in ~0.02% area of the earth.[1] To give it a pictorial view, solar panels with area as large as Benin (a small country in Africa) or Greece will be sufficient to power all energy requirements of the world ten years later. With respect to Indian perspective, solar panels of the land area of the state of Telangana or Tamil Nadu or half of Rajasthan will be adequate to energize the world a decade later. Many countries have come together and agreed upon addressing the issue through increasing the usage of solar energy to minimize the pollution and global

climate change. Till 2017, India has attained 63% of its overall energy sufficiency and using the remaining 37% through import of direct electricity or raw materials to produce electricity.[9] The energy deficit has been planned to be minimized through the use of alternate sources as per the energy policy of India. Now, with all the villages in the country being electrified the onus has moved towards confirming that in facilitating each individual with enhanced standard of living the nature is not polluted further. This can only be done through the expedition of alternate sources of energy with primary focus on solar energy.

1.2 History of Solar Cells

Solar cells work on the principle of photovoltaic effect and hence are also referred to as photovoltaic cells. The photovoltaic effect is a process of generation of voltage or electric current in a photovoltaic cell when exposed to sunlight. It was first demonstrated by a French physicist, Edmond Becquerel, in 1839.[10] Willoughby Smith observed passage of electric current on selenium in 1873.[11] A decade later, in 1883, Charles Fritts developed the first photovoltaic cell by coating selenium with a thin layer of gold and the device was found to be ~1% efficient. This was the first rooftop solar cell installed in New York in the year 1884.[12] However, the first report on photovoltaic effect appeared only in 1948 by Kurt Lehovec. Meanwhile, Albert Einstein projected a new quantum theory of light in support of photoelectric effect and received the Nobel Prize in Physics for the same in 1921.[13] In 1946, the concept of p-n junction semiconductor solar cell was patented by Russell Ohl while working on the leads obtained for the development of transistor. Public demonstration of the first solar cell was only done in 1954 at the Bell Laboratories.[14] The first solar cell utilized crystalline silicon as the photo-active material. For the improvement of device performances many techniques were being attempted including the passivation of defects. Mohamed M. Atalia, an engineer from Egypt, showcased the method of surface passivation of silicon by thermal oxidation to improve the device efficiency in 1957.[15] In a year's time, solar cell gained enough fame that it was for the first time used in space application along with Vanguard I satellite.[16] In the 1970s, amorphous silicon was utilized for the development of solar cell to cut down on the expenses of producing pure crystalline silicon which was being utilized for fabricating solar cells. The first organic solar cell was developed in the 1980s and more than two decades later the first perovskite-based solar cell was reported.[17, 18]

1.3 Parameters to Define Solar Cell Performance

1.3.1 J-V Characterization

A typical solar cell device is first tested under illumination (AM 1.5G, 1Sun) using the current density-voltage (*J-V*) measurement which enables the determination of PCE.[19] The current density is recorded by linearly sweeping the voltage across the electrodes to obtain the *J-V* curve as shown in Figure 1.1a. The voltage sweeping can be done either in the forward direction (short circuit to open circuit condition) or reverse direction (open circuit to short circuit condition). Following parameters are estimated from the *J-V* curve:

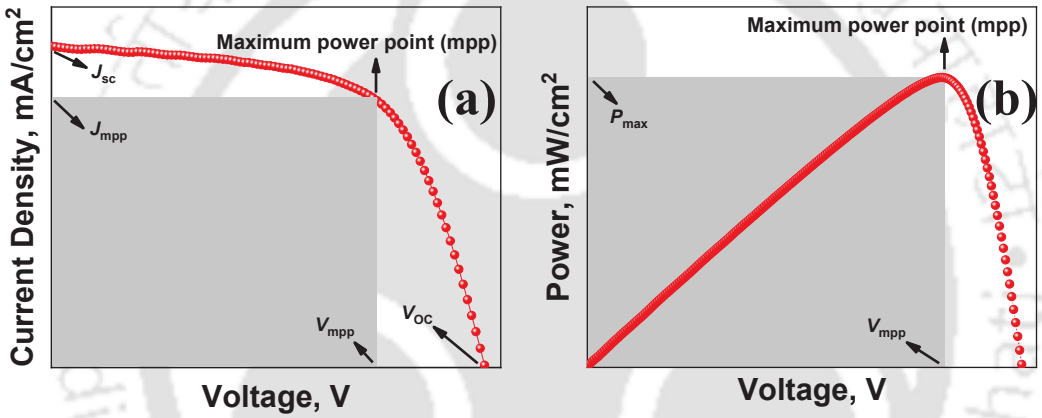

Figure 1.1: A typical example of (a) J-V curve and (b) power output versus voltage curve recorded under light illumination.

Short circuit current density (J_{sc})

The short circuit current density is obtained from the *J-V* curve at zero volt condition. It is the current per unit area that is induced directly due to the photo-generated charges. The J_{sc} value depends on the absorption properties and bandgap of the active layer, charge transportation and collection in the complete device.[20] J_{sc} is the maximum current that can be generated in a solar cell.

Open circuit voltage (V_{oc})

The open circuit voltage is determined as the potential in the device when the current flowing inside it is zero. The zero current condition arises when the photo-generated charges

equal the injected charges. It mainly depends on the built-in potential and the band positions of active layer.[21] It is the maximum voltage that can be obtained in a solar cell.

Fill factor (FF)

Fill factor is a parameter which is used to evaluate the deviation of solar cell sample efficiency from the estimated theoretical maximum power output. High value of FF indicates good quality of solar cells.[22] If the maximum power point (mpp) is known then the FF of a solar cell can be calculated using equation 1.1.

$$FF = \frac{J_{mpp}V_{mpp}}{J_{sc}V_{oc}} \qquad (1.1)$$

Power conversion efficiency (PCE, η)

The overall power conversion efficiency of a solar cell is defined as the ratio of maximum power (P_{max}) extracted from solar cell to the power of incident light (P_{in}) and can be expressed as equation 1.2:

$$PCE\ (\eta) = \frac{P_{max}}{P_{in}} = J_{sc}V_{oc}\mathrm{FF}/P_{in} \qquad (1.2)$$

The product of photocurrent and voltage at mpp (J_{mpp} x V_{mpp}) results in the maximum power (P_{max}) as illustrated in Figure 1.1b. The *J-V* curve of PSCs often depends on the scan direction resulting in hysteresis behavior. Therefore, the scan direction (V_{oc} to J_{sc} or J_{sc} to V_{oc} sweep of voltage) and the scan rate are important for obtaining reliable photovoltaic parameters.[23]

1.3.2 External Quantum Efficiency (EQE)

EQE or incident photon to current efficiency (IPCE) is a ratio of number of photons absorbed by the active layer to the number of charges (electrons and holes) getting collected at the electrodes. It is usually measured to confirm the reliability of J_{sc} obtained from *J-V* characterization. The EQE spectrum (Figure 1.2) is obtained by applying monochromatic light with continuously varying wavelength. The photocurrent at individual wavelength can be estimated; hence the area under the spectrum gives the integrated J_{sc} value. EQE of a solar cell device can be estimated using equation 1.3.

$$EQE(\lambda) = \frac{n_{electrons}(\lambda)}{n_{photons}(\lambda)} = \frac{J_{sc}(\lambda)/q}{P_{in}/hf} = \frac{h\upsilon}{q\lambda} \times \frac{J_{sc}(\lambda)}{P_{in}} = \frac{1240}{\lambda} \times \frac{J_{sc}(\lambda)}{P_{in}} \qquad (1.3)$$

where, $n_{electrons}$ & $n_{photons}$ are number of electrons & photons, respectively. *J*sc is photocurrent density in mA cm^{-2}, q stands for an elementary charge, P_{in} is the power of incident light (mW cm^{-2}), h is the Planck's constant, f is the frequency of light in vacuum (Hz), υ is the speed of light in vacuum (nm s^{-1}) and λ is the wavelength of incident light (nm). The expected short-circuit photocurrent density that is to be generated by the solar cell is calculated by integrating the product of IPCE and *J*sc (λ) over the wavelength of the incoming light.[24, 25]

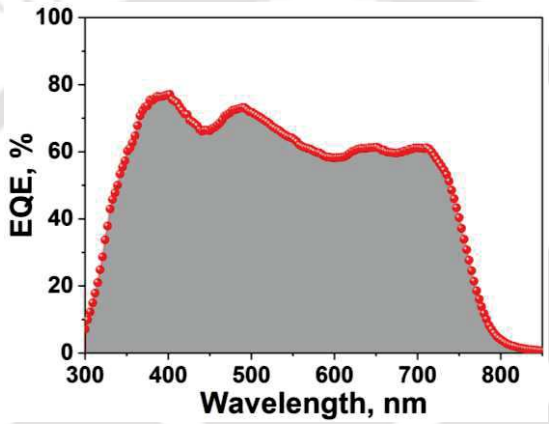

Figure 1.2: A typical EQE spectrum of a perovskite solar cell.

1.3.3 Impedance Spectroscopy Measurements

Impedance spectroscopy is a useful technique to track charge transport and recombination involved in a solar cell. The impedance spectroscopic measurement of a solar cell is performed, generally, in the frequency range of 1 Hz–1 MHz with sinusoidal voltage amplitude of 10 mV in dark condition. The impedance data can be represented in the form of either Bode plot or Nyquist plot. By fitting the impedance spectrum to equivalent circuits, many parameters such as sheet resistance, shunt resistance, charge transport resistance, recombination resistance, capacitance, and density of trap states can be estimated.[26-28]

1.4 Generations of Solar Cell

Photovoltaic technologies have come through decades of evolution and are well classified into four generations (Figure 1.3). In the first generation, solar cells were mainly

based on crystalline silicon wafers which are hundreds of micrometer thick. These solar cells are fabricated using the diffusion process of the crystalline silicon wafers. The highest PCE using the crystalline silicon have reached 27.6% in single junction and 47.1% in four-junction devices. Currently, silicon wafer based solar cells are commercially dominant and account for majority of the terrestrial solar cell industry. The reason for such a strong hold is its long payback lifetime of 25-30 years. Although this solar cell technology is commercially most viable still the production of solar grade silicon wafer is very costly, tedious and large energy consumption process. Also, the thick wafers resulted in heavier solar modules which restricted its use in space applications. Further, they generate waste in the range of thousands of metric tons which is increasing every year.[29-31]

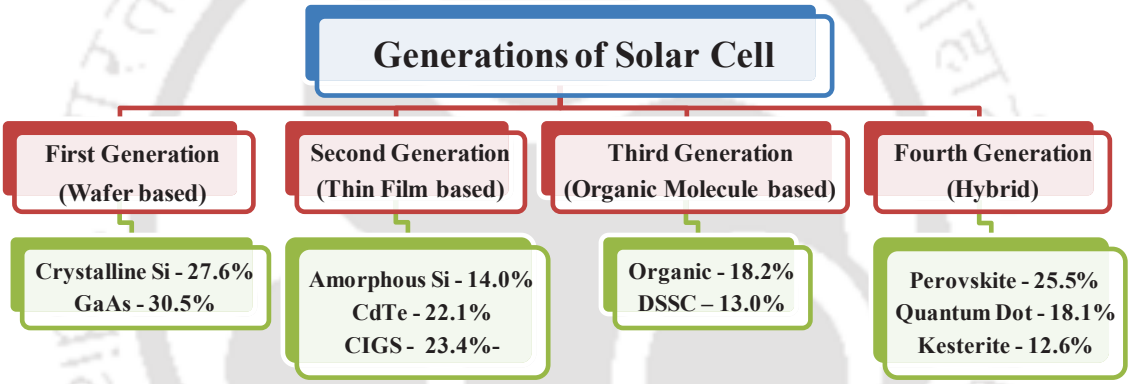

Figure 1.3: Classification of four generations of solar cell.

The drawbacks of the silicon wafer usage in solar cells directed the way to the discovery of thin film based solar cells in the second generation. In this generation amorphous silicon, CdTe and CIGS are utilized in solar cells fabrication. The cost of production for obtaining these materials for developing solar cells is less compared to crystalline silicon and since, thin films are used to generate electricity the photovoltaic cells were much cheaper than the first generation solar cells. The second generation solar cells also has comparable payback lifetime as the crystalline solar cells, but the PCE has only reached 14.0%, 22.1% and 23.4% for amorphous silicon, CdTe and CIGS, respectively. Since, thin films were being used in the development of the solar cells; the modules are light weight and finds majority of the application in space application. This materials used in the second generation are scarce elements and obtaining pure form of the materials involves

costly process as well as consumes lot of energy. Further, the waste generated from the solar modules is polluting not only earth, but also creating tons of garbage in space.[32-35]

Thereafter, the focus shifted towards having eco-friendly and inexpensive active materials in the third generation solar cells. In third generation, organic materials such as small materials and polymers are being used in the active layer of the solar cells. Polymers were considered as insulators until, in 1976, Alan J. Heegar, Alan. G. MacDiarmid and Hideki Shirakawa displayed that polyacetylene when halogenated improves conductivity by several orders.[36] They received the Nobel Prize in Chemistry for this excellent discovery in the year 2000.[37] Many conducting organic molecules were developed and they displayed similar optical and electrical properties as that of inorganic materials that were being used for solar cells in the first two generations. This led to many organic materials being utilized as active layer for polymer/organic solar cells (OSC) and Dye-sensitized solar cells (DSSC).[38, 39] These solar cell technology do not form the conventional p-n junction in the device and offers an advantage of being processed using the solution-processable technique and the cost of production is very low. They can also be fabricated on flexible substrates and hence, large-area roll-to-roll solar modules can be developed. Further, these solar cells can be easily disposed and the substrates can be recycled for future use. Since, the cost of material development and device fabrication is very less the payback lifetime for the third generation solar cells are estimated to be much shorter than the previous two generations. However, the growth of these solar cells is limited by its PCE and stability. The highest PCE of 18.2% and 13.0% has been achieved for OSC and DSSC, respectively. On the other hand development of third generation solar cells with stability of a few years is still a challenge and draws a lot of interest from various academicians and industries.[40, 41]

Finally, fourth generations of solar cells witnessed the utility of hybrid materials such as organic inorganic perovskite, quantum dots-organic, nanoparticle-organic (plasmonic) heterojunction and kesterite as active layer.[42-45] These low-cost materials also enable fabrication of solar cells on flexible a mechanically robust substrates. Perovskite solar cells (PSCs), in general, displayed characteristics similar to that of inorganic materials that were being employed in the first two generations of solar cells. Even though the stability is an issue, this fast growing technology in the field of solar cells has PCE reaching from 3% to

over 25% within a span of just over a decade. This solar cell is being tried for various commercial applications by improving its stability. Already, few reports suggest that fourth generation solar cells can be useful for space applications with short term target. The fourth generation solar cells also boast of low payback lifetime, and once the stability is significantly improved to few years this photovoltaic technology can evolve as the best alternative to inorganic solar cells.[46]

This thesis covers the fabrication of OSC from third generation and PSC from the fourth generation of solar cells. Hot-casting technique was used to fabricate OSC and PSC in the second and third chapters, respectively. The room-temperature anti solvent method was used to develop PSC in the fourth and fifth chapters.

1.5 Organic Solar Cell (OSC)

OSC belongs to the third generation of solar cells and involves organic semiconductors (polymers or small molecules) as the light absorbing photo-active layer. Generally, the organic molecules associated in the fabrication of OSC can be easily developed at very low cost and the choice of materials is available in plenty. Solution-processing technique is mostly used in the fabrication of OSCs, making the development process even cheaper even for large volumes and area. This solar cell can be fabricated on flexible substrates and hence, is much lighter in weight compared to its silicon counterpart. Since, the materials used can be easily disposed its large scale commercialization is most likely to reduce the pollution caused by the inorganic solar cells.[47, 48] OSCs utilize either a donor material (p-type) or an acceptor material (n-type) or both in various configurations as active layer. A single layer OSC consists of an organic semiconductor sandwiched in between two contacts one with higher work function and the other slightly lower work function to create the built-in potential so that the photo-generated charges can easily diffuse and gets collected at the electrodes. However, the single layer OSC offers a disadvantage of recombination of the photo-generated excitons, which are bounded holes and electrons, as their diffusion length is small and the charges recombine without reaching the electrode. The built-in potential is not enough to draw the charges towards electrodes, hence very low PCE<1% is achieved in single layer OSCs.[49, 50] Following this drawback, bilayer OSCs (planar heterojunction OSCs) were fabricated where two layers, one donor and one acceptor,

was sandwiched in between two electrodes. Different electron affinity and ionization energies of the donor and acceptor materials allowed generation of an electrostatic force at the interface. The excitons that are photo-generated near the interface can be easily separated and collected at the electrodes. However, the snag in this system was that the excitons generated away from the interface still recombined and was a loss in the photovoltaic devices. Thus, the thickness of each layer became very important in fabrication of planar heterojunction devices. Initially, the PCE was limited in bilayer OSCs, but with the development of new donor and acceptor materials the PCE has crossed 14%.[51-53] The shortcomings of these two junction types lead to the bulk heterojunction (BHJ) OSCs where the donor and acceptor materials are mixed in a fixed ratio in the solution form before utilizing it to coat the active layer.[54-56] This technique formed a nanoscale domain of the donor and acceptor materials in the film which allowed the excitons to separate at each interface easily and the loss is minimized. Among all the junction types, BHJ is most popular and PCE >18% has been achieved.

1.5.1 Working principle

The working principle of an OSC involves six important processes for converting the photon energy into electricity (Figure 1.4). The steps are: i) absorption of photons and excitations, ii) generation of excitons, iii) diffusion of excitons at the donor-acceptor interface, iv) formation of polaron, v) charge dissociation, and vi) charge transport and collection. Each steps needs to be taken care of to maximize the utility of light energy and minimize the losses to ensure high PCE of the photovoltaic device. On illumination, OSC absorbs photons from light and the active layer is excited. Thereafter, unlike inorganic solar cells, excitons are formed in the active layer which displays a binding energy of 0.1-1 eV. These bounded hole-electron pairs in the form of excitons diffuses to the interface of the donor-acceptor materials where the holes and electrons are separated. If the excitons do not diffuse to the interface the photo-generated excitons are lost through non-radiative recombination. Once the excitons reach the interface, electrons moves towards the acceptor material and donor stays in the donor forming the polaron. The charges in polarons can now be easily dissociated and the holes moves deeper in the donor material, whereas the electrons

moves deeper in the acceptor. Finally, the holes and electrons are collected at the anode and cathode, respectively.[57, 58]

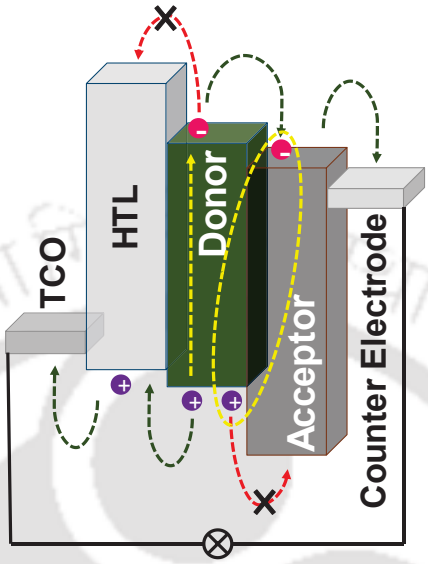

Figure 1.4: Working principle of organic solar cell.

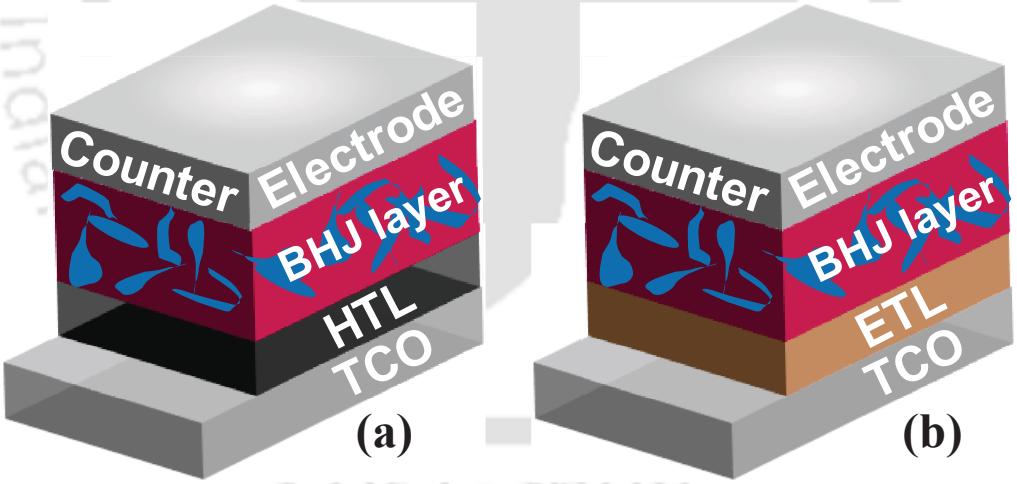

Figure 1.5: OSC device architecture (a) conventional, and (b) inverted.

1.5.2 Device architecture

All the OSC fabricated follows two kinds of device architecture: (i) conventional, and (ii) inverted as presented in Figure 1.5. The inverted device architecture was discovered first where transparent conducting oxide (TCO) is used as anode and a metal counter electrode as cathode. The photo-generated holes gets transported towards and collected at TCO, where the

electrons moves towards and gets collected at metal. However, later the flow of charges was reversed based on the selection of materials for appropriate band alignment so that the electrons gets collected at the TCO and holes at the counter metal. Thus, TCO acted as cathode and metal electrode was anode. Since, the direction of the charges were reversed, hence the name inverted device architecture. Similar charge transport mechanism is followed in both the device architectures.[59]

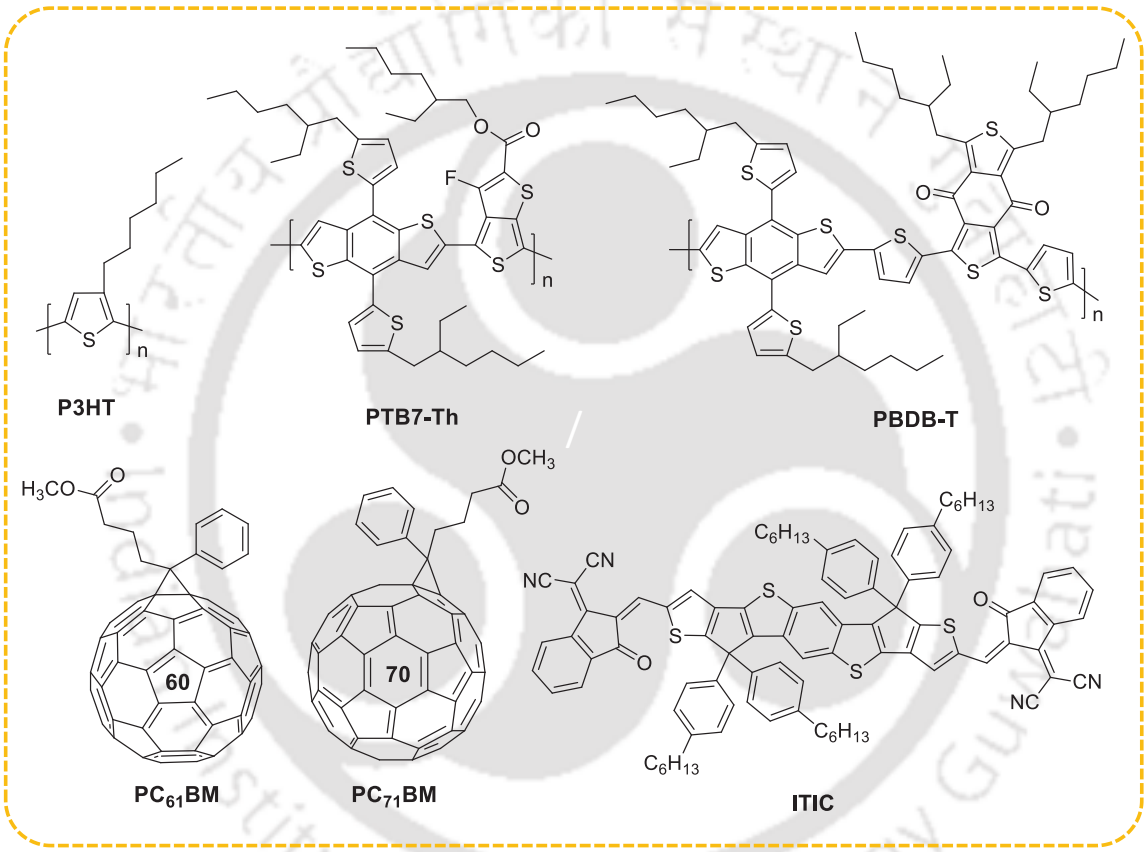

Figure 1.6: Most commonly used donor acceptor materials for OSC.

In both the device architectures various components are used namely: (i) anode, (ii) hole transport layer (HTL), (iii) active layer, (iv) electron transport layer (ETL), (v) buffer layer, and (vi) cathode. The conventional devices uses indium doped tin oxide (ITO) as anode, but some low work function metals such as copper or gold as used as anode in inverted devices. PEDOT:PSS is the most common HTL used in OSC for conventional devices. However, for conventional devices MoO_3 is the most utilized HTL.[60] The active layer for both the device architecture consists of donor and acceptor materials either

separately for bilayer devices or blended together in some ratios for BHJ devices. The most common donor materials for OSCs are P3HT, PTB7, PTB7-Th, PBDB-T, etc. The fullerene based acceptors like $PC_{61}BM$ and $PC_{71}BM$ are mostly used. However, recently some non-fullerene acceptors such as ITIC, IDIC, etc. have gained popularity.[39] A separate ETL is generally not used in conventional OSCs, but for inverted devices transparent metal oxides such as zinc oxide, tin oxide, titanium oxide, etc. are used.[61] Buffer layers are used in OSCs to further increase the transport and collection of the photo-generated charges either through band alignment or through quantum mechanical tunneling. Organic buffer layers commonly used in OSCs are bathocuproine (BCP), Bathophenanthroline (BPhen), etc. and metal buffer layers include calcium, magnesium, etc.[62] Finally, for cathode metal counter electrodes such as aluminium and silver are used for conventional devices, but for inverted devices TCOs are only used as cathode. Most commonly used active layer materials used as donor and acceptor in OSC are presented in Figure 1.6.

1.5.3 Engineering Organic Solar Cells

With the discovery of conducting polymers in 1977, the field of OSC has displayed the ability to bring down the cost of photovoltaic and also reduce the waste generation due to the inorganic solar panels. OSCs can be fabricated on low-cost solution-processable technique and can be easily integrated on flexible substrates. Short payback lifetime is another major advantage of OSC. Thorough materials and device engineering have resulted in PCE reaching beyond 18%. The most common technique to achieve good performance in an OSC device is to vary the ratio of donor and acceptor material in the blend solution for depositing the BHJ active layer. Modulating the ratio of donor and acceptor materials result in optimum domain size in nanoscale for smooth diffusion and transport of the photo-generated charges.[63, 64] Fabrication of ternary OSC through introduction of a third component (either a donor or an acceptor) bearing complementary absorption also tunes the morphology of the active layer and improves the device performance.[65, 66] The active layer is further annealed, if required, for the removal of excess solvent from the film. Solvent vapor annealing is another approach that has improved the morphology of the active layer further and improved the solar cell PCE.[67] It has been also observed that annealing, at times, leads to degrading the active layer and hence, the device performance drops. In those cases, the

annealing technique is replaced by high vacuum treatment of the active layer for removal of excess solvent from the film.[68] The transport materials have been also modified to find the adequate band alignment for the smooth collection of charges at the electrodes.[69] The processing of blend solution using various green solvents has also reduced the pollution and health issues due to the halogenated solvents. The desirable nanoscale morphology of the active layer processed using green solvents has been also achieved and the performance of the solar cell device has not been compromised.[70] Introduction of additives have also acted as morphology modifier and a small percentage have also improved and stabilized the solar cell performance.[71]

As mentioned before, that since annealing sometimes restricts the charge transport process by hampering the morphology, hence various other methodology have been attempted to improve the device performance especially in PTB7 and PTB7-Th based OSCs. One very effective technique is cooling a hot ink method where the blend solution is heated for adequate mixing of the donor and acceptor and cooling it down to a lower temperature before coating at room temperature.[72] The PCE of the device improved compared to the one which was processed through annealing. Another approach is hot-casting technique using which the blend is coated on a pre-heated substrate and do not require further annealing for evaporation of the excess solvent to achieve PCE >9%. Modulation of thickness and morphology took place by varying the hot-casting temperature. It has also been observed that annealing the active layer after hot-casting may also improve the device performance slightly.[73, 74]

Large-area and thick active layer OSCs have also been displayed by various device engineering. Techniques such as doctor blading, ink-jet printing and spray coating are very effective in fabricating large-area, flexible OSCs. The possibility of developing an OSC on a fabric has also been displayed.[75-77]

1.6 Perovskite Solar Cell (PSC)

PSCs belong to the fourth generation of solar cells and include materials in the active layer bearing similar crystal structure to that of $CaTiO_3$. The material is named after the famous Russian mineralogist L. A. Perovski.[78] The light harvesting material used for solar

cell application is mostly hybrid organic-inorganic lead or tin halide-based material. Recently, all inorganic perovskite materials are also being utilized in fabrication of solar cells. Similar to $CaTiO_3$, the photo-active material for PSC follows the ABX_3 crystal structure where A and B are cations and X is an anion (Figure 1.7). In a perovskite crystal, B and X will form a regular octahedron, BX_6, with B in the centre and A is present in the cube-octahedral void. The material offers the many advantage such as ambipolarity, wide range absorption, long diffusion length, long carrier lifetime, tunable bandgap. Alike OSCs, PSCs are also fabricated mostly using solution processing technique which makes this solar cell technology inexpensive.[44, 79, 80] The most common perovskite material used for solar cell developments is methyl ammonium lead halide ($MAPbX_3$). This was first used as sensitizer in DSSC in 2009 and resulted in a PCE of 3.8%.[18] Various developments over the last decade has resulted in PCE reaching beyond 25% and is well competing with single junction silicon solar cell.[81] Even PSCs on flexible substrates have demonstrated high efficiency >20% making this photovoltaic technology lighter in weight compared to the inorganic counterpart.[82] Generally, the active layer of a solution-processable PSC is developed from a precursor solution consisting of organic [methyl ammonium iodide (MAI), formamidinium iodide (FAI), etc.] and inorganic [lead iodide (PbI_2), tin iodide (SnI_2), etc.] materials in fixed ratio. These materials are made soluble in solvents such as dimethylformamide (DMF), γ-Butyrolactone (GBL), dimethyl sulfoxide DMSO, etc. All inorganic perovskite solar cells consists of cesium iodide (CsI) instead of the organic molecules.

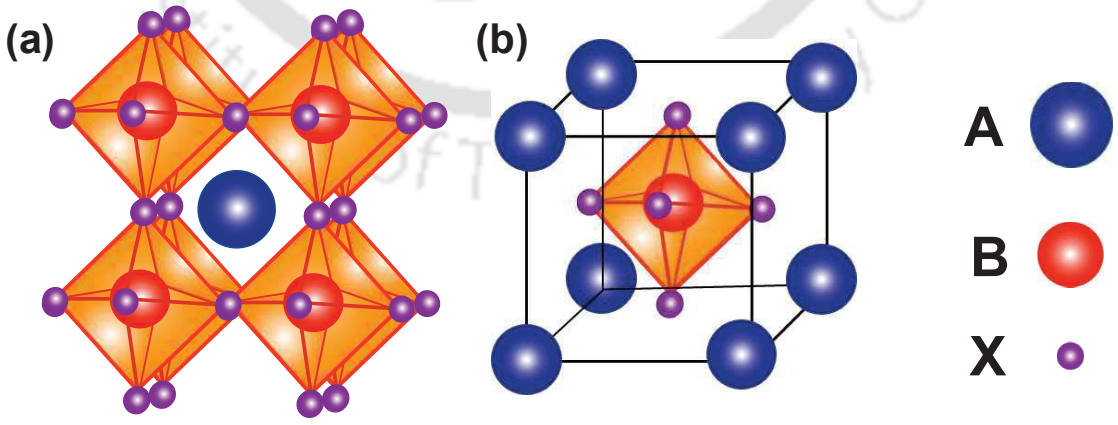

Figure 1.7 Scheme of perovskite crystal unit cell (a) A-cation centered and (b) B-cation centered.

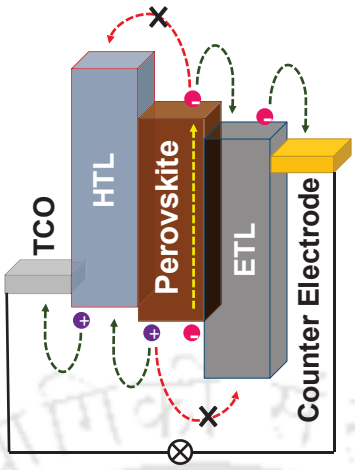

Figure 1.8: Working principle of perovskite solar cell.

1.6.1 Working Principle

Identical to silicon solar cell, the working principle of a PSC involves three important processes for converting the photon energy into electricity (Figure 1.8). The steps are: i) absorption of photons and excitations, ii) generation of charges, iii) charge transport and collection. On illumination of the solar cells, holes and electrons are generated due to absorption of the photons. The photo-generated holes move to the HTL through the HOMO level, whereas the electrons move towards the ETL through the LUMO level. Finally, these charges are collected at the respective electrodes. There is some debate regarding the formation of excitons instead of free electron-hole pairs. Few reports suggest that the lower dimensional PSCs have excitonic charge transport. Hence, in these cases first the excitons are broken into free charges and then the remaining process follows. [83]

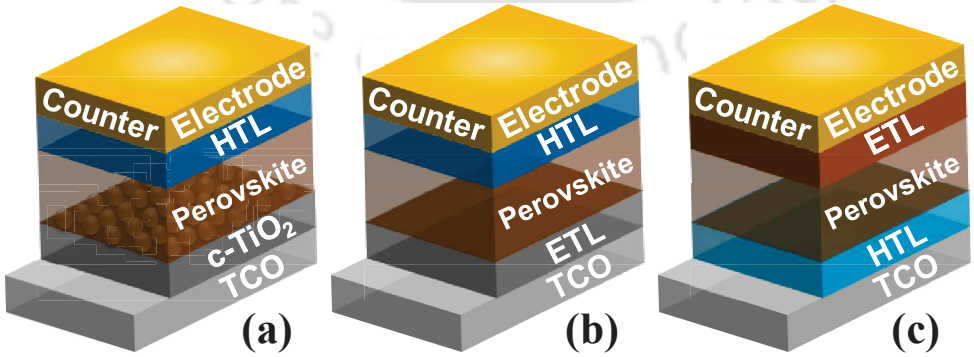

Figure 1.9: PSC device architecture (a) mesoscopic, (b) planar conventional and (c) planar inverted.

1.6.2 Device Architecture

The device architecture of PSCs is broadly classified into two types: (i) mesoscopic structure and (ii) planar heterostructure structure as presented in Figure 1.9. The mesoscopic structure facilitates infiltration of perovskite into a metal oxide layer which is mesoporous in nature. However, the ambipolarity of the perovskite material is not explored completely in this architecture. Hence, the planar heterojunction PSCs were fabricated to probe the ambipolar nature of perovskite. The planar devices are sub-classified into two types: (i) conventional (n-i-p) and (ii) inverted (p-i-n). If an n-type contact is present towards the TCO then it is said to be conventional planar device, while a p-type contact with TCO defines an inverted planar device. All the device architectures follow similar charge generation, transport and collection mechanism as explained in the working principle of PSCs.[84, 85]

The components of PSCs of varied architecture are classified similar to OSCs as: (i) anode, (ii) hole transport layer (HTL), (iii) active layer, (iv) electron transport layer (ETL), (v) buffer layer, and (vi) cathode. The mesoscopic and conventional devices use some low work function metals such as copper or gold as used as anode, while the inverted devices uses TCO such as fluorine doped tin oxide (FTO) or ITO as anode. Spiro-OMeTAD is the most common HTL used in mesoscopic and conventional devices. Since spiro-OMeTAD is expensive, many conjugated organic materials are also used as HTL in mesoscopic and conventional devices. For the inverted device, PEDOT:PSS and few conjugated polyelectrolytes are the most common HTLs that are being utilized. However, recently inorganic HTL such as NiO_x has been also explored for PSCs with improved device performance.[86, 87] The most commonly used single cation perovskite for active layer in PSCs is $MAPbX_3$ or $FAPbX_3$ or $CsPbX_3$. However, double and triple cation perovskites (consisting of MA^+, FA^+ and Cs^+ in varying ratios) have also garnered interest.[88] Mesoporous titanium oxide is the most common ETL used in mesoscopic architecture. In the conventional devices titanium oxide or tin oxide are commonly used as ETL, while the inverted devices utilizes $PC_{61}BM$ or fullerene (C_{60}) as ETL.[89-91] Like the OSCs, buffer layers are also used in PSCs to further increase the transport and collection of the photo-generated charges either through band alignment or through quantum mechanical tunneling. Buffer layers commonly used in PSCs are BCP, Rhodamine-101, etc.[88] Finally, for cathode TCOs are only used in

mesoscopic and conventional devices, while for inverted devices metal counter electrodes such as aluminium and silver are used as cathode.

1.6.3 Engineering Perovskite Solar Cell

PSCs have fascinated tremendous research interest in the field of photovoltaic technology. As already discussed before, this is due to the attractive optoelectronic properties that perovskite materials have facilitated in demonstrating PCE beyond 25% in solar cell devices. Still, the devices fabricated from the perovskite materials show stability only in the range of few hours to few days and are yet to compete with the inorganic solar cells based on the lifetime. The trap states present in the perovskite tends to accelerate the degradation process when exposed to heat, light, oxygen or UV radiation.[92-96] With PCE almost nearing the Shockley-Queisser limit, the complete focus has now mostly shifted to fabricating solar cells with improved stability under ambient conditions.[97-100] The first and foremost prerequisite to have some stability in PSCs is to fabricate perovskite films with improved crystallinity. The traps present in the perovskite crystals tend to reduce the stability. Also, the perovskite film quality is observed to increase the performance of the device.[101-103] Many techniques such as anti-solvent method, hot-casting, vacuum treatment, compositional engineering, etc. have been developed to improve the quality of perovskite films and increase its crystallinity.[104-107] Obtaining large sized crystalline grains with minimum width of grain boundaries is also a pre-requisite to further augment the stability and performance of the devices. Perovskite films with millimeter-sized grains and nanometer-sized grain boundary width have been developed to ambient stability of the device.[108] Another effective strategy to reduce the trap density of perovskite is introduction of organic molecules as passivating additive (Figure 1.10) in the precursor solution.[109-113] These molecules interact with each components of the precursor solution and control the crystallization process from the initial stages. The functional groups present in the organic molecules passivate the defects present in the perovskite layer and mitigate ion migration arising due to the presence of defects. It has also been observed that the organic molecules are coated on top of the perovskite films for adequate surface passivation. Both these techniques also result in reduced hysteresis in the forward and reverse scans of the current-voltage characteristic curve.

Another strategy to increase the stability of PSCs is to reduce the dimensionality of the perovskite crystal. The two-dimensional (2D) Ruddlesden-Popper and Dion-Jacobson perovskites have engrossed researchers to fabricate solar cell devices with even longer stability. The 2D perovskites are formed by combining large organic cations such as phenyl-ethyl ammonium (PEA), and butyl ammonium (BA) with the other components in the precursor solution. However, the PCE have only reached ~20% using these 2D perovskites due to quantum confinement effect.[114-117] Thereafter, formation of 2D/3D interface in the perovskite film has been attempted. This device engineering confirms the efficient charge transport property of the 3D perovskite and enhanced stability of the 2D perovskite. This technique has facilitated PSCs to display more than one year stability without losing much on PCE.[118] Another problem with PSCs is the lead (Pb) content as even a small amount of Pb exposure may result in severe health issues in human being including death. Thus, focus has now shifted to fabrication of Pb-free or Pb-less PSCs. The Pb-free (tin-based) PSCs have resulted in PCE ~10% and Pb-less (or less-Pb) PSCs have reached ~19% PCE.[119-123]

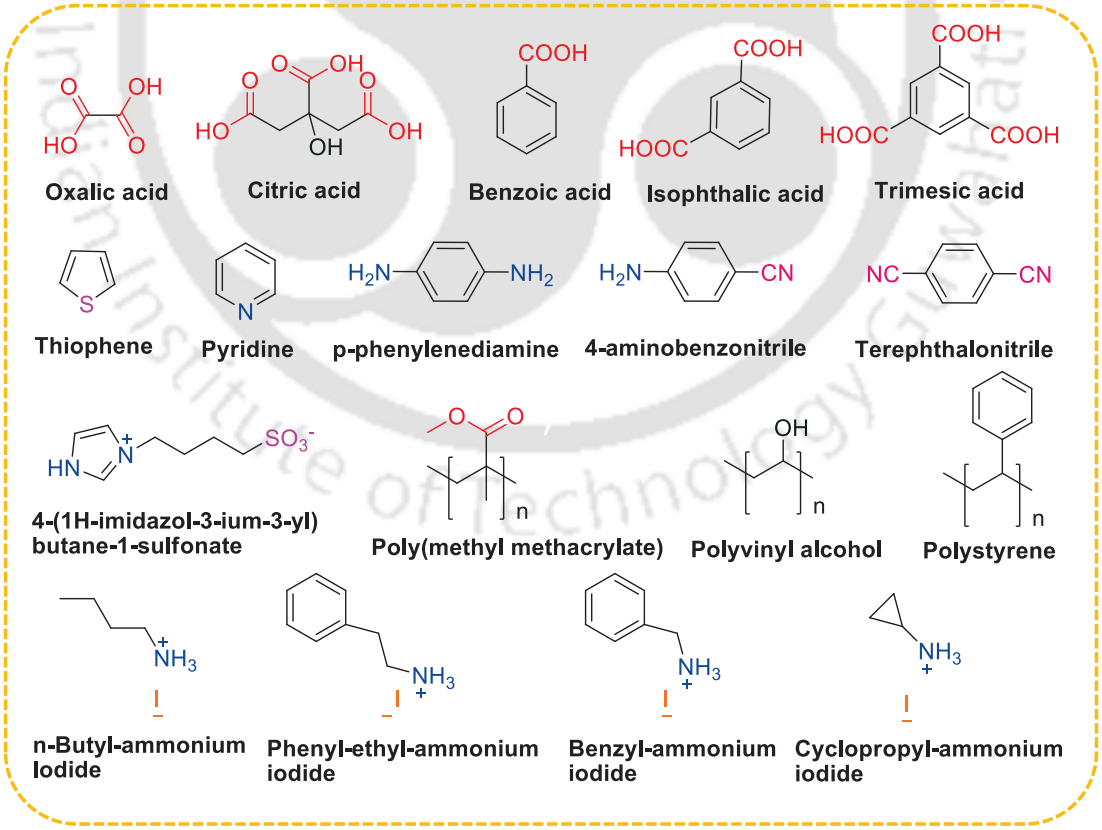

Figure 1.10: Commonly used organic passivating molecules used in PSC.

Upscaling of PSCs has also been a challenge as depositing defect free large-area perovskite films have been difficult. However, with various technology developments such as doctor blading, inkjet printing and spray coating large-area PSCs in the order of a few m^2 have been successfully demonstrated. PSCs have also been fabricated for various purposes including space application.[124-127]

1.7 Thesis Synopsis

Considering the global energy crisis and the demand to explore solar energy in large scale, the inspiration of this thesis was the development of sustainable high performance OSCs and PSCs for capturing the clean energy from the sun. The first working chapter of the thesis covers implementation of hot-casting technique to achieve thick film for OSC. Next chapter onwards fabrication of PSCs have been covered through various device engineering. Controlled crystallization process of the perovskites in each chapter has been explained in detail. The outcome has been defect-free perovskite films for solar cell applications. Large-area solar cells have also been fabricated to showcase the possibility of accepting these device engineering techniques for future commercialization. The results achieved in this thesis work are divided into next four chapters. Lastly, a summary and future prospect is presented. A concise synopsis of each chapter is given below:

Chapter 2 demonstrates the fabrication of OSC using the hot-casting technique through the modulation of morphology and thickness of the PTB7-Th:PCBM based active layer. The solar cell hot-casted at 40 °C displayed the highest PCE of 9.13%, while the device fabricated at room temperature displayed the highest PCE of 8.02%. It was noticed that increasing the hot-casting temperature resulted in higher thickness of the active layer. The moderate hot-casting at 40 °C displayed an average thickness of 133 nm which increased from 99 nm for room temperature coated active layer. Even the active layer coated at 70 °C showcased comparable PCE at an average thickness of over 180 nm. The modified device displayed reduced recombination and improved charge carrier mobility.

Chapter 3 deals with the hot-casting technique in the fabrication of mixed-halide perovskite solar cells. The ratio of three halides was optimized strategically to form micro-meter sized crystalline film with nano-meter sized grain boundary. Also, the ion migration

was minimized by replacing the free iodine vacancy using the bromide ion. Highest PCE of >18% was obtained by minimizing the defect density. This technique was also utilized to fabricate large-area solar cell which displayed an efficiency of ~17% with retention factor of 93%. This halide-engineering combined with hot-casting technique can facilitate large-scale solar module commercialization. The best device retained almost 85% efficiency when placed under ambient conditions due to reduction of grain boundaries which acts as recombination centers.

Chapter 4 showcases the use of an organic molecules trifluoro acetic acid (TFAA) containing the fluoro and carbonyl groups in passivating the defects in the perovskite film. Thus, various concentrations of trifluoroacetic acid were introduced in the perovskite precursor solution and solar cells were fabricated at room-temperature conditions using the one-step anti-solvent technique. The grain size of the modified film increased and higher crystallinity was displayed for the TFAA incorporated films. Highest power conversion efficiency of >20% was obtained in this work. The perovskite films were optimized for crystallinity and grain size to minimize the recombination loss due to the defect states. For predefining the role of each functional group solar cells were also fabricated with only acetic acid and efficiency of ~16% was reached confirming both functional groups passivated the defects in the perovskite to obtain ambient stable perovskite solar cells. The TFAA-modified device also disclosed reduced recombination and improved charge transport.

Chapter 5 describes a novel strategy of dual-passivation of perovskite using p-toluenesulphonic acid (PTSA) and polystyrene (PS) to minimize the defects at the bulk and surface, respectively. The concentration of each was systematically optimized to produce the best film with largest grain size and highest crystallinity. Anti-oxidant PTSA and hydrophobic PS together improved the stability of the solar cell device and retained 93% efficiency after 1000 hours of exposure to the ambient conditions. The highest power conversion efficiency obtained >20.5% and the large-area device displayed an efficiency of ~18.5% with a retention factor of approximately 90%. Mitigated recombination of photo-generated charges along with improved charge transport was observed for dual-passivated device. This can also be a very nice technique for adaptation to commercialize perovskite solar cells.

Chapter 6 covers the conclusion and future prospects of the thesis. A concise review of the all the research works is presented along with the future development scope towards commercialization of organic and perovskite solar cells.

References

1. M. M.-Y. Chan, C.-H. Tao and V. W.-W. Yam, in *WOLEDs and Organic Photovoltaics: Recent Advances and Applications*, ed. V. W. W. Yam, Springer Berlin Heidelberg, Berlin, Heidelberg, 2010, DOI: 10.1007/978-3-642-14935-1_1, pp. 1-35.
2. M. Hoel and S. Kverndokk, *Resour. Energy Econ.*, 1996, **18**, 115-136.
3. N. Armaroli and V. Balzani, *Angew. Chem., Int. Ed.*, 2007, **46**, 52-66.
4. L. Chiari and A. Zecca, *Energy Policy*, 2011, **39**, 5026-5034.
5. PROS AND CONS OF FOSSIL FUELS & WHY CAN FOSSIL FUELS BE GOOD?, https://group.met.com/fyouture/pros-and-cons-of-fossil-fuels/62, (accessed 07.07.2021).
6. Energy used today in the world, https://www.worldometers.info/energy/, (accessed 07.07.2021).
7. Energy in India, https://en.wikipedia.org/wiki/Energy_in_India, (accessed 07.07.2021).
8. 22 of world's 30 most polluted cities are in India: Report, https://economictimes.indiatimes.com/news/politics-and-nation/new-delhi-is-worlds-most-polluted-capital-for-third-straight-year-iqair-study/articleshow/81530587.cms, (accessed 07.07.2021).
9. Energy policy of India, https://en.wikipedia.org/wiki/Energy_policy_of_India, (accessed 07.07.2021).
10. R. Williams, *J. Chem. Phys.*, 1960, **32**, 1505-1514.
11. *Nature*, 1873, **7**, 303-303.
12. Photovoltaic Dreaming 1875–1905: First Attempts At Commercializing PV, https://cleantechnica.com/2014/12/31/photovoltaic-dreaming-first-attempts-commercializing-pv/, (accessed 07.07.2021).
13. The Nobel Prize in Physics 1921, https://www.nobelprize.org/prizes/physics/1921/summary/, (accessed 07.07.2021).
14. April 25, 1954: Bell Labs Demonstrates the First Practical Silicon Solar Cell, https://www.aps.org/publications/apsnews/200904/physicshistory.cfm, (accessed 07.07.2021).
15. L. E. Black, in *New Perspectives on Surface Passivation: Understanding the Si-Al2O3 Interface*, ed. L. E. Black, Springer International Publishing, Cham, 2016, DOI: 10.1007/978-3-319-32521-7_8, pp. 141-153.
16. The World's Oldest Satellite Still in Orbit, http://code8100.nrl.navy.mil/about/heritage/vanguard.htm, (accessed 07.07.2021).
17. C. W. Tang, *Appl. Phys. Lett.*, 1986, **48**, 183-185.
18. A. Kojima, K. Teshima, Y. Shirai and T. Miyasaka, *J. Am. Chem. Soc.*, 2009, **131**, 6050-6051.
19. J. Rostalski and D. Meissner, *Sol. Energy Mater. Sol. Cells.*, 2000, **61**, 87-95.
20. B. P. Rand, J. Genoe, P. Heremans and J. Poortmans, *Prog. Photovoltaics Res. Appl.*, 2007, **15**, 659-676.
21. B. P. Rand, D. P. Burk and S. R. Forrest, *Phys. Rev. B*, 2007, **75**, 115327.
22. J.-M. Nunzi, *C.R. Phys.*, 2002, **3**, 523-542.
23. N. K. Elumalai and A. Uddin, *Sol. Energy Mater. Sol. Cells.*, 2016, **157**, 476-509.

24. M. G. Murali, A. D. Rao, S. Yadav and P. C. Ramamurthy, *Polym. Chem.*, 2015, **6**, 962-972.
25. T. Markvart and L. Castañer, in *Practical Handbook of Photovoltaics (Second Edition)*, eds. A. McEvoy, T. Markvart and L. Castañer, Academic Press, Boston, 2012, DOI: https://doi.org/10.1016/B978-0-12-385934-1.00001-5, pp. 7-31.
26. A. Zaban, A. Meier and B. A. Gregg, *J. Phys. Chem. B*, 1997, **101**, 7985-7990.
27. R. Kern, R. Sastrawan, J. Ferber, R. Stangl and J. Luther, *Electrochim. Acta*, 2002, **47**, 4213-4225.
28. S. A. Haque, Y. Tachibana, R. L. Willis, J. E. Moser, M. Grätzel, D. R. Klug and J. R. Durrant, *J. Phys. Chem. B*, 2000, **104**, 538-547.
29. M. Drießen, D. Amiri, N. Milenkovic, B. Steinhauser, S. Lindekugel, J. Benick, S. Reber and S. Janz, *Energy Procedia*, 2016, **92**, 785-790.
30. E. Kobayashi, Y. Watabe, R. Hao and T. S. Ravi, *Appl. Phys. Lett.*, 2015, **106**, 223504.
31. D. C. Jordan and S. R. Kurtz, *Prog. Photovoltaics Res. Appl.*, 2013, **21**, 12-29.
32. M. Edoff, *AMBIO*, 2012, **41**, 112-118.
33. V. M. Fthenakis, *Renew. Sustain. Energy. Rev.*, 2004, **8**, 303-334.
34. R. W. Collins, A. S. Ferlauto, G. M. Ferreira, C. Chen, J. Koh, R. J. Koval, Y. Lee, J. M. Pearce and C. R. Wronski, *Sol. Energy Mater. Sol. Cells.*, 2003, **78**, 143-180.
35. J. M. Pearce, N. Podraza, R. W. Collins, M. M. Al-Jassim, K. M. Jones, J. Deng and C. R. Wronski, *J. Appl. Phys.*, 2007, **101**, 114301.
36. H. Shirakawa, E. J. Louis, A. G. MacDiarmid, C. K. Chiang and A. J. Heeger, *J. Chem. Soc., Chem. Commun.*, 1977, 578-580.
37. The Nobel Prize in Chemistry 2000, https://www.nobelprize.org/prizes/chemistry/2000/summary/, (accessed 07.07.2021).
38. J. Gong, K. Sumathy, Q. Qiao and Z. Zhou, *Renew. Sustain. Energy. Rev.*, 2017, **68**, 234-246.
39. R. K. Gupta, R. Garai, M. Hossain, M. A. Afroz, D. Kalita and P. K. Iyer, *J. Mater. Chem. C*, 2021, DOI: 10.1039/D1TC01860D.
40. M. A. Green, *Physica E*, 2002, **14**, 65-70.
41. M. Jørgensen, K. Norrman and F. C. Krebs, *Sol. Energy Mater. Sol. Cells.*, 2008, **92**, 686-714.
42. M. He, C. Yan, J. Li, M. P. Suryawanshi, J. Kim, M. A. Green and X. Hao, *Adv. Sci.*, 2021, **8**, 2004313.
43. P. Mandal and S. Sharma, *Renew. Sustain. Energy. Rev.*, 2016, **65**, 537-552.
44. P. Roy, N. Kumar Sinha, S. Tiwari and A. Khare, *Sol. Energy*, 2020, **198**, 665-688.
45. A. Sahu, A. Garg and A. Dixit, *Sol. Energy*, 2020, **203**, 210-239.
46. K. D. G. I. Jayawardena, L. J. Rozanski, C. A. Mills, M. J. Beliatis, N. A. Nismy and S. R. P. Silva, *Nanoscale*, 2013, **5**, 8411-8427.
47. A. Pivrikas, N. S. Sariciftci, G. Juška and R. Österbacka, *Prog. Photovoltaics Res. Appl.*, 2007, **15**, 677-696.
48. N. Tessler, Y. Preezant, N. Rappaport and Y. Roichman, *Adv. Mater.*, 2009, **21**, 2741-2761.
49. J. Nelson, *Curr. Opin. Solid State Mater. Sci.*, 2002, **6**, 87-95.
50. B. R. Weinberger, M. Akhtar and S. C. Gau, *Synth. Met.*, 1982, **4**, 187-197.
51. C. Zhang, W. Luan and Y. Yin, *Energy Procedia*, 2017, **105**, 793-798.

52. J. C. Wang, S. Q. Shi, C. W. Leung, S. P. Lau, K. Y. Wong and P. K. L. Chan, *Appl. Phys. Lett.*, 2012, **100**, 053301.
53. M. D. M. Faure and B. H. Lessard, *J. Mater. Chem. C*, 2021, **9**, 14-40.
54. J. Nelson, *Mater. Today*, 2011, **14**, 462-470.
55. S. Rafique, S. M. Abdullah, K. Sulaiman and M. Iwamoto, *Renew. Sustain. Energy. Rev.*, 2018, **84**, 43-53.
56. H. Kang, G. Kim, J. Kim, S. Kwon, H. Kim and K. Lee, *Adv. Mater.*, 2016, **28**, 7821-7861.
57. E. E. van Dyk and E. L. Meyer, *Renewable Energy*, 2004, **29**, 333-344.
58. B. A. Gregg, *J. Phys. Chem. B*, 2003, **107**, 4688-4698.
59. G. Sherafatipour, J. Benduhn, B. R. Patil, M. Ahmadpour, D. Spoltore, H.-G. Rubahn, K. Vandewal and M. Madsen, *Sci. Rep.*, 2019, **9**, 4024.
60. H. Xu, F. Yuan, D. Zhou, X. Liao, L. Chen and Y. Chen, *J. Mater. Chem. A*, 2020, **8**, 11478-11492.
61. Z. Yang, T. Zhang, J. Li, W. Xue, C. Han, Y. Cheng, L. Qian, W. Cao, Y. Yang and S. Chen, *Sci. Rep.*, 2017, **7**, 9571.
62. R. Po, C. Carbonera, A. Bernardi and N. Camaioni, *Energy Environ. Sci.*, 2011, **4**, 285-310.
63. S. S. van Bavel, M. Bärenklau, G. de With, H. Hoppe and J. Loos, *Adv. Funct. Mater.*, 2010, **20**, 1458-1463.
64. Y. Zang, Q. Xin, J. Zhao and J. Lin, *J. Phys. Chem. C*, 2018, **122**, 16532-16539.
65. N. Gasparini, A. Salleo, I. McCulloch and D. Baran, *Nat. Rev. Mater.*, 2019, **4**, 229-242.
66. Q. An, F. Zhang, J. Zhang, W. Tang, Z. Deng and B. Hu, *Energy Environ. Sci.*, 2016, **9**, 281-322.
67. T. Kietzke, R. Y. C. Shin, D. A. M. Egbe, Z.-K. Chen and A. Sellinger, *Macromolecules*, 2007, **40**, 4424-4428.
68. B. J. Tremolet de Villers, K. A. O'Hara, D. P. Ostrowski, P. H. Biddle, S. E. Shaheen, M. L. Chabinyc, D. C. Olson and N. Kopidakis, *Chem. Mater.*, 2016, **28**, 876-884.
69. S. Lattante, *Electronics*, 2014, **3**.
70. S. Lee, D. Jeong, C. Kim, C. Lee, H. Kang, H. Y. Woo and B. J. Kim, *ACS Nano*, 2020, **14**, 14493-14527.
71. H.-C. Liao, C.-C. Ho, C.-Y. Chang, M.-H. Jao, S. B. Darling and W.-F. Su, *Mater. Today*, 2013, **16**, 326-336.
72. H. Yan, S. Ye and D. S. Seferos, *ACS Appl. Mater. Interfaces*, 2018, **10**, 979-984.
73. R. K. Gupta, R. Garai, M. A. Afroz and P. K. Iyer, *J. Mater. Chem. C*, 2020, **8**, 8191-8198.
74. B. Du, R. Geng, W. Tan, Y. Mao, D. Li, X. Zhang, D. Liu, W. Tang, W. Huang and T. Wang, *J. Energy Chem.*, 2021, **54**, 131-137.
75. Y. Zhao, G. Wang, Y. Wang, T. Xiao, M. A. Adil, G. Lu, J. Zhang and Z. Wei, *Solar RRL*, 2019, **3**, 1800333.
76. L. Zhang, X. Xu, B. Lin, H. Zhao, T. Li, J. Xin, Z. Bi, G. Qiu, S. Guo, K. Zhou, X. Zhan and W. Ma, *Adv. Mater.*, 2018, **30**, 1805041.
77. J. Cheng, R. Hu, X. Meng, Y. Li, X. Yan, X. Yang, X. Liao, L. Li, Q. Pei and K. B. Chong, *Solar RRL*, 2018, **2**, 1800064.

78. Perovskite Mineral Data, http://webmineral.com/data/Perovskite.shtml#.YObekugzbIU, (accessed 08.07.2021).
79. J. Cao and F. Yan, *Energy Environ. Sci.*, 2021, **14**, 1286-1325.
80. J. Y. Kim, J.-W. Lee, H. S. Jung, H. Shin and N.-G. Park, *Chem. Rev.*, 2020, **120**, 7867-7918.
81. Best Research-Cell Efficiency Chart, https://www.nrel.gov/pv/cell-efficiency.html, (accessed 08.07.2021).
82. J. Zhang, W. Zhang, H.-M. Cheng and S. R. P. Silva, *Mater. Today*, 2020, **39**, 66-88.
83. J. Yan and B. R. Saunders, *RSC Adv.*, 2014, **4**, 43286-43314.
84. I. Hussain, H. P. Tran, J. Jaksik, J. Moore, N. Islam and M. J. Uddin, *Emergent Mater.*, 2018, **1**, 133-154.
85. P. Lopez-Varo, J. A. Jiménez-Tejada, M. García-Rosell, S. Ravishankar, G. Garcia-Belmonte, J. Bisquert and O. Almora, *Adv. Energy Mater.*, 2018, **8**, 1702772.
86. X. Yin, Z. Song, Z. Li and W. Tang, *Energy Environ. Sci.*, 2020, **13**, 4057-4086.
87. C. H. Teh, R. Daik, E. L. Lim, C. C. Yap, M. A. Ibrahim, N. A. Ludin, K. Sopian and M. A. Mat Teridi, *J. Mater. Chem. A*, 2016, **4**, 15788-15822.
88. N. Suresh Kumar and K. Chandra Babu Naidu, *J. Materiomics*, 2021, DOI: https://doi.org/10.1016/j.jmat.2021.04.002.
89. K. Mahmood, S. Sarwar and M. T. Mehran, *RSC Adv.*, 2017, **7**, 17044-17062.
90. S. Zheng, G. Wang, T. Liu, L. Lou, S. Xiao and S. Yang, *Sci. China Chem.*, 2019, **62**, 800-809.
91. G. Yang, H. Tao, P. Qin, W. Ke and G. Fang, *J. Mater. Chem. A*, 2016, **4**, 3970-3990.
92. J. Bisquert and E. J. Juarez-Perez, *J. Phys. Chem. Lett.*, 2019, **10**, 5889-5891.
93. C. C. Boyd, R. Cheacharoen, T. Leijtens and M. D. McGehee, *Chem. Rev.*, 2019, **119**, 3418-3451.
94. S. P. Dunfield, L. Bliss, F. Zhang, J. M. Luther, K. Zhu, M. F. A. M. van Hest, M. O. Reese and J. J. Berry, *Adv. Energy Mater.*, 2020, **10**, 1904054.
95. J. Wei, Q. Wang, J. Huo, F. Gao, Z. Gan, Q. Zhao and H. Li, *Adv. Energy Mater.*, 2021, **11**, 2002326.
96. J. Qian, M. Ernst, N. Wu and A. Blakers, *Sustainable Energy Fuels*, 2019, **3**, 1439-1447.
97. A. Kheralla and N. Chetty, *Heliyon*, 2021, **7**, e06211.
98. R. Wang, M. Mujahid, Y. Duan, Z.-K. Wang, J. Xue and Y. Yang, *Adv. Funct. Mater.*, 2019, **29**, 1808843.
99. M. V. Khenkin, E. A. Katz, A. Abate, G. Bardizza, J. J. Berry, C. Brabec, F. Brunetti, V. Bulović, Q. Burlingame, A. Di Carlo, R. Cheacharoen, Y.-B. Cheng, A. Colsmann, S. Cros, K. Domanski, M. Dusza, C. J. Fell, S. R. Forrest, Y. Galagan, D. Di Girolamo, M. Grätzel, A. Hagfeldt, E. von Hauff, H. Hoppe, J. Kettle, H. Köbler, M. S. Leite, S. Liu, Y.-L. Loo, J. M. Luther, C.-Q. Ma, M. Madsen, M. Manceau, M. Matheron, M. McGehee, R. Meitzner, M. K. Nazeeruddin, A. F. Nogueira, Ç. Odabaşı, A. Osherov, N.-G. Park, M. O. Reese, F. De Rossi, M. Saliba, U. S. Schubert, H. J. Snaith, S. D. Stranks, W. Tress, P. A. Troshin, V. Turkovic, S. Veenstra, I. Visoly-Fisher, A. Walsh, T. Watson, H. Xie, R. Yıldırım, S. M. Zakeeruddin, K. Zhu and M. Lira-Cantu, *Nat. Energy*, 2020, **5**, 35-49.
100. W. Xiang, S. Liu and W. Tress, *Energy Environ. Sci.*, 2021, **14**, 2090-2113.
101. L. Gao and G. Yang, *Solar RRL*, 2020, **4**, 1900200.

102. Y. Xu, M. Wang, Y. Lei, Z. Ci and Z. Jin, *Adv. Energy Mater.*, 2020, **10**, 2002558.
103. L. Wagner, L. E. Mundt, G. Mathiazhagan, M. Mundus, M. C. Schubert, S. Mastroianni, U. Würfel, A. Hinsch and S. W. Glunz, *Sci. Rep.*, 2017, **7**, 14899.
104. S. Ghosh, S. Mishra and T. Singh, *Adv. Mater. Interfaces*, 2020, **7**, 2000950.
105. K. Liao, C. Li, L. Xie, Y. Yuan, S. Wang, Z. Cao, L. Ding and F. Hao, *Nano-Micro Lett.*, 2020, **12**, 156.
106. Z. Wan, S. Ren, H. Lai, Y. Jiang, X. Wu, J. Luo, Y. Wang, R. He, Q. Chen, X. Hao, Y. Wang, L. Wu, I. Constantinou, W.-H. Zhang, J. Zhang and D. Zhao, *Adv. Mater. Interfaces*, 2021, **8**, 2100135.
107. N. J. Jeon, J. H. Noh, W. S. Yang, Y. C. Kim, S. Ryu, J. Seo and S. I. Seok, *Nature*, 2015, **517**, 476-480.
108. R. K. Gupta, R. Garai, M. Hossain, A. Choudhury and P. K. Iyer, *ACS Sustainable Chem. Eng.*, 2021, **9**, 7993-8001.
109. P. Zhao, B. J. Kim and H. S. Jung, *Mater. Today Energy*, 2018, **7**, 267-286.
110. B. Chen, P. N. Rudd, S. Yang, Y. Yuan and J. Huang, *Chem. Soc. Rev.*, 2019, **48**, 3842-3867.
111. L. Fu, H. Li, L. Wang, R. Yin, B. Li and L. Yin, *Energy Environ. Sci.*, 2020, **13**, 4017-4056.
112. J. Kim, A. Ho-Baillie and S. Huang, *Solar RRL*, 2019, **3**, 1800302.
113. A. N. Jumabekov, *J. Vac. Sci. Technol. A*, 2020, **38**, 060401.
114. E.-B. Kim, M. S. Akhtar, H.-S. Shin, S. Ameen and M. K. Nazeeruddin, *J. Photochem. Photobiol. C*, 2021, **48**, 100405.
115. F. Zhang, H. Lu, J. Tong, J. J. Berry, M. C. Beard and K. Zhu, *Energy Environ. Sci.*, 2020, **13**, 1154-1186.
116. C. Ortiz-Cervantes, P. Carmona-Monroy and D. Solis-Ibarra, *ChemSusChem*, 2019, **12**, 1560-1575.
117. T. He, S. Li, Y. Jiang, C. Qin, M. Cui, L. Qiao, H. Xu, J. Yang, R. Long, H. Wang and M. Yuan, *Nat. Commun.*, 2020, **11**, 1672.
118. G. Grancini, C. Roldán-Carmona, I. Zimmermann, E. Mosconi, X. Lee, D. Martineau, S. Narbey, F. Oswald, F. De Angelis, M. Graetzel and M. K. Nazeeruddin, *Nat. Commun.*, 2017, **8**, 15684.
119. M. Wang, W. Wang, B. Ma, W. Shen, L. Liu, K. Cao, S. Chen and W. Huang, *Nano-Micro Lett.*, 2021, **13**, 62.
120. J. Li, J. Duan, X. Yang, Y. Duan, P. Yang and Q. Tang, *Nano Energy*, 2021, **80**, 105526.
121. W. Ke and M. G. Kanatzidis, *Nat. Commun.*, 2019, **10**, 965.
122. G. Schileo and G. Grancini, *J. Mater. Chem. C*, 2021, **9**, 67-76.
123. L. Gollino and T. Pauporté, *Solar RRL*, 2021, **5**, 2000616.
124. D. Li, D. Zhang, K.-S. Lim, Y. Hu, Y. Rong, A. Mei, N.-G. Park and H. Han, *Adv. Funct. Mater.*, 2021, **31**, 2008621.
125. Y. Deng, Q. Wang, Y. Yuan and J. Huang, *Mater. Horiz.*, 2015, **2**, 578-583.
126. F. Schackmar, H. Eggers, M. Frericks, B. S. Richards, U. Lemmer, G. Hernandez-Sosa and U. W. Paetzold, *Adv. Mater. Technol.*, 2021, **6**, 2000271.
127. J. E. Bishop, J. A. Smith, C. Greenland, V. Kumar, N. Vaenas, O. S. Game, T. J. Routledge, M. Wong-Stringer, C. Rodenburg and D. G. Lidzey, *ACS Appl. Mater. Interfaces*, 2018, **10**, 39428-39434.

[This page was intentionally left blank]

Chapter 2

Regulating Active Layer Thickness and Morphology for High Performance Hot-casted Organic Solar Cells

---

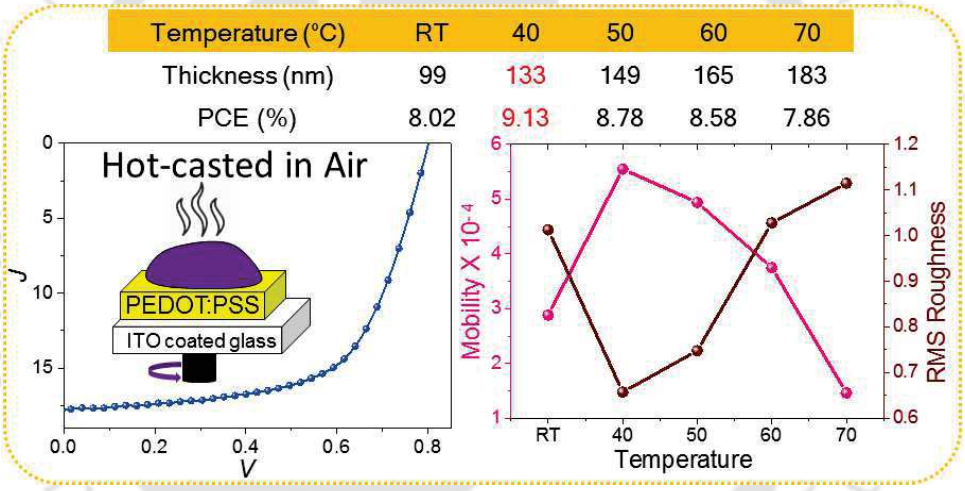

Manuscript: Ritesh Kant Gupta, Rabindranath Garai, Mohammad Adil Afroz, Parameswar Krishnan Iyer, "Regulating Active Layer Thickness and Morphology for High Performance Hot-casted Polymer Solar Cells", *J. Mater. Chem. C*, **2020**, 8, 8191-8198.

Patent: Parameswar Krishnan Iyer, **Ritesh Kant Gupta**, Mohammad Adil Afroz, Rabindranath Garai,"A High Efficiency Polymer Solar Cell and a Process for Fabricating the same", **2020**, Ref. No. 201931019186, Appl. No. 201931019186 A.

[This page was intentionally left blank]

Abstract

Thick films of active layer (Polymer:PCBM blend) are required to harness maximum amount of sunlight and to achieve higher efficiencies in organic solar cells (OSCs). However, realization of thick films along with desired morphology of the active layer is very challenging. Herein, thick films with optimum morphologies have been precisely obtained using hot-casting technique. Superior active layer morphology supports better charge transport. The photovoltaic properties of OSC fabricated with PTB7-Th:$PC_{71}BM$ using the hot-casting technique were thoroughly studied. A significant increase in power conversion efficiency to >9% was observed for the solar cells fabricated at 40 °C compared to the one fabricated at room temperature, which displayed an efficiency of ~8%. The main reason for this improvement was the increased thickness of the active layer that facilitated better light absorption and therefore resulting in enhanced short circuit current density. In addition, the devices fabricated at 40 °C exhibited very low rms roughness enabling better charge transport in the device. The recombination studies and mobility estimation were also performed through impedance spectroscopy and SCLC technique, which gave a clearer insight of the hot casting method. The outcome of this moderate hot-casting technique to achieve low roughness morphology in thick active layer was very promising as this would be a possible breakthrough technique in the manufacturing of highly efficient OSC.

2.1 Overview

Polymer/organic solar cells (OSCs), involving a polymer donor and a fullerene or non-fullerene acceptor blend, has drawn great attention as a possible potent candidate for the future photovoltaics. The flexibility, transparency, lightweight and the ability to be processed through printing or spin coating techniques are the main advantages of OSCs which led them to gain focus of various researchers across the world.[1-3] The power conversion efficiency (PCE) of OSCs has also shown an upward trend since its discovery. Recently, PCE of 18% has been reported, which is very competitively compared with the commercially available silicon solar cell.[4-7] However, improvisation of photovoltaic parameters such as the short circuit current density (*J*sc), open circuit voltage (*V*oc) and fill factor (FF) is necessary for the wide utility of the OSCs in real time application. The desired results can be achieved by regulating the morphology of the active layer by varying the parameters such as thickness and annealing temperature etc.[8, 9] In addition, few reports mention that both device performance and stability was improved by incorporation of various interfacial layers.[10-16]

One of the restraining factors for attaining high performance OSC is the *J*sc which depends on the bandgap of the donor material, thickness of the active layer and charge transport through the device. For achieving higher *J*sc values, extensive research has been carried out to design and develop various low bandgap donor materials. Among the donors, PTB7-Th has become one of the most important discoveries recently with the PCE reaching >10% in combination with $PC_{71}BM$ as an acceptor in a single junction OSC.[17-20] The interaction of PTB7-Th has been thoroughly studied with fullerene as well as various non-fullerene based acceptors to achieve desirable PCEs.[21-26] Also, the possibility of PTB7-Th in ternary and tandem OSC has been investigated by various groups.[27-32] Morphology dependence study for improved PCE in PTB7-Th: $PC_{71}BM$ as an active layer has been explored by modulating the annealing temperature and annealing time.[9, 33] Morphology control of active layer has been also carried out by different solvent engineering, varying the concentration of PCBM loading and introducing additives like DIO, DPS, etc.[3, 20, 34-41] In all these cases, it has been very closely observed that annealing the active layer at ≥70 °C deteriorates the morphology hampering the charge transport and thereafter, reduces the PCE. Additionally, there is a report which suggests that cooling the active layer blend (referred to

as ink) to 40 °C from 80 °C improves the PCE by optimizing the film morphology.[42] A recent work also reports about the effect of PCBM loading on the morphology and charge transport which proves that the device having 1:1.5 ratio of PTB7-Th:$PC_{71}BM$ displays the best performance in solar cells.[20] Researchers have also focused on increasing the thickness of the active layer and retaining the overall PCE of the solar cells. Over 10% PCE was obtained for the active layer thicker than 200 nm, making it quite a prospect for commercialization. These reports suggest that thick films of active layer with good morphology are prerequisites for high efficiency OSC. Attaining thick film with conventional methods, such as by increasing the solution concentration or by spin coating at reduced speed, results in poor morphology.[8, 38]

Motivated by recent reports on hot casting method to fabricate perovskite solar cell where dilute solution was used,[43-45] we used this technique to achieve thick active layer with good morphology. The influence of hot-casting on the morphology and thickness of the active layer consisting of PTB7-Th: $PC_{71}BM$ blend and thereby its effect on the device performance has been studied. The 40 °C active layer hot-casted solar cell displays the highest PCE of 9.13% with *J*sc of 17.82 mA cm^{-2}, *V*oc of 0.822 V and FF of 62%. The PCE was improved from the solar cell fabricated at room temperature (RT, ~27 °C), which showed the highest PCE of 8.02%. This was achieved by regulating thickness and morphology of the active layer film during the hot-casting process. This approach is the first report which reveals the hot-casted OSC advantages to the best of our knowledge.

2.2 Experimental Section

2.2.1 Materials

PEDOT:PSS (PVP AI 4083) was obtained from Clevios. ITO substrates (15 Ω $\square^{-1}$) and $PC_{71}BM$ (>99.5 %) were obtained from LUMTEC. Chlorobenzene (HPLC, purity 99.9%), Calcium (purity >99.99%) and Aluminium (purity >99.99%) were procured from Sigma Aldrich. PTB7-Th was synthesized thermally earlier in our laboratory.[46]

2.2.2 Device Fabrication

A patterned ITO substrate is taken and sequentially cleaned with soap water, DI water, acetone and isopropanol and thereafter, dried with N_2 gas flow and treated with UV-

O3. On the cleaned substrate PEDOT:PSS is deposited through spin-coating at 3000 rpm for 45 s to facilitate proper hole transport in the device. Thereafter, the substrate is annealed at 120 °C for 20 minutes. PTB7-TH and PC71BM was mixed in the weight ratio 1:1.5 in chlorobenzene in the concentration 25 mg ml-1 to prepare the blend solution. Then, the substrate is brought down to a lower temperature to set the hot-casting temperature. Later, the active layer blend is spin-coated at pre-heated substrates kept at various temperatures. Methanol treatment was done on the active layer for achieving better morphology. Lastly, calcium and aluminium were thermally evaporated (pressure ~ 10^{-6} mbar) to complete the device.

2.2.3 Characterization

UV-vis absorption spectroscopy (PerkinElmer Lambda-35) and atomic force microscopy (AFM, Agilent 5500-STM) were carried out on the active layer. All the current densities versus voltage curves were measured using a Keithley 2400 source meter in argon atmosphere. The illumination study to calculate the photovoltaic parameters and recombination factor were carried out under a Newport solar simulator (Oriel Sol 3A, AM 1.5G, 100 mw cm^{-2}) using a shadow mask of 6 mm^2 under argon atmosphere. For external quantum efficiency measurement an Oriel IQE-200 instrument was used in ambient condition. CH Instruments 760D was used in the measurement of impedance spectroscopy. Thickness of the samples was measured using Dektak 150 profilometer. Grazing-incidence X-ray Diffraction (GIXRD) measurements were performed at Anton Paar in SAXSpoint 2.0 instrument with microsource ($\lambda \approx 0.1542$ nm) and an 2D EIGER R 1M hybrid photon counting (HPC) detector with 75 μm^2 pixel size. The X-ray incident angle was fixed at 0.18° to maximize the diffracted signal and minimize the background from substrate scattering.

2.3 Results and Discussions

The UV-vis spectra of the blend films coated using hot casting technique at various substrate temperatures are illustrated in Figure 2.1a. It was observed that the absorbance of the films increased with increasing substrate temperature. Distinguishable change in absorbance was observed as the substrate temperature increased moderately from RT to 40 °C. However, on increasing the temperature further to 50 °C, 60 °C and 70 °C the increment

in the absorbance was very moderate. To analyze the reason for this increase in absorbance, thickness profiles were studied (Figure 2.1b). It was observed that as the film fabrication temperature was increased from RT, the average thickness of the films also increased. Average thickness of 99, 133, 149, 165 and 183 nm was found for films coated at RT, 40 °C, 50 °C, 60 °C and 70 °C, respectively. The hot-casted films displayed better uniformity compared to that of RT films.

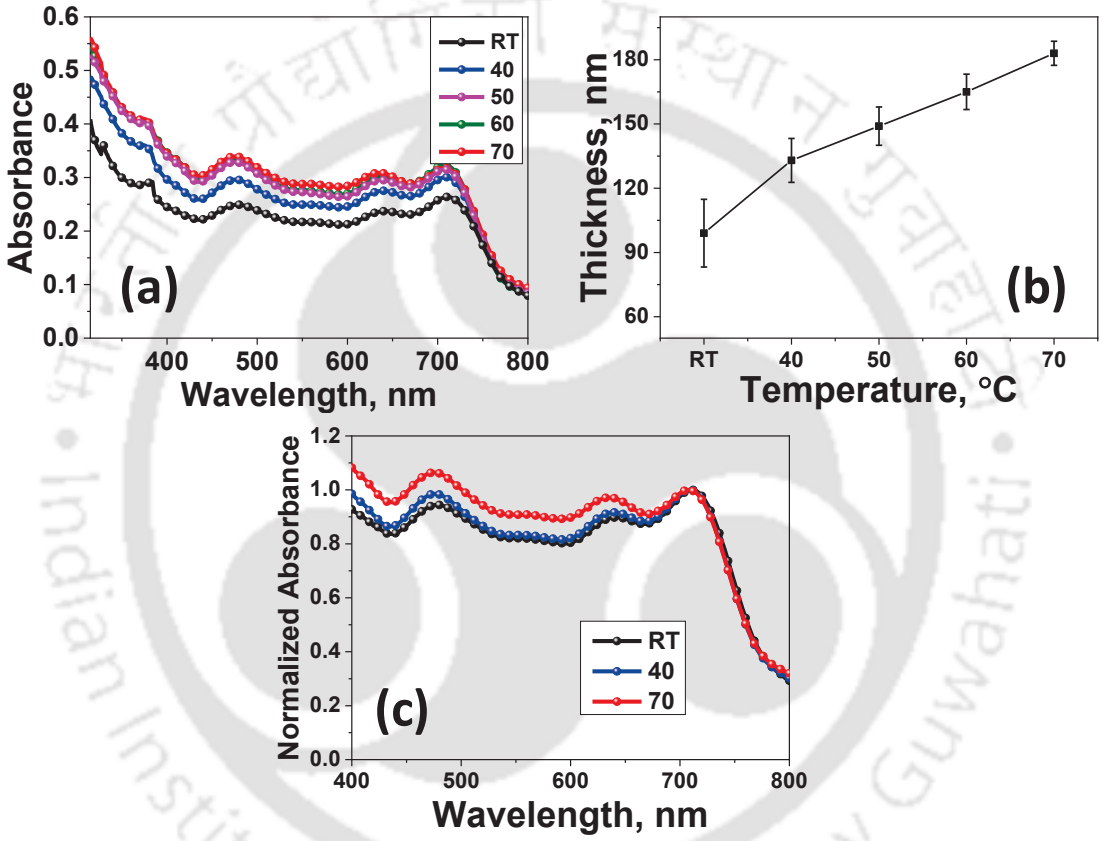

Figure 2.1: (a) Absorbance of blend films coated at various temperatures, (b) variation of active layer thickness with hot-casted temperature and (c) normalized absorption to show decreased crystallinity and increased fullerene loading.

It is also noteworthy to observe in the UV-Vis spectra of the films that the first peak due to PTB7-Th is slightly blue shifted from 642 nm for RT to 639 and 635 nm for 40 °C and 70 °C respectively (Figure 2.1c). This may be due to the decrease in crystallinity of the hot-casted films. Likewise, peak intensity at around 475 nm related

to PCBM was enhanced compared to PTB7-Th peak confirming increased domains of PCBM in hot-casted films.[20]

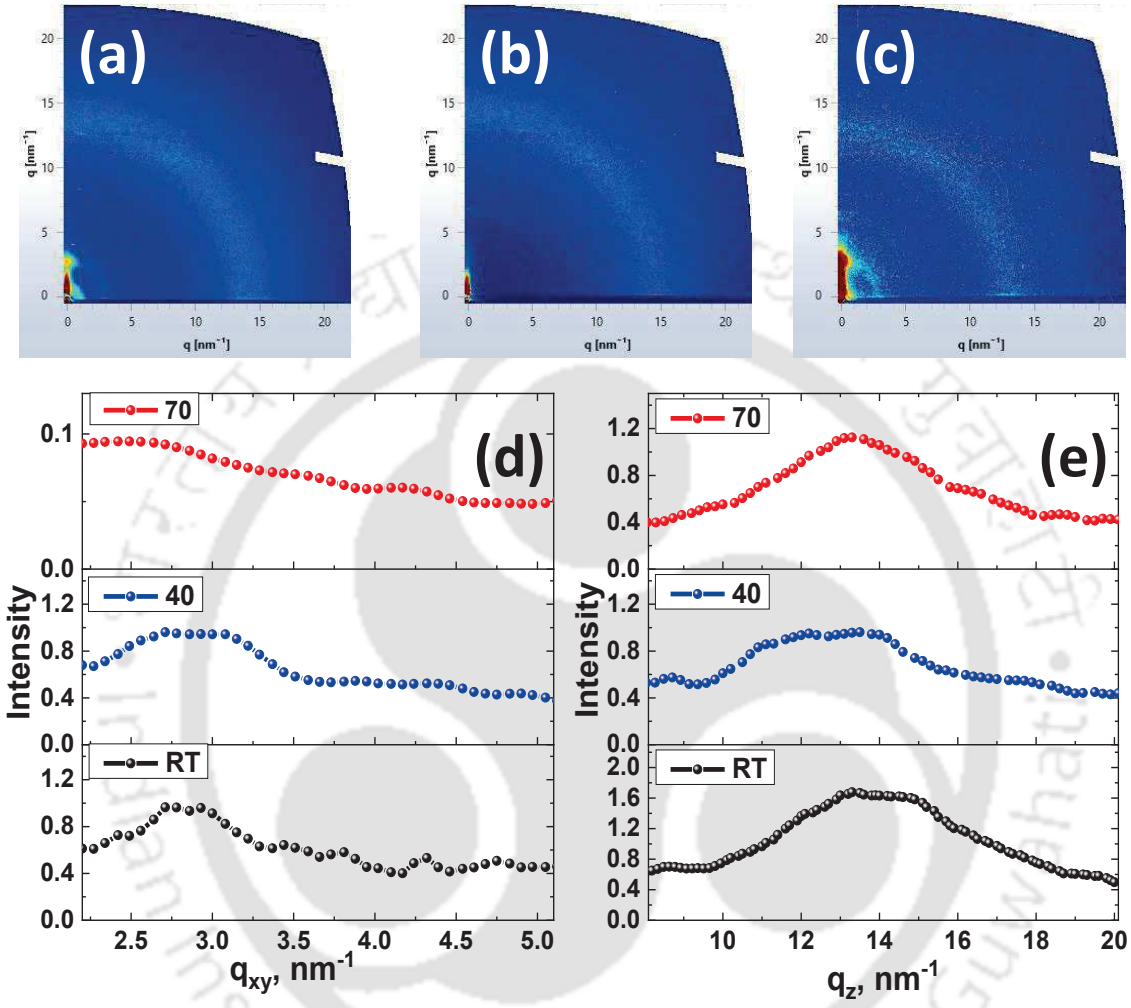

Figure 2.2: 2D GIWAX images of films for (a) RT, (b) 40 °C, (c) 70 °C, 1D GIXRD profile of films (d) in plane and (e) out of plane.

The crystallinity of the films was further verified using the GIWAX 2D plots. It can be clearly seen in the 2D plots (Figure 2.2a-c) that the concentric rings are not very discrete in any of the cases, but on increasing the hot-casting temperature of the films to 40 °C and 70 °C the rings become more diffused. This is in accordance with the crystallinity explained using normalized UV-vis spectra through Figure 2.1c. Also, the lamellar spacing was calculated for the films using the in-plane 1D line cut profile presented in Figure 2.2d. The lamellar spacing was found to be 2.26, 2.32, 2.52 nm for RT, 40 °C and 70 °C films

respectively. It may also be noted from the in-plane line cut profile that the intensity of the peak is similar for RT and 40 °C, but reduces drastically for 70 °C confirming the degree of crystallinity has reduced for films coated at higher temperature. π-π stacking distance was calculated from the 1D out-of-plane line cut profile (Figure 2.2e) and it was found to be ~0.47 nm for all the three films.

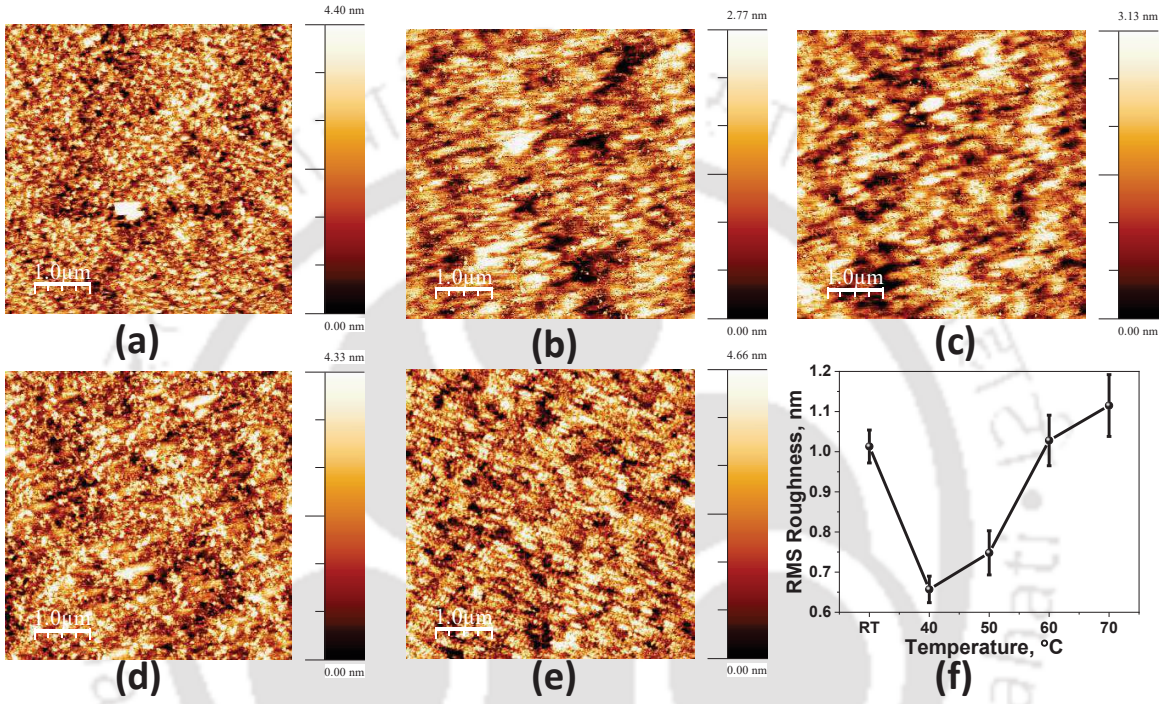

Figure 2.3: AFM images of blend films coated at (a) RT, (b) 40 °C, (c) 50 °C, (d) 60 °C, (e) 70 °C, (f) variation of roughness with hot-casted temperature.

To understand the role of hot-casted temperatures on the surface morphology of the blend films, AFM study was carried out and the same is given in Figure 2.3a-e. The RMS roughness versus hot-casting temperature plot is presented in Figure 2.3f. It can be observed from the curve that the RMS roughness reduced from 1.013 nm for RT to 0.657 nm for 40 °C. On further increasing the temperature the RMS roughness increased to 0.748 nm, 1.028 nm and 1.115 nm for 50 °C, 60 °C and 70 °C, respectively. Thus, it was expected that the solar cell fabricated at 40 °C will have better charge transport.

To verify the effect of the hot-casted films on the performance of solar cell, devices were fabricated as per the schematic shown in Figure 2.4. The active layer blend was coated

on pre-heated substrates at different temperatures between 40 °C and 70 °C at an interval of 10 °C and RT fabrication was used as control. The fabricated device was of inverted architecture with ITO/PEDOT:PSS/Blend/Ca/Al configuration.

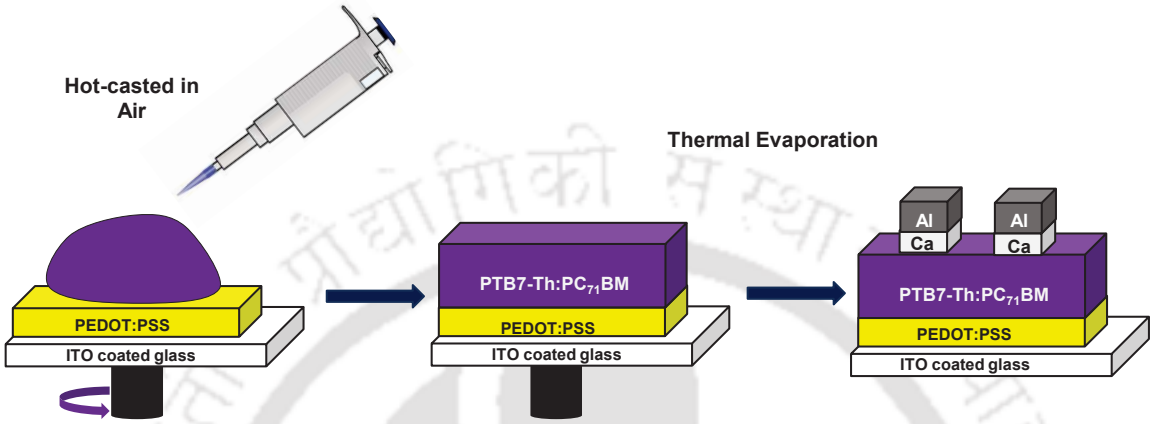

Figure 2.4: Schematic diagram showing the device fabrication steps.

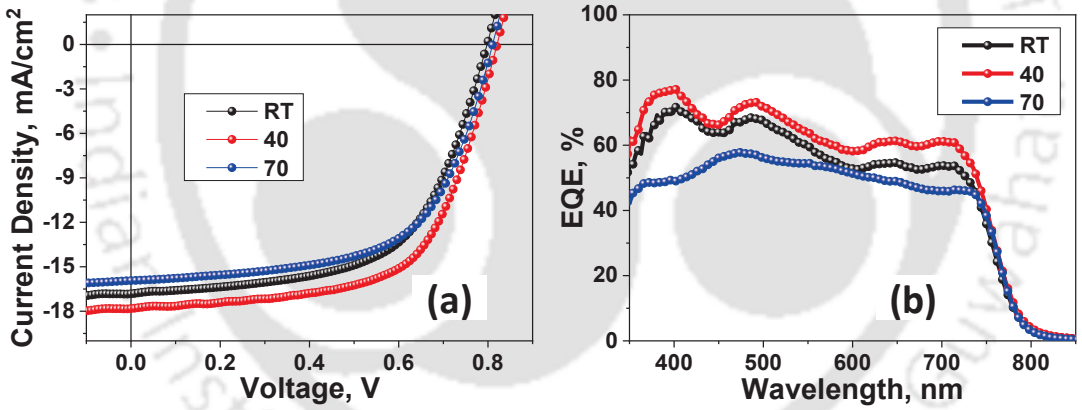

Figure 2.5: (a) *J-V* graph of the fabricated devices, (b) corresponding EQE.

The *J-V* graphs for RT, 40 °C and 70 °C were recorded under illumination and are presented in Figure 2.5a. The photovoltaic parameters are summarized in Table 2.1. The device fabricated at moderately hot-casted temperature of 40 °C displays an improved PCE compared to the one fabricated at RT. The 40 °C device has the highest PCE of 9.13% (average 9.04%) with *J*sc of 17.82 mA cm^{-2}, *V*oc of 0.822 V and FF of 62%. On the other hand, the device fabricated at RT exhibit highest PCE of 8.02% (average 7.89%) with *J*sc of 16.78 mA cm^{-2}, *V*oc of 0.798 V and FF of 60%. On increasing the hot-casting temperature to 70 °C the device PCE reduced to 7.86% (average 7.56%) with *J*sc of 15.92 mA cm^{-2}, *V*oc of

0.811 V and FF of 62%. It is noteworthy that on increasing the temperature from RT to 40 °C *J*sc values increased, but on further increasing the temperature to 70 °C *J*sc reduced. This may be due to better charge transport at reduced roughness and optimum thickness of the active layer. Also, the PCE of 70 °C device was well comparable with the device fabricated at RT. Both *V*oc and FF were increased slightly for all the hot-casted photovoltaic devices. The EQE spectra shown in Figure 2.5b could also be well co-related with the *J*sc values and highest EQE was obtained for the device fabricated at a hot-casting temperature of 40 °C.

Table 2.1: Photovoltaic parameters of hot-casted organic solar cell devices.

Device	J_{SC}, mA/cm^2	V_{OC}, V	FF, %	PCE (average)[a], %
RT	16.78	0.798	59.9	8.02 (7.89± 0.09)
40	17.82	0.822	62.3	9.13 (9.04±0.07)
50	17.35	0.810	62.4	8.78 (8.65±0.08)
60	16.88	0.818	62.1	8.58 (8.35±0.23)
70	15.92	0.811	60.9	7.86 (7.56±0.25)

[a]Average and standard deviation of 10 devices.

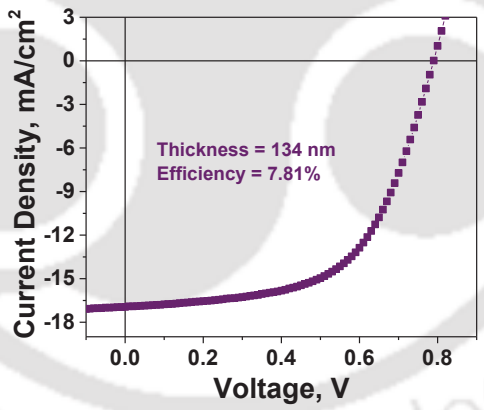

Figure 2.6: *J-V* characteristic curve of device fabricated with 134 nm active layer at RT.

For reference thick active layer (~134 nm) at 2000 rpm were fabricated at RT and maximum PCE of 7.81% was obtained (Figure 2.6). This confirms that thickness obtained though modulation of spin speed do not achieve improved PCE and it is due to the improved morphology of the hot-casted temperature.

The results listed in Table 2.1 are the average of 10 devices. To study the variation of the device parameters across the entire fabricated devices, box chart was plotted (Figure 2.7).

It can be observed that minimum variation in *J*sc is observed for the device fabricated at 40 °C compared to other device types. It was also noted that the variation in *V*oc and FF is nearly similar for all device types. Thus, the major reason for the improved PCE is the increase in *J*sc of the device fabricated at 40 °C.

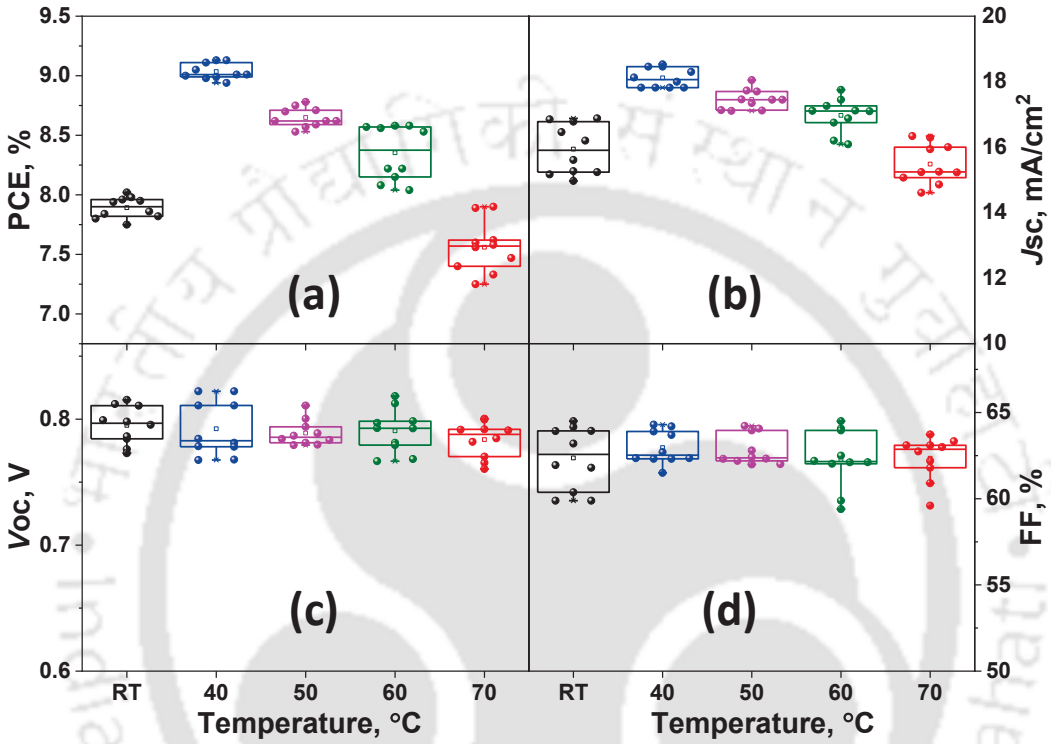

Figure 2.7: Box chart showing variation of (a) PCE, (b) *J*sc, (c) *V*oc, and (d) FF.

To study more details of the loss mechanism of the photo-generated charge carriers the variation of current density at different light intensity were studied. The log-log plot of *J*sc versus the light intensity is shown in Figure 2.8a. From the graph, α value was estimated by finding the slope for each device type. Ideally, α should be equal to 1for zero bimolecular recombination losses and typically the device should have α value close to 1 for better performance. In this case, the device fabricated at RT has α value of 0.909, while the one fabricated at 40 °C has α value of 0.964. On increasing the temperature α value decreased to 0.890 for 70 °C. This confirms that minimum bimolecular recombination or non-radiative recombination through the trap sites happens for the device fabricated at 40 °C and hence, maximum photo-generated charges are extracted in the device fabricated at 40 °C hot-casting temperature which can be one of the reasons for its improved PCE.

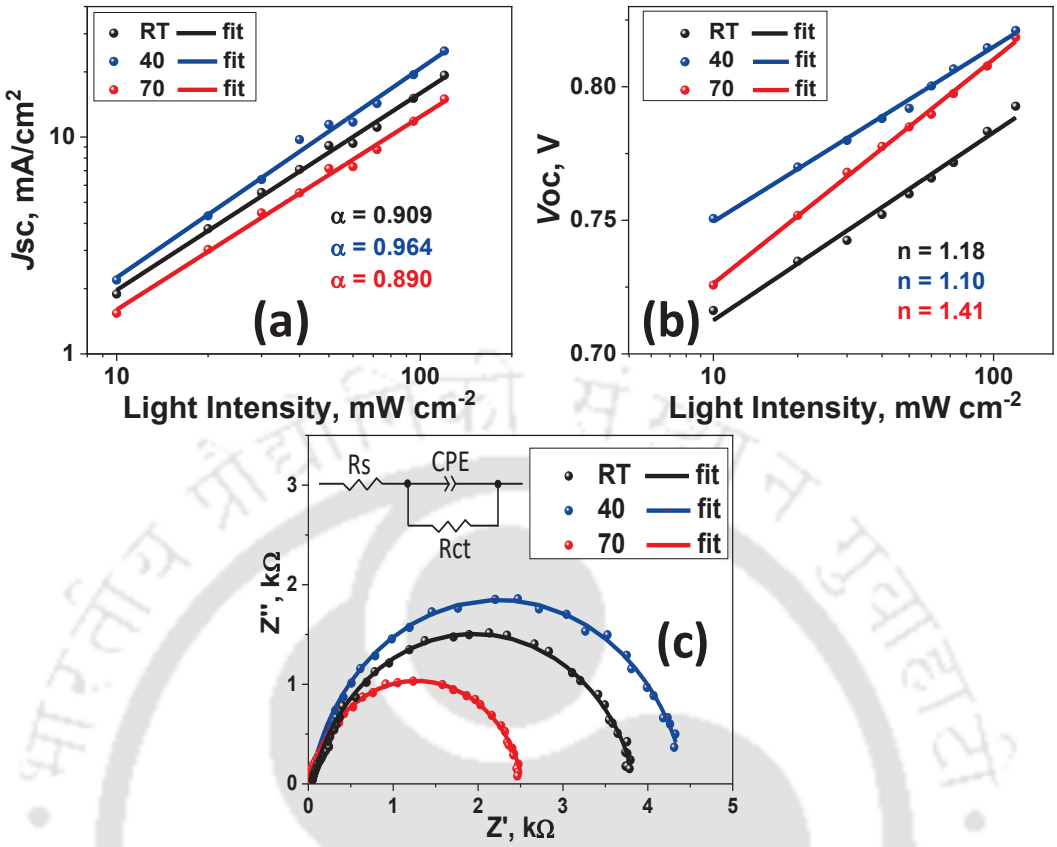

Figure 2.8: (a) *J*sc versus light intensity plot, (b) *V*oc versus light intensity plot, (c) Impedance spectra and the fitting circuit in inset.

Similarly, a semi log plot of *V*oc versus light intensity is plotted in Figure 2.8b. From the fitted curves the slope nkT/q was calculated where n is the ideality factor, k is the Boltzmann's constant, T is the temperature in Kelvin and q is the electronic charge. The value of n, which gives the type of recombination present at open circuit condition, was computed to be 1.18, 1.10 and 1.41 for RT, 40 °C and 70 °C, respectively. Both monomolecular and bimolecular recombination is present in devices fabricated at RT and 40 °C. However, monomolecular recombination is dominant over bimolecular recombination in devices fabricated at RT and bimolecular recombination is dominant over monomolecular recombination for devices fabricated at 40 °C. On increasing the temperature to 70 °C, such higher value of n confirms presence of Shockley-Read-Hall mechanism or monomolecular recombination due to the deep trap states.[14, 25]

The Impedance Spectra (IS) of the devices fabricated at RT, 40 °C and 70 °C are presented in Figure 2.8c. The IS was recorded at dark condition in the frequency range of 100 Hz to 1 MHz. One semi-circle was observed in the spectra, therefore, they were fitted using the equivalent circuit as presented in the inset[47, 48] and the same are represented by the solid lines. The main aim of this study was to determine the series resistance between the cathode and anode (R_s) and the recombination resistance (R_{rec}) of the fabricated devices. R_s was observed to decrease to a very small value of 18.89 Ω for the device fabricated at 40 °C from 49.62 Ω for the device fabricated at RT. On increasing the temperature to 70 °C R_s was observed to increase slightly to 27.55 Ω. On the other hand, R_{rec} was 4419 Ω, maximum for the device fabricated at 40 °C compared to 3805 Ω and 2509 Ω for devices fabricated at RT and 70 °C, respectively. This confirms that the device fabricated at 40 °C has the minimum recombination current and hence, the improved efficiency.

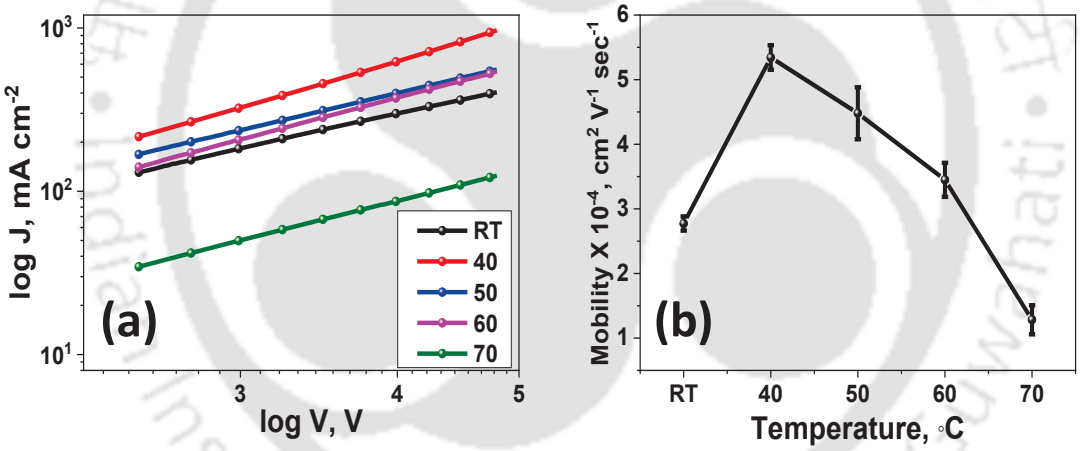

Figure 2.9: (a) SCLC plot for hole only devices, and (b) variation of mobility with hot-casted temperature.

To compare the change in hole mobility due to the hot-casting temperatures, devices with configuration of ITO/PEDOT:PSS/PTB7-Th:$PC_{71}BM$/Cu were fabricated.[49] Thereafter, the dark *J-V* curves of the devices were taken and analyzed using the SCLC method and Mott-Gurney relationship. It was observed that the device fabricated at 40 °C had higher an average mobility of 5.34 x 10^{-4} cm^2 V^{-1} sec^{-1} (highest mobility 5.55 x 10^{-4} cm^2 V^{-1} sec^{-1}) than that of the device fabricated at RT which showed an average mobility of 2.77 x 10^{-4} cm^2 V^{-1} sec^{-1} (highest mobility 2.88 x 10^{-4} cm^2 V^{-1} sec^{-1}). On increasing the hot-casting temperature further the hole mobility of the devices was found to reduce with the average mobility for

device fabricated at 70 °C to be of 1.28 x 10^{-4} cm^2 V^{-1} sec^{-1} (highest mobility 1.46 x 10^{-4} cm^2 V^{-1} sec^{-1}). The *J-V* graph of the hole only devices with highest mobility for the best devices are presented in Figure 2.9a. Figure 2.9b displays the variation of mobility with the hot-casting temperature including error bar and the statistical parameters of three such devices. This increase in hole mobility for the device fabricated at 40 °C can be attributed to the least roughness of the film among all the samples as presented in the AFM images and hence, the improved PCE.

2.4 Conclusions

In summary, the influence of hot-casting technique on the performance of OSC consisting of PTB7-Th as donor and $PC_{71}BM$ as acceptor has been thoroughly studied. PCE was increased to 9.13% for device fabricated at 40 °C from 8.02% for device fabricated at RT. From these results, it is confirmed that the improvement in PCE was due to the increase in *J*sc till 40 °C, moderate hot-casting temperature and thereafter the PCE reduced. However, the *V*oc and FF increased slightly for all the hot-casted devices. The main reason for 40 °C fabricated device to be the best performing was its optimized thickness (~133 nm) and lowest rms roughness obtained for the active layer film. These results were well supported by mobility and recombination studies, confirming that higher mobility values were obtained at 40 °C compared to RT and higher temperature fabricated films. Furthermore, these devices were highly reproducible as can be observed in the box chart made from 10 fabricated devices. Moreover, it was observed that thicker film of ~183 nm displayed PCE of 7.86%, which is ~88% of the highest PCE reported in this work and ~98% for the photovoltaic device fabricated at RT. This technique can very well lead to OSC commercialization that requires thick film active layers.

References

1. A. J. Heeger, *Adv. Mater.*, 2014, **26**, 10-28.
2. E. Wang, W. Mammo and M. R. Andersson, *Adv. Mater.*, 2014, **26**, 1801-1826.
3. Z. Li, X. Xu, W. Zhang, X. Meng, W. Ma, A. Yartsev, O. Inganäs, M. R. Andersson, R. A. J. Janssen and E. Wang, *J. Am. Chem. Soc.*, 2016, **138**, 10935-10944.
4. F. Liu, L. Zhou, W. Liu, Z. Zhou, Q. Yue, W. Zheng, R. Sun, W. Liu, S. Xu, H. Fan, L. Feng, Y. Yi, W. Zhang and X. Zhu, *Adv. Mater.*, 2021, **33**, 2100830.
5. Y. Cui, H. Yao, J. Zhang, K. Xian, T. Zhang, L. Hong, Y. Wang, Y. Xu, K. Ma, C. An, C. He, Z. Wei, F. Gao and J. Hou, *Adv. Mater.*, 2020, **32**, 1908205.
6. Y. Lin, Y. Firdaus, F. H. Isikgor, M. I. Nugraha, E. Yengel, G. T. Harrison, R. Hallani, A. El-Labban, H. Faber, C. Ma, X. Zheng, A. Subbiah, C. T. Howells, O. M. Bakr, I. McCulloch, S. D. Wolf, L. Tsetseris and T. D. Anthopoulos, *ACS Energy Lett.*, 2020, **5**, 2935-2944.
7. C. Li, J. Zhou, J. Song, J. Xu, H. Zhang, X. Zhang, J. Guo, L. Zhu, D. Wei, G. Han, J. Min, Y. Zhang, Z. Xie, Y. Yi, H. Yan, F. Gao, F. Liu and Y. Sun, *Nat. Energy*, 2021, **6**, 605-613.
8. Y. Zang, Q. Xin, J. Zhao and J. Lin, *J. Phys. Chem. C*, 2018, **122**, 16532-16539.
9. L. Krishnan Jagadamma, M. T. Sajjad, V. Savikhin, M. F. Toney and I. D. W. Samuel, *J. Mater. Chem. A*, 2017, **5**, 14646-14657.
10. D. Li, Q. Liu, J. Zhen, Z. Fang, X. Chen and S. Yang, *ACS Appl. Mater. Interfaces*, 2017, **9**, 2720-2729.
11. C. Sun, Z. Wu, Z. Hu, J. Xiao, W. Zhao, H.-W. Li, Q.-Y. Li, S.-W. Tsang, Y.-X. Xu, K. Zhang, H.-L. Yip, J. Hou, F. Huang and Y. Cao, *Energy Environ. Sci.*, 2017, **10**, 1784-1791.
12. C. Li, X. Liu, D. Tu, Q. Yang, X. Chen, C. Li and X. Guo, *Chem. Commun.*, 2019, **55**, 2956-2959.
13. S. Rasool, N. Khan, M. Jahankhan, D. H. Kim, T. T. Ho, L. T. Do, C. E. Song, H. K. Lee, S. K. Lee, J.-C. Lee, W.-W. So, S.-J. Moon and W. S. Shin, *ACS Appl. Mater. Interfaces*, 2019, **11**, 16785-16794.
14. Z. Liu, S. Niu and N. Wang, *J. Colloid. Interf. Sci.*, 2018, **509**, 171-177.
15. V.-H. Tran, S. H. Eom, S. C. Yoon, S.-K. Kim and S.-H. Lee, *Org. Electron.*, 2019, **68**, 85-95.
16. G. Ji, W. Zhao, J. Wei, L. Yan, Y. Han, Q. Luo, S. Yang, J. Hou and C.-Q. Ma, *J. Mater. Chem. A*, 2019, **7**, 212-220.
17. J. Lee, D. H. Sin, B. Moon, J. Shin, H. G. Kim, M. Kim and K. Cho, *Energy Environ. Sci.*, 2017, **10**, 247-257.
18. X. Jia, L. Shen, M. Yao, Y. Liu, W. Yu, W. Guo and S. Ruan, *ACS Appl. Mater. Interfaces*, 2015, **7**, 5367-5372.
19. A. F. Mitul, J. Sarker, N. Adhikari, L. Mohammad, Q. Wang, D. Khatiwada and Q. Qiao, *AIP Adv.*, 2018, **8**, 025018.
20. L. Song, W. Wang, E. Barabino, D. Yang, V. Körstgens, P. Zhang, S. V. Roth and P. Müller-Buschbaum, *ACS Appl. Mater. Interfaces*, 2019, **11**, 3125-3135.
21. W. Yang, L. Ye, F. Yao, C. Jin, H. Ade and H. Chen, *Nano Res.*, 2019, **12**, 777-783.
22. P. Cheng, C. Yan, Y. Wu, J. Wang, M. Qin, Q. An, J. Cao, L. Huo, F. Zhang, L. Ding, Y. Sun, W. Ma and X. Zhan, *Adv. Mater.*, 2016, **28**, 8021-8028.

23. C. Zhang, A. Mumyatov, S. Langner, J. D. Perea, T. Kassar, J. Min, L. Ke, H. Chen, K. L. Gerasimov, D. V. Anokhin, D. A. Ivanov, T. Ameri, A. Osvet, D. K. Susarova, T. Unruh, N. Li, P. Troshin and C. J. Brabec, *Adv. Energy Mater.*, 2017, **7**, 1601204.
24. F. Tang, K. Wu, Z. Zhou, G. Wang, B. Zhao and S. Tan, *ACS Appl. Energy Mater.*, 2019, **2**, 3918-3926.
25. M. P. Hughes, K. D. Rosenthal, R. R. Dasari, B. R. Luginbuhl, B. Yurash, S. R. Marder and T.-Q. Nguyen, *Adv. Funct. Mater.*, 2019, **29**, 1901269.
26. Q. Liu, J. Toudert, F. Liu, P. Mantilla-Perez, M. M. Bajo, T. P. Russell and J. Martorell, *Adv. Energy Mater.*, 2017, **7**, 1701201.
27. P. Cheng, Y. Liu, S.-Y. Chang, T. Li, P. Sun, R. Wang, H.-W. Cheng, T. Huang, L. Meng, S. Nuryyeva, C. Zhu, K.-H. Wei, B. Sun, X. Zhan and Y. Yang, *Joule*, 2019, **3**, 432-442.
28. L. Mao, J. Tong, S. Xiong, F. Jiang, F. Qin, W. Meng, B. Luo, Y. Liu, Z. Li, Y. Jiang, C. Fuentes-Hernandez, B. Kippelen and Y. Zhou, *J. Mater. Chem. A*, 2017, **5**, 3186-3192.
29. L. Lu, W. Chen, T. Xu and L. Yu, *Nat. Commun.*, 2015, **6**, 7327.
30. N. Gasparini, X. Jiao, T. Heumueller, D. Baran, G. J. Matt, S. Fladischer, E. Spiecker, H. Ade, C. J. Brabec and T. Ameri, *Nat. Energy*, 2016, **1**, 16118.
31. H. Do Kim, R. Shimizu and H. Ohkita, *Chem. Lett.*, 2018, **47**, 1059-1062.
32. K. Midori, T. Fukuhara, Y. Tamai, H. Do Kim and H. Ohkita, *ChemPhysChem*, 2019, **20**, 2683-2688.
33. Y.-J. Hsieh, Y.-C. Huang, W.-S. Liu, Y.-A. Su, C.-S. Tsao, S.-P. Rwei and L. Wang, *ACS Appl. Mater. Interfaces*, 2017, **9**, 14808-14816.
34. C. Liu, Y. Zhu, Y. Cao and J. Chen, *J. Phys. Chem. C*, 2019, **123**, 2105-2113.
35. R. Datt, Suman, A. Bagui, A. Siddiqui, R. Sharma, V. Gupta, S. Yoo, S. Kumar and S. P. Singh, *Sci. Rep.*, 2019, **9**, 8529.
36. L. Salamandra, L. La Notte, G. Paronesso, G. Susanna, L. Cinà, G. Polino, L. Mattiello, A. Catini, C. Di Natale, E. Martinelli, A. Di Carlo, F. Brunetti, T. M. Brown and A. Reale, *Energy Technol.*, 2017, **5**, 2168-2174.
37. C. Duan, Z. Peng, F. J. M. Colberts, S. Pang, L. Ye, O. M. Awartani, K. H. Hendriks, H. Ade, M. M. Wienk and R. A. J. Janssen, *ACS Appl. Mater. Interfaces*, 2019, **11**, 10794-10800.
38. J. Chen, F. Pan, Y. Cao and J. Chen, *J. Mater. Chem. A*, 2019, **7**, 1861-1869.
39. Y. Liang, Z. Xu, J. Xia, S.-T. Tsai, Y. Wu, G. Li, C. Ray and L. Yu, *Adv. Mater.*, 2010, **22**, E135-E138.
40. Y.-C. Chao, Y.-H. Liao, H.-L. Hsu, B.-H. Jiang, J.-C. Kao, T.-H. Lai, C.-P. Chen and R.-J. Jeng, *ACS Appl. Energy Mater.*, 2019, **2**, 833-843.
41. J. Li, Y. Wang, Z. Liang, N. Wang, J. Tong, C. Yang, X. Bao and Y. Xia, *ACS Appl. Mater. Interfaces*, 2019, **11**, 7022-7029.
42. H. Yan, S. Ye and D. S. Seferos, *ACS Appl. Mater. Interfaces*, 2018, **10**, 979-984.
43. W. Nie, H. Tsai, R. Asadpour, J.-C. Blancon, A. J. Neukirch, G. Gupta, J. J. Crochet, M. Chhowalla, S. Tretiak, M. A. Alam, H.-L. Wang and A. D. Mohite, *Science*, 2015, **347**, 522.
44. M. A. Afroz, R. K. Gupta, R. Garai, M. Hossain, S. P. Tripathi and P. K. Iyer, *Org. Electron.*, 2019, **74**, 172-178.

45. H. Tsai, W. Nie, Y.-H. Lin, J. C. Blancon, S. Tretiak, J. Even, G. Gupta, P. M. Ajayan and A. D. Mohite, *Adv. Energy Mater.*, 2017, **7**, 1602159.
46. R. Garai, M. Adil Afroz, R. K. Gupta, A. Choudhury and P. K. Iyer, *ACS Omega*, 2020, **5**, 2747-2754.
47. A. Chuchmała, M. Palewicz, A. Sikora and A. Iwan, *Synth. Met.*, 2013, **169**, 33-40.
48. B. Arredondo, M. B. Martín-López, B. Romero, R. Vergaz, P. Romero-Gomez and J. Martorell, *Sol. Energy Mater. Sol. Cells.*, 2016, **144**, 422-428.
49. R. Ratha, A. Singh, M. A. Afroz, R. K. Gupta, M. Baumgarten, K. Müllen and P. K. Iyer, *Synth. Met.*, 2019, **252**, 113-121.

Chapter 3

Halide Engineering for Mitigating Ion Migration and Defect States in Hot-casted Perovskite Solar Cells

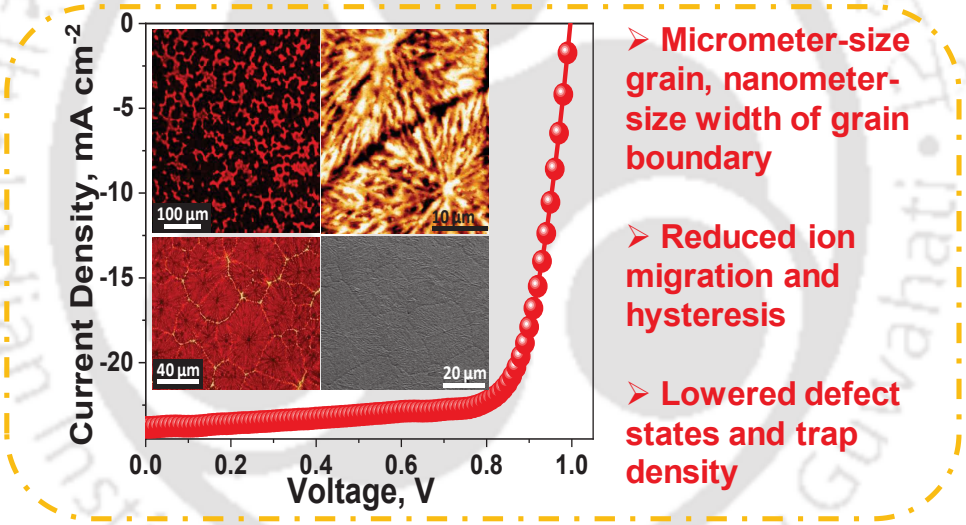

Manuscript: Ritesh Kant Gupta, Rabindranath Garai, Maimur Hossain, Anwesha Choudhury, Parameswar Krishnan Iyer, "Halide Engineering for Mitigating Ion Migration and Defect-States in Hot-Cast Perovskite Solar Cells", *ACS Sustainable Chem. Eng.*, **2021**, 9, 7993-8001.

[This page was intentionally left blank]

Abstract

Precise control of perovskite morphology to achieve large grains with small width grain boundaries is challenging and a pre-requisite for realizing high photovoltaic performance. Ion-migration is another problem with perovskites, which hinders the device results. Herein, incorporation of MABr in mixed halide perovskite $MAPbCl_xI_{3-x}$ has been carried out to minimize ion-migration by replacing the mobile I^- ions in the perovskite with Br^-. Moreover, introduction of MABr results in high quality and smooth films with large grains of average size ~45 μm. Increasing ratio of MABr was added in the perovskite precursor solution and devices with architecture of FTO/PEDOT:PSS/Perovskite/PCBM/Rhodamine-101/Ag was fabricated using the hot-casting technique. The device with MABr ratio of 0.1 (0.1MABr) showed superior power conversion efficiency of 18.08% compared to 14.10% of control without any MABr. For higher ratio, performance deteriorated due to the increase in bandgap of the perovskite which resulted in reduction of short-circuit current density. For 0.1MABr minimum defect states and trap density was obtained using various experimental techniques supporting its optimum device performance. Further, minimum recombination loss was taking place in 0.1MABr device. Similarly, the applicability of this technique in large area devices were studies and efficiency of ~17% was obtained for devices with 2.5 cm^2 dimensions. This innovative concept and approaches are vital tools to achieve large crystalline domains for increasing the solar cell performance for commercial applications.

3.1 Overview

In the field of photovoltaics, the last decade has seen focused research related to perovskite solar cells (PSCs) due to their intriguing optoelectronic properties like wide range absorption, tunable bandgap and longer carrier lifetimes.[1, 2] The low-cost solution-processing method to achieve power conversion efficiency (PCE) beyond 25% has outperformed the widely used commercialized silicon solar cells.[3] Even large-area PSCs have been fabricated using various approaches for their acceptance in real world futuristic applications.[4-7] However, the recognition of this solar photovoltaics technology for commercial applications is far from reality till today. The reason behind this is the irregularity in the formation of perovskite crystals which tends to have films with smaller grain size and larger grain boundaries which acts like trap sites and recombination centre for the photo-generated charges reducing the device performance.[8, 9] Ion migration is another concern in the perovskite films which leads to hysteresis in the current-voltage analysis.[10, 11] Many attempts have been made to inhibit ion-migration in perovskite.[12, 13]

Among all the variants, polycrystalline $MAPbI_3$ is the most famous perovskite to be used in solar cell applications worldwide.[14-17] Many techniques have been utilized to obtain high quality desirable perovskite polycrystalline films for the application of solar cells.[18-21] Among these, the use of anti-solvent while spin-coating is the most commonly used method for depositing perovskite films.[22-24] However, the use of anti-solvent technique is very complex and the method requires post-annealing treatment for optimum time.[25] This has led to the discovery of the hot-casting technique for the fabrication of solar cell devices through modulation of morphology.[26, 27] This technique is comparatively new and does not involve any anti-solvent treatment or annealing of the casted perovskite, yet it yields large-grain crystalline films almost instantly. In perovskite solar cell, the technique is also known to form millimeter size domains with very low-width grain boundaries for minimization of recombination of charge carriers.[28] Nonetheless, there are very few reports that utilize hot-casting technique in which the reactants for the perovskite precursor solution involve PbI_2 and MAI only to obtain the desirable $MAPbI_3$ phase.[29] However, another report suggests that anti-solvent treatment and post-annealing is needed to obtain better quality film for increasing device performance.[30] Therefore, to avail the large sized grains to facilitate

smoother charge transport, MACl is used instead of MAI to form the mixed halide $MAPbCl_xI_{3-x}$ perovskite.[31-33] The use of MACl instead of MAI ensured that no anti-solvent or post-annealing treatment is needed to form large-sized perovskite grains. However, with this large percentage of non-conducting $MAPbCl_3$ phase is also formed along with $MAPbI_3$ due to which there is loss of device performance even though micrometer sized perovskite grains are formed.[34] To overcome this issue, MAI and MACl were used in equal ratio to minimize the unwanted $MAPbCl_3$ phase in the hot-casted perovskite solar cells.[35] Again, this ensured that large-sized desirable perovskite grains are formed and an improvement in PCE was observed by inhibiting the $MAPbCl_3$ phase.

Herein, the role of MABr in mixed halide perovskite $MAPbCl_xI_{3-x}$ formation using the hot-casting technique and its application in solar cell devices has been carried out as a conceptually new approach. As the ratio of MABr was increased in the precursor solution, the redundant $MAPbCl_3$ phase was seen diminishing. Likewise, there was confirmation of the exchange of Br^- with I^- which minimized ion migration, and hence the hysteresis in the device. Highest PCE of 18.08% was achieved for 0.1MABr in which PbI_2, MAI, MACl and MABr was used in the ratio of 1:0.5:0.4:0.1, whereas for the control device without any MABr exhibited PCE of 14.10%. The improvement in the 0.1MABr device was due to increase in all three photovoltaic parameters, i.e. short circuit current density (*J*sc), open circuit voltage (*V*oc) and fill factor (FF). However, on increasing the MABr ratio further the device performance deteriorated due to increase in bandgap, which caused a trade-off between the *J*sc and *V*oc of the solar cell devices. UV-vis study confirmed superior photon harvesting capability of the MABr modified films and blue-shifted onset due to increase in bandgap for MABr incorporation, which was confirmed through PL analysis as well. Multiple microscopy analysis like confocal imaging, optical imaging, FESEM and AFM was carried out to realize the changes due to introduction of MABr. Not only did the grain size increase with reduction in grain boundary width for 0.1MABr, but the film had minimum non-radiative recombination of the generated charges. Even the 0.1MABr device displayed lowest trap density and defect states with minimum recombination loss. Further, the stability of 0.1MABr solar cell was considerably higher than the control device. The possibility of this technique in fabrication of large area device was also checked and PCE of ~17% was obtained for 2.5 cm^2 device area.

3.2 Experimental Section

3.2.1 Materials

Fluorine doped tin oxide (FTO) coated glass (7Ω/sq.), Lead iodide (PbI_2,99%), Methyl ammonium bromide (MABr, 99%), anhydrous DMF, anhydrous DMSO, Rhodamine-101 and silver was purchased from Sigma Aldrich. Methylammonium chloride (MACl, 98.0%) was purchased from TCI chemicals. Methylammonium iodide (MAI, 99%) was purchased from Greatcell Solar. (6,6)-Phenyl-C61-butyric Acid Methyl Ester (PCBM, >99.5%) was purchased from LUMTEC for electron transport layer. Poly(3,4-ethylenedioxythiophene)-poly(styrenesulfonate) (PEDOT:PSS, PVP AI 4083) was procured from Clevios for hole-transporting layer. All the materials were used as received until otherwise specified.

3.2.2 Device Fabrication

The solar cell devices were fabricated on FTO coated glass which was pre-patterned and cleaned sequentially in soap solution, de-ionized water, acetone and isopropanol. The substrate was then dried under N_2 gas and UV-ozone treated before further processing. PEDOT:PSS was used as hole transporting layer which was spin-coated on the cleaned FTO glass at 5000 rpm for 45 sec and annealed at 120 ºC for 30 min. 0.43M perovskite precursor solution was prepared using PbI_2, MAI, MACl and MABr in the ratio of 1:0.5:(0.5-x):x (where x=0, 0.1, 0.2 and named as control, 0.1MABr and 0.2MABr respectively) in 1ml anhydrous DMF:DMSO in the ratio 3:2. The precursor solution was stirred overnight at 70 ºC. The precursor solution was spin-coated at 4000 rpm for 30 sec using the hot-casting technique where the PEDOT:PSS coated substrate was pre-heated at 160 ºC and immediately kept on spin-coater for deposition of perovskite on the hot-substrate. The perovskite coated film was not annealed further. 12 mg/mL PCBM in chlorobenzene was used as electron transport layer which was spin-coated at 1000 rpm for 30 sec on top of perovskite. Lastly, thin layer of rhodamine-101 in isopropanol was spin-coated at 4000 rpm for 30 sec. 100 nm of Ag was used at cathode metal was vacuum deposited at 10^{-6} mbar pressure. The overall device architecture was FTO/PEDOT:PSS/Perovskite/PCBM/Rhodamine-101/Ag.

3.2.3 Characterization

The hot-casted perovskite films were characterized by X-ray diffraction (XRD, Rigaku Micromax-007HF diffractometer equipped with Cu Kα1 irradiation [λ =1.54184 Å]), UV–vis absorption spectroscopy (PerkinElmer Lambda-35), optical microscopy (Leica DM 2500P polarizing optical microscope with QICAM FAST1394 camera), scanning electron microscopy (SEM, JEOL JSM-7610F), atomic force microscopy (AFM, Agilent 5500-STM instrument), and current density−voltage (*J*−*V*) characteristic curves were recorded with a Keithley 2400 source meter in argon atmosphere for dark characterization. All light characteristic was done by illuminating the device with a solar simulator (Newport, Oriel Sol 3A solar simulator, AM 1.5G, 100 mW cm^{-2}) using a shadow mask. The steady state current analysis, Mott-Scottky and impedance spectroscopic measurement were performed using an electrochemical workstation (CH Instruments 760D). An Oriel IQE-200 instrument was used to record the incident photon-to-current efficiency (IPCE) in ambient condition.

3.3 Results and Discussions

Perovskite films with various MABr ratios were coated using the hot-casting technique and X-ray diffraction (XRD) study was carried out to understand the role of MABr in controlling the crystallinity (Figure 3.1a). 110, 220 and 310 planes for the $MAPbI_3$ were present in all the films confirming the perovskite arrangement. Moreover, as MACl was used in the formation of mixed halide perovskite, the 110 plane peak for $MAPbCl_3$ was found whose peak intensity decreased on increasing the MABr ratio. Interestingly, the 110 peak for $MAPbI_3$ shifted to higher 2θ value when the MABr ratio was increased (Figure 3.1b). This can be a confirmation for Br^- ion interaction in the perovskite film due to any I^- vacancy in the perovskite film. Generally, these peak shift to higher 2θ values is very common and are observed in previous works on bromide addition for controlling ion migration.[36]

UV-vis study (Figure 3.1c) was performed on all hot-casted perovskite films. The films modified with MABr showed an increase in absorption compared to the one without MABr. The mid-wavelength region the 0.2MABr film displayed slight lower absorption compared to 0.1MABr film. Identical film thickness of perovskite of ~480 nm was obtained for all three perovskite films. Therefore, it was expected that the best photon harvesting could

be observed for 0.1MABr film due to improved quality of the perovskite film. It is well-known that on addition of bromide there is an increase in bandgap of the perovskite.[37] The bandgap for control, 0.1MABr and 0.2MABr perovskite film was calculated to be 1.59, 1.62, 1.65 eV, respectively as confirmed from the Tauc plot for all the perovskite films (Figure 3.1d).

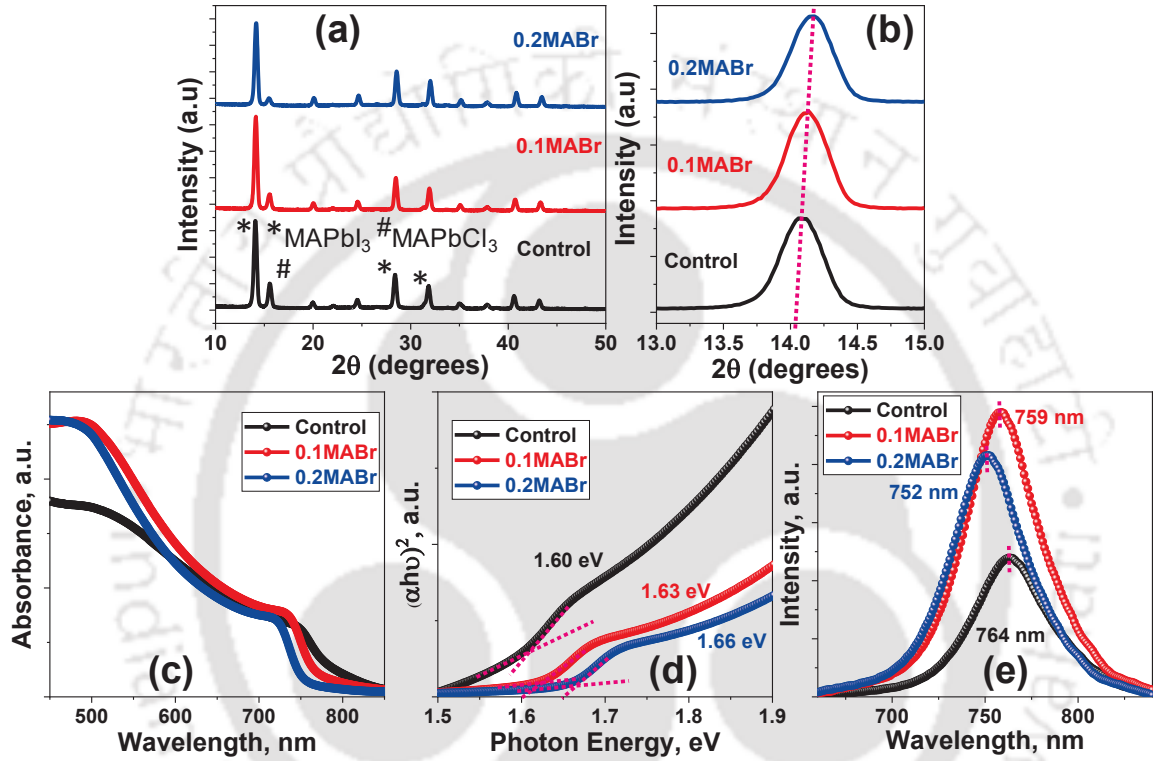

Figure 3.1: (a) XRD patterns of perovskite films with various MABr concentrations, (b) Enlarged XRD patterns to evaluate the peak shifting, (c) UV-vis absorption spectra of perovskite films with different MABr concentrations, (d) Tauc plot, and (e) PL curve of perovskite films with different MABr concentrations.

All the films were also subjected to photoluminescence (PL) study (Figure 3.1e) by coating the perovskite with different MABr ratios on a glass substrate. It was observed that the PL intensity of the 0.1MABr film increased almost two-folds compared to the control film. However, for 0.2MABr film the PL intensity decreased slightly. This increase in PL intensity of the 0.1MABr perovskite was due to the reduction in non-radiative recombination of the charge carriers, which is attributed to the superior quality of the film. Moreover, it was observed that on increasing the MABr ratio the peak in the PL study blue-shifted to 759 and

752 nm for 0.1MABr and 0.2MABr respectively from 764 nm for control. This can be due to the increase in bandgap of the perovskite with MABr introduction.

Confocal intensity mapping of all the three hot-casted perovskite films (Figure 3.2a-c) indicated that brighter the confocal image confirms with higher PL intensity and least non-radiative recombination. As observed, the control film displays least brightness with many black spots. However, for both 0.1MABr and 0.2MABr films the black spots were reduced drastically, but higher brightness was observed for 0.1MABr film. This was in-line with the PL study which suggested least non-radiative recombination for 0.1MABr film.

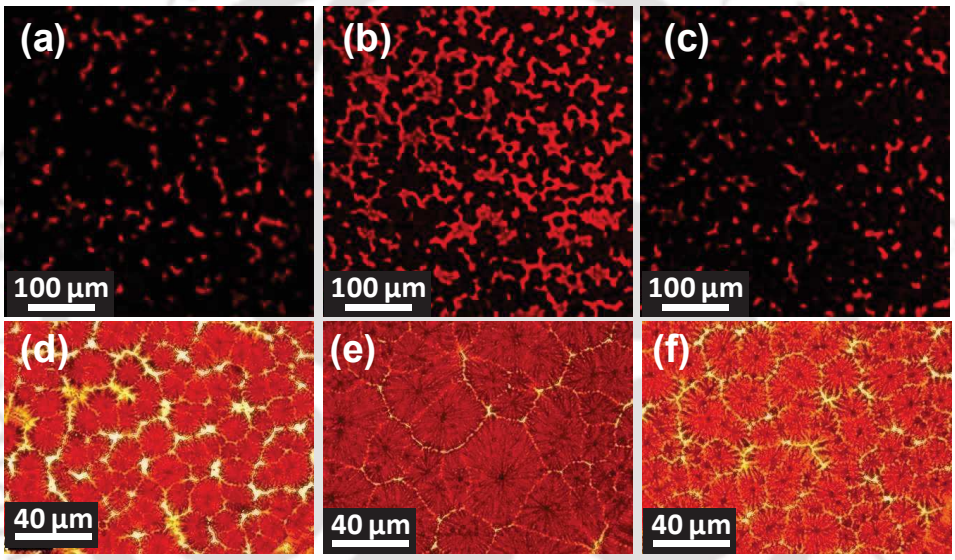

Figure 3.2**:** Confocal intensity mapping of the perovskite films for (a) control, (b) 0.1MABr, and (c) 0.2MABr; optical microscopic images of the perovskite films for (d) control, (e) 0.1MABr, and (f) 0.2MABr.

To get more insight regarding the morphology of the hot-casted perovskite film, optical microscopic images were also recorded (Figure 3.2d-f). It was noticed that the grain size of the perovskite increases in 0.1MABr film compared to the control film However, for the 0.2MABr film the grain size reduced again due to the slight shift towards cubic $MAPbBr_3$ phase from tetragonal $MAPbI_3$ phase. The average grain size for each hot-casted perovskite films were recorded and presented in the histogram plot (Figure 3.3a-c). The average grain size for the control film was 27 µm which increased to 45 µm for 0.1MABr film. The average grain size reduced to 37 µm for 0.2MABr film. The variation in grain size clearly indicated

the role of MABr in the formation of better perovskite crystals to support improved charge transport.

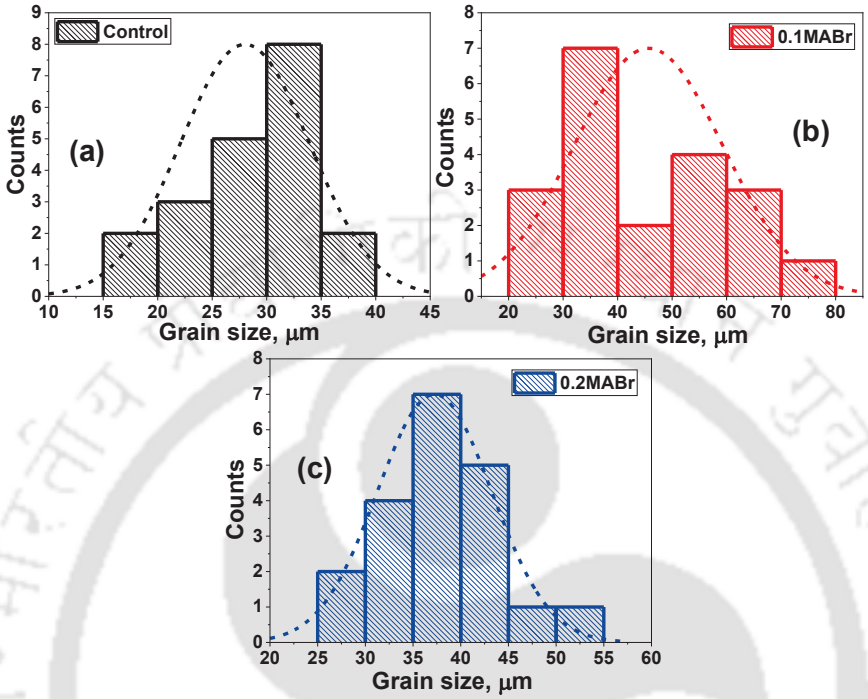

Figure 3.3: Histogram plot showing grain size variation of perovskite films for (a) control, (b) 0.1MABr, and (c) 0.2MABr obtained from the microscopic images.

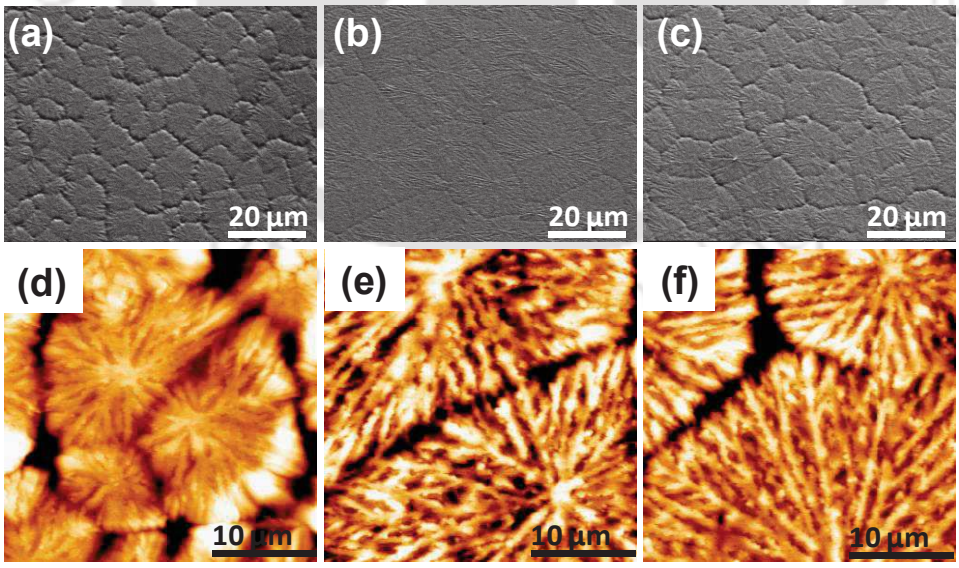

Figure 3.4**:** FESEM images of the perovskite films for (a) control, (b) 0.1MABr, and (c) 0.2MABr; AFM images of the perovskite films for (d) control, (e) 0.1MABr, and (f) 0.2MABr.

Further, field emission scanning electron microscopy (FESEM) analyses of the films (Figure 3.4a-c) were in-order with the optical microscopy images. The highest grain size with very good quality smooth film was recorded for the 0.1MABr. Both the control and 0.2MABr perovskite films had smaller grain size compared to 0.1MABr film, and the grain boundaries were more prominent for control and 0.2MABr film.

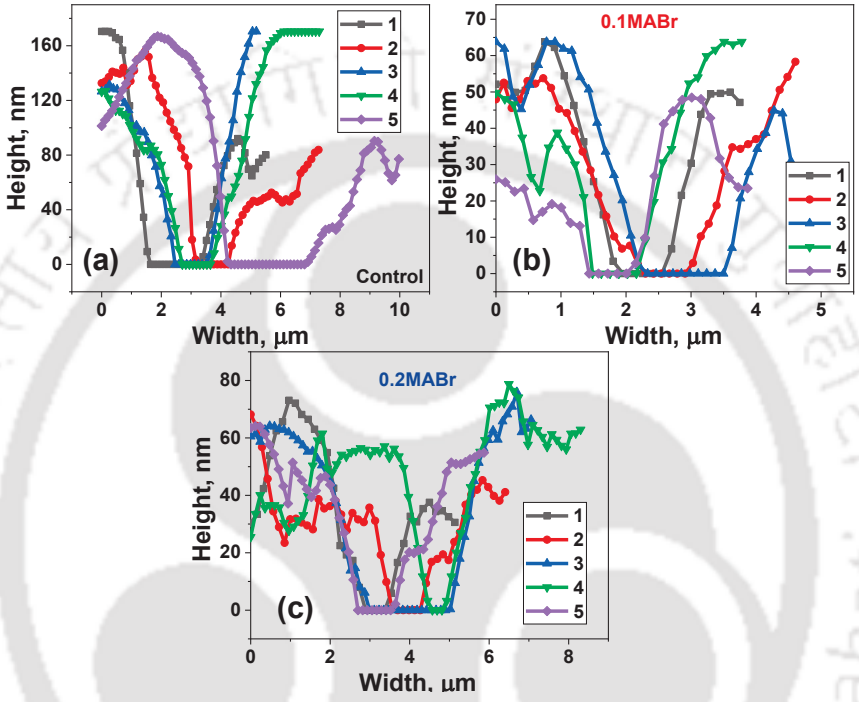

Figure 3.5: Line profile along the grain boundaries to measure grain boundary width for (a) control, (b) 0.1MABr, and (c) 0.2MABr obtained from the AFM images.

To understand more about the surface roughness and comprehend clearly about the grain boundaries atomic force microscopy (AFM) was carried out (Figure 3.4d-f). The surface RMS roughness reduced to 15 nm for 0.1MABr film compared to 35 nm of the control film. The RMS roughness increased slightly to 17 nm for 0.2MABr film. To calculate the average width of the grain boundaries in between two perovskite grains various line profiles were recorded for all hot-casted films (Figure 3.5a-c) and was found to be ~1.5 µm for control film. However, for the 0.1MABr and 0.2MABr films the average grain boundaries was observed to be approximately 700 and 940 nm respectively. Further, the height of the grain boundaries was the minimum for 0.1MABr film which is also conclusive from the line profile of the AFM images.

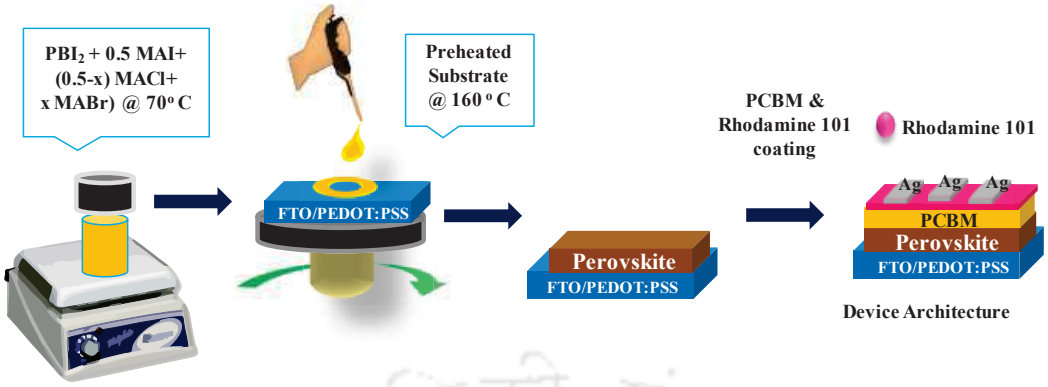

Figure 3.6: Device fabrication steps of the hot-casted perovskite solar cells.

Considering the optical and morphological changes of the hot-casted perovskite films due to MABr incorporation, inverted solar cells with p-i-n architecture of FTO/PEDOT:PSS/Perovskite/PCBM/Rhodamine101/Ag was fabricated. The schematic of the hot-casted perovskite solar cells fabrication are presented in Figure 3.6 and explained elaborately in the experimental section 3.2.2. The *J-V* characteristics graphs of all devices are present in Figure 3.7a and the parameters are tabulated in Table 3.1. The control device without any MABr displayed highest PCE of 14.10% (average PCE of 12.93±0.61%) with *V*oc of 931.3 mV, *J*sc of 21.71 mA cm^{-2} and FF of 69.7%. The results improved with the introduction of MABr in the precursor solution and for 0.1MABr the highest PCE of 18.08% (average PCE of 17.50±0.30%) was obtained with *V*oc of 996.8 mV, *J*sc of 23.86 mA cm^{-2} and FF of 75.4%. However, for 0.2MABr the PCE dropped to a highest value of 16.73% (average PCE of 15.96±0.57%) with *V*oc of 992.2 mV, *J*sc of 22.57 mA cm^{-2} and FF of 74.7%. There is a decrease in PCE at higher MABr ratio due to the trade-off between *V*oc and *J*sc which is a result of increase in bandgap of the perovskite. External quantum efficiency (EQE) recorded for all devices (Figure 3.7b) were observed to be in-order with the photovoltaic results with highest EQE for 0.1MABr perovskite solar cell. The integrated *J*sc, calculated from the EQE spectra, correlated well with the results obtained experimentally through *J-V* curve analysis as well. Interestingly, there was a blue-shift in onset of the EQE spectra for 0.1MABr and 0.2MABr devices compared to the control devices which was very similar to the UV-vis spectra of the perovskite films. The steady state current and efficiency was recorded for the 0.1MABr solar cell (Figure 3.7c). Stable PCE of >17.5% was obtained for 300 s constant illumination.

Table 3.1: Photovoltaic parameters of small area hot-casted solar cell PSC devices.

Device	J_{SC}, mA-cm^{-2}	V_{OC}, mV	FF, %	PCE (average)[a], %
Control	21.71	931.3	69.7	14.10 (12.93±0.61)
0.1MABr	23.86	996.8	75.4	18.08 (17.50±0.30)
0.2MABr	22.57	992.2	74.7	16.73 (15.96±0.57)

[a]Average and standard deviation of 15 devices.

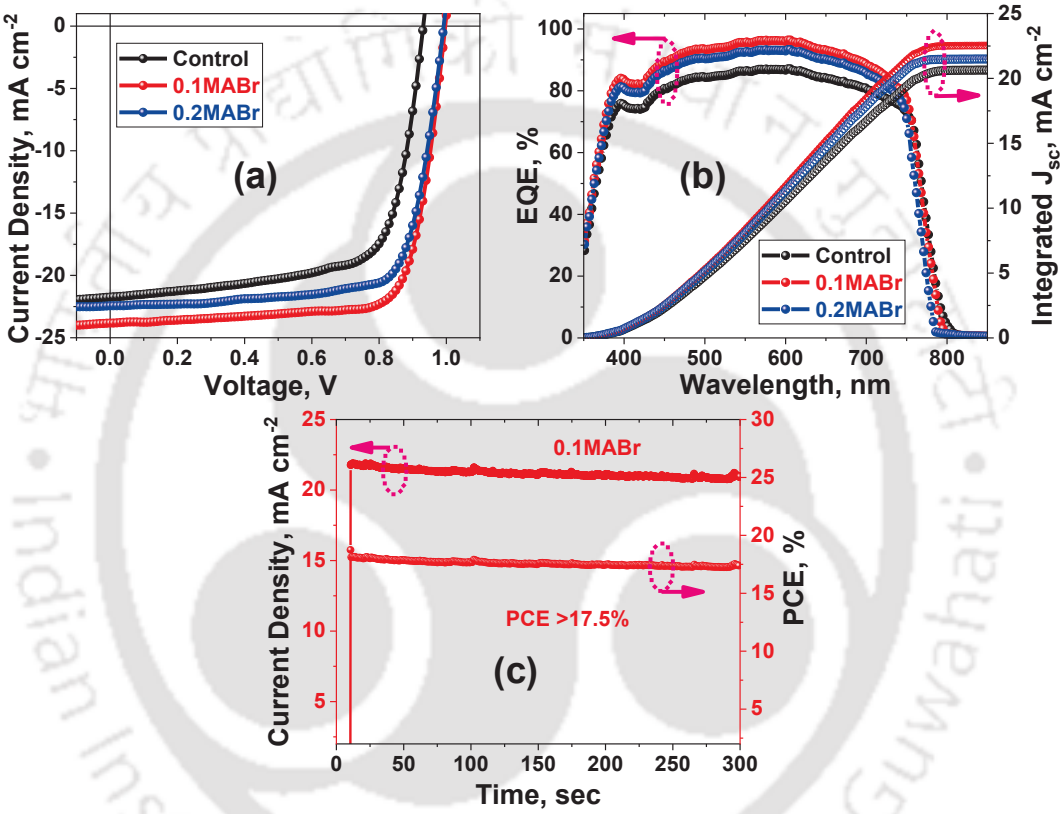

Figure 3.7: (a) *J–V* curves of the devices with various MABr concentrations, (b) EQE curves of devices with integrated *J*sc spectra, and (c) steady-state current measured at the maximum power point for the 0.1MABr device.

The reproducibility of the perovskite photovoltaic devices was verified and plotted with box-chart (Figure 3.8a-d). The increase in PCE for 0.1MABr was due to increase in all parameters, i.e. *V*oc, *J*sc and FF. However, for 0.2MABr the PCE decreased due to the decrease in *J*sc even though there was slight increase in the *V*oc. Furthermore, it was observed that with the addition of MABr the FF increased with very little cell to cell variation. This was due to the reduction in ion migration in the perovskite.

To confirm the minimization of ion migration due to the presence of MABr, all devices were put through forward and reverse scans and hysteresis index (HI) was calculated as per the following equation (3.1):

$$HI = \frac{PCE_{forward} - PCE_{reverse}}{PCE_{forward}} X\ 100 \qquad (3.1)$$

The hysteresis plots with forward and reverse scans (Figure 3.9a-c) confirm that the HI reduced to 2.16% for 0.1MABr device from 4.90% for control device. 0.2MABr device displayed even lower HI of 0.72% confirming that the ion migration is minimized with higher MABr incorporation.

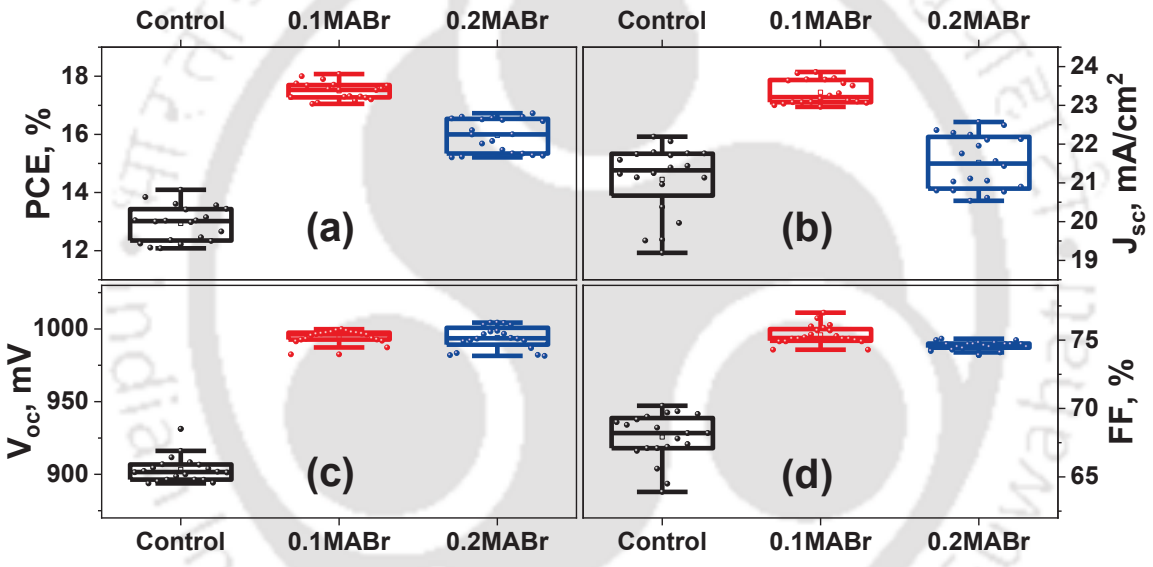

Figure 3.8: Box chart showing variation of (a) PCE, (b) *J*sc, (c) Voc, and (d) FF.

Thereafter, to compute the trap density, hole-only devices with the architecture FTO/PEDOT:PSS/Perovskite/MoO_3/Cu were fabricated. *J-V* graph of each hole-only devices were measured and the voltage where current suddenly increases due to trap filling (V_{TFL}) is recorded (Figure 3.9d-f). From the obtained V_{TFL} values, the trap density (N_{trap}) is calculated using the equation (3.2):[38]

$$N_{trap} = \frac{2\varepsilon\varepsilon_0 V_{TFL}}{eL^2} \qquad (3.2)$$

where, ε is the dielectric constant of perovskite, ε_0 is permittivity of free space, e is the charge of electron and L is the thickness. The V_{TFL} values obtained for control, 0.1MABr and 0.2MABr were 695, 571 and 608 mV respectively. From the obtained V_{TFL} values, the N_{trap} was calculated to be 10.8×10^{15}, 8.8×10^{15} and 9.4×10^{15} cm^{-3} respectively. The decrease in trap density for 0.1MABr can be attributed to the smooth quality of the perovskite film with very small width of the grain boundary which acts as trap sites for the generated charges. Again, the increase in the trap density for 0.2MABr can be endorsed due to slight increase in the width of the grain boundary.

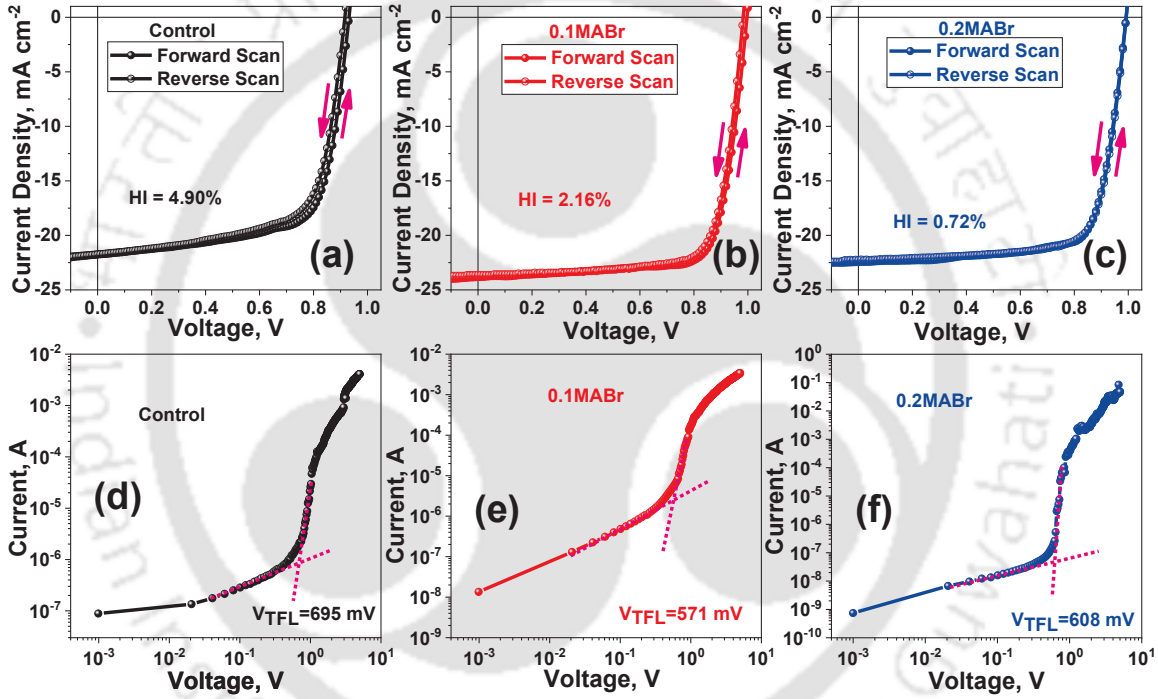

Figure 3.9**:** Hysteresis analysis of the perovskite devices for (a) control, (b) 0.1MABr, & (c) 0.2MABr, and Dark *J-V* analysis of hole-only perovskite devices for (d) control, (e) 0.1MABr, & (f) 0.2MABr.

Impedance spectroscopy (Figure 3.10a) was recorded for all solar cell devices and fitted with the circuit as shown in the inset. It can be seen that the highest recombination resistance of 39 KΩ was obtained for 0.1MABr device while for the control device it was only 9 KΩ. It must be also noted that the recombination resistance for 0.2MABr device was 29 KΩ. The recombination resistance is correlated to *V*oc, thus the higher voltage for 0.1MABr compared to control device is justified. However, as the recombination resistance is lowered for 0.2MABr, the increase in *V*oc is not as proportionate compared to 0.1MABr

device due to the higher recombination loss. This can be attributed to higher trap density in 0.2MABr compared to 0.1MABr device.

Additionally, the energy states disorders can be estimated from the band edge of an UV-vis spectrum in the form of Urbach energy (E_u) represented by the equation (3.3):[39]

$$\alpha = \alpha_0 \exp\left(\frac{E}{E_u}\right) \qquad (3.3)$$

where, α is the absorption coefficient, α_0 is a constant and E is the photon energy. Therefore, the inverse slope in the plot of ln(α) versus E (Figure 3.10b) can project the value of E_u. The calculated E_u values were 323, 98, 119 meV for control, 0.1MABr and 0.2MABr devices respectively. It can be observed that the least value of E_u was found for 0.1MABr device which confirms least defect states at the energy band edge compared to control and 0.2MABr.

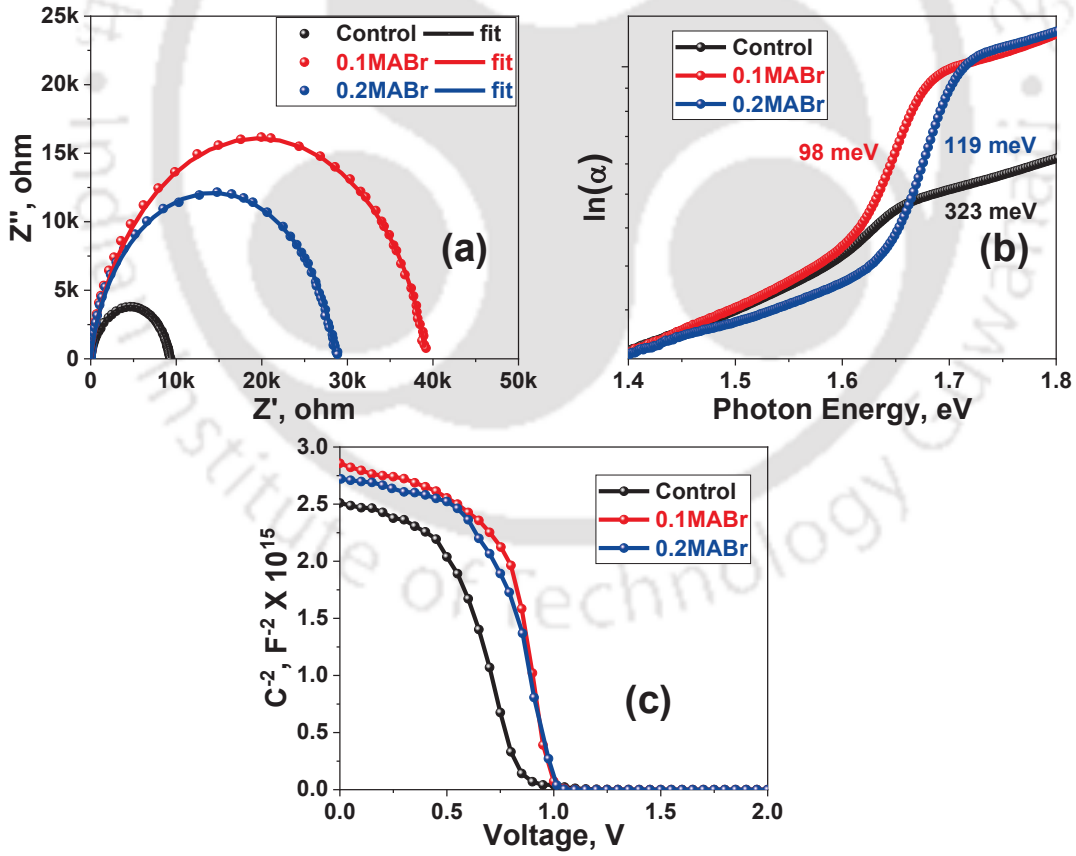

Figure 3.10: (a) Nyquist plots of the devices with various MABr ratios, (b) ln(α) vs photon energy plot used to estimate Urbach energy, and (c) MS plots.

Mott-Schottky (MS) plot (Figure 3.10c) estimated the built-in potential (V_{bi}) and residual charges (N) in the device. The V_{bi} for the control, 0.1MABr and 0.2MABr devices was found from the x-intercept to be 854, 986 and 1011 mV respectively. The increase in value of the V_{bi} can be a possible reason for improved Voc for the MABr modified solar cell devices. The value for N was calculated to be 3.2 x 10^{16}, 2.1 x 10^{16} and 2.3 x 10^{16} cm^{-3} for control, 0.1MABr and 0.2MABr devices, respectively. The least value of N confirms that more number of charges is easily getting transported to the electrodes for 0.1MABr device compared to the other two variants; hence, highest Jsc was obtained for it due to lesser charge recombination.

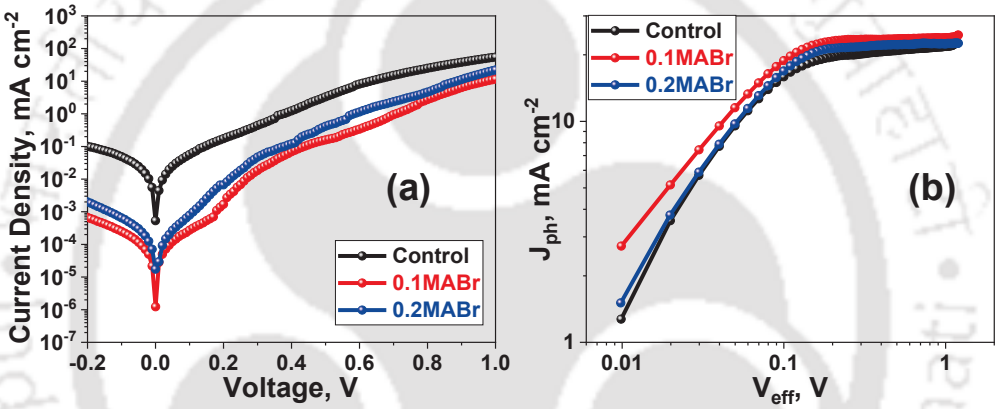

Figure 3.11: (a) Dark J-V curves of the solar cell devices with various MABr ratios, and (b) J_{ph} vs V_{eff} characteristics with double logarithmic axis for different MABr ratios.

Dark J-V spectra were also recorded for the complete solar cell device (Figure 3.11a). From the figure, it is absolutely clear that the least reverse saturation current was observed for 0.1MABr device compared to control and 0.2MABr. This leads to minimum leakage current in the 0.1MABr device which confirms least recombination of the injected charges, an improved transport and collection of the charges at the electrodes for the 0.1MABr device. All this can be possible reason for improved Voc and FF in the MABr-modified device. To have an insight about the charge generation rate in the solar cell devices, J_{ph} versus V_{eff} plots were recorded (Figure 3.11b). J_{ph} is the difference between the current densities recorded under light and dark, whereas V_{eff} is the difference between the voltage where J_{ph} = 0 and the applied voltage. In all the cases, J_{ph} increased linearly till V_{eff} ~0.1 V and saturates at higher voltage. However, highest J_{ph} was obtained for 0.1MABr device which confirms best light

absorption and charge generation in the photo-active layer. Higher J_{ph} at higher V_{eff} confirms efficient charge transport and collection. This could be a possible reason for highest *J*sc in the 0.1MABr device.

One of the biggest problems with any PSCs is its stability. To confirm whether the modified device addresses the issue, pristine un-encapsulated 0.1MABr solar cell device was put through ambient stability test (temperature = 25±2 ˚C, humidity = 40±5%) and compared with the control device (Figure 3.12a). It was observed that 0.1MABr device retained almost 85% of its initial efficiency up to 20 days, whereas the control device retained only 50% of its initial efficiency. The improvement in stability was due to the ion exchange between the Br^- and I^- ions. The control and 0.1MABr films were also exposed to ambient condition for 20 days and XRD study was done to ensure the reason for stability (Figure 3.12b, c). It can be seen that a large peak of PbI_2 appears for control film; however, for the 0.1MABr film PbI_2 peak observed after 20 days was of very less intensity. Further, there was no shift of the $MAPbI_3$ peak to lower 2θ value confirming that once the Br^- ion interacts with the perovskite, it does not leave the film and helps in minimizing the ion migration and improving its stability. It is also well-known that the stability of perovskite improves for large grain size as the density of grain-boundaries reduces.[40, 41] In this case, both the density and width of the grain boundaries has reduced for 0.1MABr device which can be another reason for improvement in stability.

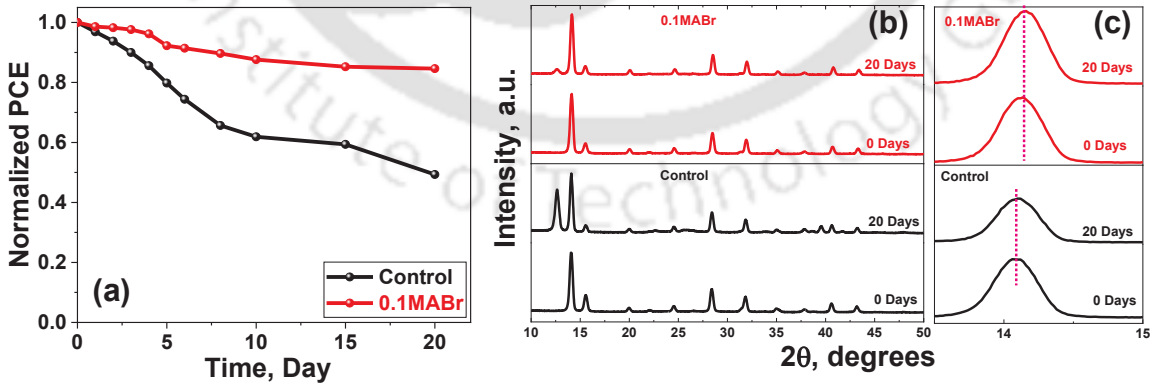

Figure 3.12: (a) Normalized efficiency of control and 0.1MABr devices stored at room temperature in a relative humidity of 40 ± 5%, (b) XRD patterns of perovskite films showing stability after 20 days, and (c) Enlarged XRD patterns to evaluate no peak shifting.

Table 3.2: Photovoltaic parameters of large area hot-casted solar cell PSC devices.

Device	J_{SC}, mA-cm^{-2}	V_{OC}, mV	FF, %	PCE (average)[a], %	Retention, %
Control	20.64	903.7	65.9	12.28 (11.56±0.66)	87
0.1MABr	23.86	996.8	75.4	16.96 (16.48±0.34)	93

[a]Average and standard deviation of 03 devices.

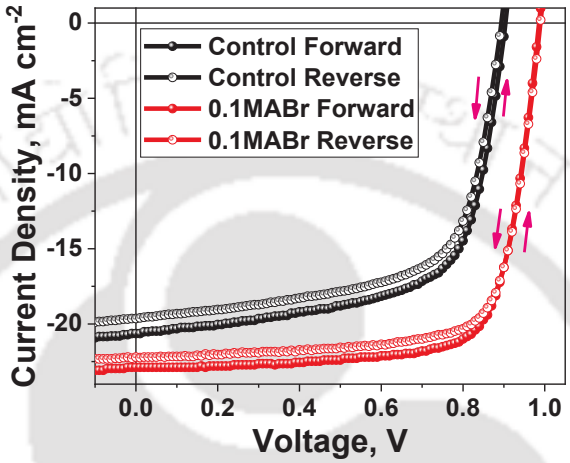

Figure 3.13: Forward and reverse *J–V* curves of control and 0.1MABr large-area devices.

For the possibility of using this technique for fabrication of large area photovoltaic to be used in commercial applications, solar cell devices of 2.5 cm^2 area were fabricated for 0.1MABr. The *J-V* graph for the same is presented in Figure 3.13. The PCE for the large device was 16.96% with *V*oc of 986.2 mV, *J*sc of 22.88 mA cm^{-2} and FF of 75.2%, which are remarkable for device with such large dimension using hot-casting technique. For comparison, control device was also fabricated in large-area and a PCE of 12.28% was obtained (Table 3.2). From the obtained results, retention PCE was calculated for the large area devices with respect to the PCE obtained for the small-area device of same type.[42, 43] It can be well established that the retention PCE of large-area device for 0.1MABr was ~93% of the best device PCE in small area, whereas for control it was ~87% of the best device PCE in small area. This can be due to the formation of smooth large-grains films with very small grain boundary widths. HI was also calculated for the large-area devices by taking the forward and reverse *J-V* scans and found to be 6.35% and 2.95% for control and 0.1MABr, respectively.

3.4 Conclusions

In summary, the precise role of conceptual approaches such as halide exchange by using MABr in tuning the morphology of the mixed halide perovskite has been extensively studied by using confocal imaging, optical microscopy, FESEM and AFM in this work. Micrometer-sized grains with nanometer-sized grain boundary width were obtained. Its application in hot-casted perovskite solar cell has been established as well. The PCE increased from 14.08% for the control device to 18.08% for the 0.1MABr device. This confirmed that small addition of MABr improves the device performance through increase in all device parameters, i.e. *V*oc, *J*sc and FF. Also, as there is a trade-off between *V*oc and *J*sc due to increase of bandgap the PCE reduces for 0.2MABr device. The main reason for the improvement in device performance for 0.1MABr was reduction in trap density and defect states. Subsequently, 0.1MABr device ensured smooth charge transport and collection at the electrodes by minimizing the recombination. Furthermore, the devices fabricated were reproducible with very little variation in the MABr modified solar cells. Besides, the 0.1MABr device displayed superior ambient condition stability compared to the control one due to minimization of ion migration. Large area device of 2.5 cm^2 was also fabricated and PCE of ~17% was achieved for 0.1MABr device confirming the utility of this technique for large-area solar cell fabrication for sustainable commercial applications.

References

1. A. Kojima, K. Teshima, Y. Shirai and T. Miyasaka, *J. Am. Chem. Soc.*, 2009, **131**, 6050-6051.
2. S. D. Stranks, G. E. Eperon, G. Grancini, C. Menelaou, M. J. P. Alcocer, T. Leijtens, L. M. Herz, A. Petrozza and H. J. Snaith, *Science*, 2013, **342**, 341.
3. National Renewable Energy Laboratory, Best research-cell efficiencies chart, https://www.nrel.gov/pv/assets/pdfs/best-research-cell-efficiencies.20200104.pdf, (accessed 28.04.2021).
4. C. Li, J. Yin, R. Chen, X. Lv, X. Feng, Y. Wu and J. Cao, *J. Am. Chem. Soc.*, 2019, **141**, 6345-6351.
5. J. Cao, B. Wu, J. Peng, X. Feng, C. Li and Y. Tang, *Sci. China Chem.*, 2019, **62**, 363-369.
6. Y. Chen, L. Zhang, Y. Zhang, H. Gao and H. Yan, *RSC Adv.*, 2018, **8**, 10489-10508.
7. D.-K. Lee, D.-N. Jeong, T. K. Ahn and N.-G. Park, *ACS Energy Lett.*, 2019, **4**, 2393-2401.
8. C. C. Boyd, R. Cheacharoen, T. Leijtens and M. D. McGehee, *Chem. Rev.*, 2019, **119**, 3418-3451.
9. Y. Shao, Y. Fang, T. Li, Q. Wang, Q. Dong, Y. Deng, Y. Yuan, H. Wei, M. Wang, A. Gruverman, J. Shield and J. Huang, *Energy Environ. Sci.*, 2016, **9**, 1752-1759.
10. D. Lan, *Prog. Photovoltaics Res. Appl.*, 2020, **28**, 533-537.
11. T. Zhang, H. Chen, Y. Bai, S. Xiao, L. Zhu, C. Hu, Q. Xue and S. Yang, *Nano Energy*, 2016, **26**, 620-630.
12. V. K. Ravi, R. A. Scheidt, A. Nag, M. Kuno and P. V. Kamat, *ACS Energy Lett.*, 2018, **3**, 1049-1055.
13. A. Walsh and S. D. Stranks, *ACS Energy Lett.*, 2018, **3**, 1983-1990.
14. Z. Chen, B. Turedi, A. Y. Alsalloum, C. Yang, X. Zheng, I. Gereige, A. AlSaggaf, O. F. Mohammed and O. M. Bakr, *ACS Energy Lett.*, 2019, **4**, 1258-1259.
15. H. Kim, J. Lee, B. Kim, H. R. Byun, S. H. Kim, H. M. Oh, S. Baik and M. S. Jeong, *Sci. Rep.*, 2019, **9**, 15461.
16. H. Zhao, S. Wang, M. Sun, F. Zhang, X. Li and Y. Xiao, *J. Mater. Chem. A*, 2018, **6**, 10825-10834.
17. L. A. Frolova, A. I. Davlethanov, N. N. Dremova, I. Zhidkov, A. F. Akbulatov, E. Z. Kurmaev, S. M. Aldoshin, K. J. Stevenson and P. A. Troshin, *J. Phys. Chem. Lett.*, 2020, **11**, 6772-6778.
18. N. J. Jeon, J. H. Noh, Y. C. Kim, W. S. Yang, S. Ryu and S. I. Seok, *Nat. Mater.*, 2014, **13**, 897-903.
19. N. J. Jeon, J. H. Noh, W. S. Yang, Y. C. Kim, S. Ryu, J. Seo and S. I. Seok, *Nature*, 2015, **517**, 476-480.
20. Q. Chen, H. Zhou, Z. Hong, S. Luo, H.-S. Duan, H.-H. Wang, Y. Liu, G. Li and Y. Yang, *J. Am. Chem. Soc.*, 2014, **136**, 622-625.
21. X. Li, D. Bi, C. Yi, J.-D. Décoppet, J. Luo, S. M. Zakeeruddin, A. Hagfeldt and M. Grätzel, *Science*, 2016, **353**, 58.
22. M. Xiao, F. Huang, W. Huang, Y. Dkhissi, Y. Zhu, J. Etheridge, A. Gray-Weale, U. Bach, Y.-B. Cheng and L. Spiccia, *Angew. Chem., Int. Ed.*, 2014, **53**, 9898-9903.

23. R. Garai, M. A. Afroz, R. K. Gupta and P. K. Iyer, *Adv. Sustainable Syst.*, 2020, **4**, 2000078.
24. M. Adil Afroz, N. Ghimire, K. M. Reza, B. Bahrami, R. S. Bobba, A. Gurung, A. H. Chowdhury, P. K. Iyer and Q. Qiao, *ACS Appl. Energy Mater.*, 2020, **3**, 2432-2439.
25. M. Saliba, J.-P. Correa-Baena, C. M. Wolff, M. Stolterfoht, N. Phung, S. Albrecht, D. Neher and A. Abate, *Chem. Mater.*, 2018, **30**, 4193-4201.
26. H. Tsai, W. Nie, Y.-H. Lin, J. C. Blancon, S. Tretiak, J. Even, G. Gupta, P. M. Ajayan and A. D. Mohite, *Adv. Energy Mater.*, 2017, **7**, 1602159.
27. R. K. Gupta, R. Garai, M. A. Afroz and P. K. Iyer, *J. Mater. Chem. C*, 2020, **8**, 8191-8198.
28. W. Nie, H. Tsai, R. Asadpour, J.-C. Blancon, A. J. Neukirch, G. Gupta, J. J. Crochet, M. Chhowalla, S. Tretiak, M. A. Alam, H.-L. Wang and A. D. Mohite, *Science*, 2015, **347**, 522.
29. K. Liao, J.-a. Yang, C. Li, T. Li and F. Hao, *ACS Appl. Mater. Interfaces*, 2019, **11**, 39882-39889.
30. C. Li, A. Wang, L. Xie, X. Deng, K. Liao, J.-a. Yang, Y. Xiang and F. Hao, *J. Mater. Chem. C*, 2020, **8**, 3217-3225.
31. H.-C. Liao, P. Guo, C.-P. Hsu, M. Lin, B. Wang, L. Zeng, W. Huang, C. M. M. Soe, W.-F. Su, M. J. Bedzyk, M. R. Wasielewski, A. Facchetti, R. P. H. Chang, M. G. Kanatzidis and T. J. Marks, *Adv. Energy Mater.*, 2017, **7**, 1601660.
32. S. Colella, E. Mosconi, G. Pellegrino, A. Alberti, V. L. P. Guerra, S. Masi, A. Listorti, A. Rizzo, G. G. Condorelli, F. De Angelis and G. Gigli, *J. Phys. Chem. Lett.*, 2014, **5**, 3532-3538.
33. A. T. Mallajosyula, K. Fernando, S. Bhatt, A. Singh, B. W. Alphenaar, J.-C. Blancon, W. Nie, G. Gupta and A. D. Mohite, *Appl. Mater. Today*, 2016, **3**, 96-102.
34. M. A. Afroz, R. K. Gupta, R. Garai, M. Hossain, S. P. Tripathi and P. K. Iyer, *Org. Electron.*, 2019, **74**, 172-178.
35. W. Nie, H. Tsai, J.-C. Blancon, F. Liu, C. C. Stoumpos, B. Traore, M. Kepenekian, O. Durand, C. Katan, S. Tretiak, J. Crochet, P. M. Ajayan, M. Kanatzidis, J. Even and A. D. Mohite, *Adv. Mater.*, 2018, **30**, 1703879.
36. R. García-Rodríguez, D. Ferdani, S. Pering, P. J. Baker and P. J. Cameron, *J. Mater. Chem. A*, 2019, **7**, 22604-22614.
37. T. Baumeler, N. Arora, A. Hinderhofer, S. Akin, A. Greco, M. Abdi-Jalebi, R. Shivanna, R. Uchida, Y. Liu, F. Schreiber, S. M. Zakeeruddin, R. H. Friend, M. Graetzel and M. I. Dar, *J. Phys. Chem. Lett.*, 2020, **11**, 10188-10195.
38. Y. Zhang, P. Wang, X. Yu, J. Xie, X. Sun, H. Wang, J. Huang, L. Xu, C. Cui, M. Lei and D. Yang, *J. Mater. Chem. A*, 2016, **4**, 18509-18515.
39. W. Zhang, L. Wan, S. Fu, X. Li and J. Fang, *J. Mater. Chem. A*, 2020, **8**, 6546-6554.
40. Q. Wang, B. Chen, Y. Liu, Y. Deng, Y. Bai, Q. Dong and J. Huang, *Energy Environ. Sci.*, 2017, **10**, 516-522.
41. C.-H. Chiang and C.-G. Wu, *ChemSusChem*, 2016, **9**, 2666-2672.
42. H. B. Lee, N. Kumar, M. M. Ovhal, Y. J. Kim, Y. M. Song and J.-W. Kang, *Adv. Funct. Mater.*, 2020, **30**, 2001559.
43. H. B. Lee, N. Kumar, B. Tyagi, K.-J. Ko and J.-W. Kang, *Solar RRL*, 2021, **5**, 2000589.

Chapter 4

Ambient Stable Perovskite Solar Cell through Trifluoro Acetic Acid-mediated Multifunctional Anchoring

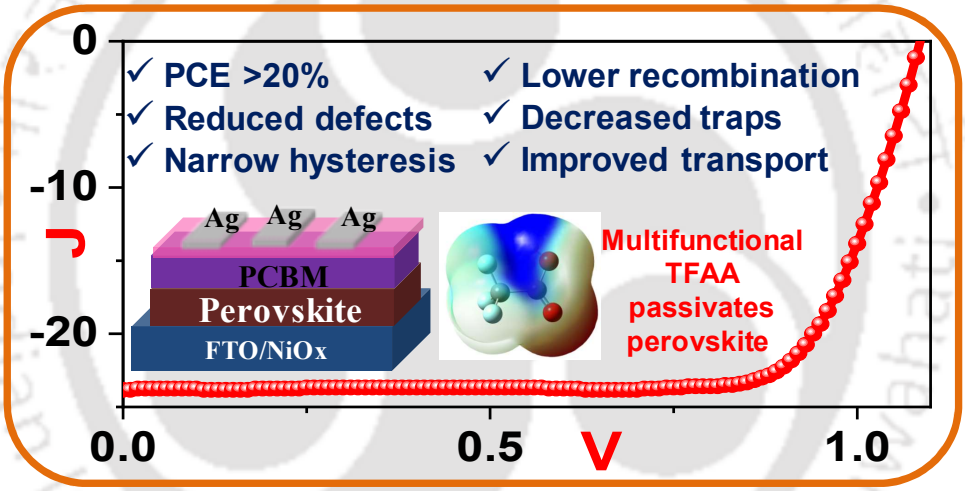

Manuscript: **Ritesh Kant Gupta,** Rabindranath Garai, Parameswar Krishnan Iyer, "Ambient Stable Perovskite Solar Cell through Trifluoro Acetic Acid-mediated Multifunctional Anchoring", *ACS Appl. Energy Mater.*, **2022**, 5, 1571–1579.

[This page was intentionally left blank]

Abstract

The functional groups of any organic materials play a key role in improving the efficiency and stability of hybrid perovskite solar cells (PSCs). This has led to the use of multifunctional organic molecules for the passivation of perovskites. Herein, trifluoro acetic acid (TFAA) has been reported as an additive for the efficient passivation of perovskite for use in PSCs applications. TFAA interacts with perovskites to passivate the defect states efficiently and enhance the device performances. The power conversion efficiency (PCE) of the champion device was found to be 20.10%, which improved from 15.08% of the control device without any TFAA. This enhancement resulted due to efficient perovskite passivation, improved crystallinity and film forming ability which was confirmed by various studies like DFT, FTIR, FESEM and XRD. The decrease in defects and trap density was proved by UV-vis, PL, EIS and other relevant analysis resulting in better charge generation, reduced recombination, and better charge transport. The fluorinated additive improves the hydrophobicity of the perovskite layer and boosts the ambient stability of the device.

4.1 Overview

Perovskite solar cells (PSCs) have seen immense growth in terms of power conversion efficiency (PCE) since 2009,[1] with the PCEs moving >25% owing to advantages such as broad absorption, color tunability, longer carrier lifetimes, long diffusion length, etc.[2-4] Moreover, PSCs can be solution-processed and can be fabricated using the roll-to-roll technique which offers a huge possibility for its commercial realization.[5-8] However, achieving stability comparable to the inorganic solar cells for the perovskite based photovoltaic devices remains a stiff challenge.[9, 10] Research has been taking place in various directions to improve both PCE and stability of the PSCs.[11-15] Passivating perovskite layer for the reduction of defects to curtail ion-migration is one of the best-known and commonly-used methods in laboratory scale to enhance the device performance.[16, 17] Many strategies have been utilized for the passivation of perovskite at the bulk, surface and interfaces.[18-22] Among all the approaches, the addition of additives in the precursor solution for the complete passivation of bulk perovskite layer is widely used in comparison to surface additive treatment (recrystallization process).[23-30] It offers an advantage of crystallization control throughout the perovskite formation process and passivates the defects at the surface and bulk.

Various small molecules and polymers have been used for the passivation of perovskites.[31-35] These organic materials possess functional groups that play a crucial role in the enhancement of the PSC device performance. Among various organic molecules the one with carboxylic acid functional groups are most commonly used as they are known to interact efficiently with defects in the perovskite layer.[36-38] Acetic acid is also utilized to passivate perovskite either in the bulk or by using it in the anti-solvent step at the surface.[39, 40] Also, fluoro group containing organic materials as additive in precursor solution makes the perovskite moisture resistant improving the ambient stability of the device. Besides, the fluoro groups are known to slow the crystallization process which helps in the formation of large grain perovskite films with improved crystallinity.[41-43] Importantly, many multifunctional additives have been used to passivate the perovskite for increasing both efficiency and stability of PSCs,[44-48] however, the role of both carboxylic acid and fluoro groups are not well explored together for the passivation of perovskite in solar cell application. Such strategic passivating agents can offer multiple advantages such as

interaction with perovskite for reducing defects, increasing its hydrophobicity and formation of large grain polycrystalline perovskite films.

In this work, trifluoro acetic acid (TFAA) has been utilized to passivate the perovskite layer for the fabrication of PSCs which significantly improved the device performance and stability. At first, various concentrations [0 µL/mL (control), 1 µL/mL (1TFAA), 2 µL/mL (2TFAA) and 3 µL/mL (3TFAA)] of TFAA had been added to the precursor solutions and perovskite films were coated using the one-step anti-solvent method. The film with 2 µL/mL of TFAA (2TFAA) displayed highest crystallinity and largest grain size. Moreover, PSCs fabricated with 2TFAA displayed highest PCE of 20.10% which improved from 15.08% of the control device without any TFAA. All the device parameters namely, open circuit voltage (*V*oc), short-circuit current density (*J*sc) and fill factor (FF) improved which contributed in the overall PCE enhancement. The modified perovskite films resulted in reduced defect and trap density which allowed higher charge generation rate and transport in the solar cell devices compared to the control device. The TFAA-modified PSCs also displayed superior ambient stability compared to the control device due to the increased hydrophobicity.

4.2 Experimental Section

4.2.1 Materials

Fluorine doped tin oxide (FTO) coated glass (7Ω/sq.), Lead iodide (PbI_2,99%), Trifluoro acetic acid (TFAA, >99%) anhydrous DMF, anhydrous DMSO, Rhodamine-101 and silver was purchased from Sigma Aldrich. Methylammonium iodide (MAI, 99%) was purchased from Greatcell Solar. (6,6)-Phenyl-C61-butyric Acid Methyl Ester (PCBM, >99.5%) was purchased from LUMTEC for electron transport layer. All the materials were used as received until otherwise specified.

4.2.2 Device Fabrication

The solar cell devices were fabricated on FTO coated glass which was pre-patterned and cleaned sequentially in soap solution, de-ionized water, acetone and isopropanol. The substrate was then dried under N_2 gas and UV-ozone treated before further processing. NiOx precursor solution for hole-transporting layer was prepared by dissolving 1M Nickel nitrate hexahydrate and 1M Ethylenediamine in 1mL Ethylene Glycol. Then the NiOx layer was

coated as hole transporting layer on the cleaned FTO. NiOx precursor solution was spin coated onto the FTO substrates at 3000 rpm for 40 sec. Afterwards the substrates were post-annealed at 300 °C for 60 min in ambient air. The $MAPbI_3$ precursor solution was prepared in a glovebox by dissolving MAI and PbI_2 was mixed in the ratio 1:1 (Molar concentration 1.26) in γ-Butyrolactone and DMSO (7:3, v/v) The solution was heated overnight prior to spin coating. For the modified device, different concentrations of TFAA additive were added to the precursor solution [0 µL/mL (control), 1 µL/mL (1TFAA), 2 µL/mL (2TFAA) and 3 µL/mL (3TFAA)]. The precursor solution was spin coated on the NiOx coated FTO in a two-step spin coating process i.e. 750 rpm for 20 sec and 4000 rpm for 60 sec. In the second step 160 mL anhydrous Toluene was dripped after 20 sec as antisolvent and after that the substrates were annealed at 80° C for 10 min. 12 mg/mL PCBM in chlorobenzene was used as electron transport layer which was spin-coated at 1200 rpm for 30 sec on top of perovskite. Lastly, thin layer of rhodamine-101 in isopropanol was spin-coated at 4000 rpm for 30 sec. 100 nm of Ag was used at cathode metal was vacuum deposited at 10^{-6} mbar pressure. The overall device architecture was FTO/NiOx/Perovskite/PCBM/Rhodamine-101/Ag.

4.2.3 Characterization

Density functional theory (DFT) was performed for the ESP analysis by using popular B3LYP/6-31G set. The perovskite films were characterized by X-ray diffraction (XRD, Rigaku Micromax-007HF diffractometer equipped with Cu Kα1 irradiation [λ =1.54184 Å]), UV–vis absorption spectroscopy (PerkinElmer Lambda-35), field emission scanning electron microscopy (FESEM, JEOL JSM-7610F), and. The current density−voltage ($J-V$) characteristic curves were recorded with a Keithley 2400 source meter in argon atmosphere for dark characterization. All light characterization was done by illuminating the device with a solar simulator (Newport, Oriel Sol 3A solar simulator, AM 1.5G, 100 mW cm^{-2}) using a shadow mask. The steady state current analysis, Mott-Scottky and impedance spectroscopic measurement were performed using an electrochemical workstation (CH Instruments 760D). An Oriel IQE-200 instrument was used to record the incident photon-to-current efficiency (IPCE) in ambient condition.

4.3 Results and Discussions

Electro-static potential mapping (Figure 4.1a) using DFT was performed to confirm possible interaction of TFAA with perovskite. From these studies it was concluded that the carbonyl groups are electronegative in nature and can passivate the defects of perovskite. To further validate this, Fourier transform infrared spectroscopy (FTIR) was performed (Figure 4.1b). The pure TFAA sample displayed asymmetric vibration of the C=O bond at 1744 cm^{-1}. However, when TFAA was added with perovskite the asymmetric vibration of the C=O bond shifted to1728 cm^{-1} as displayed from the magnified figure (right) confirming that the C=O bond strength is reduced due to the interaction with perovskite.[44]

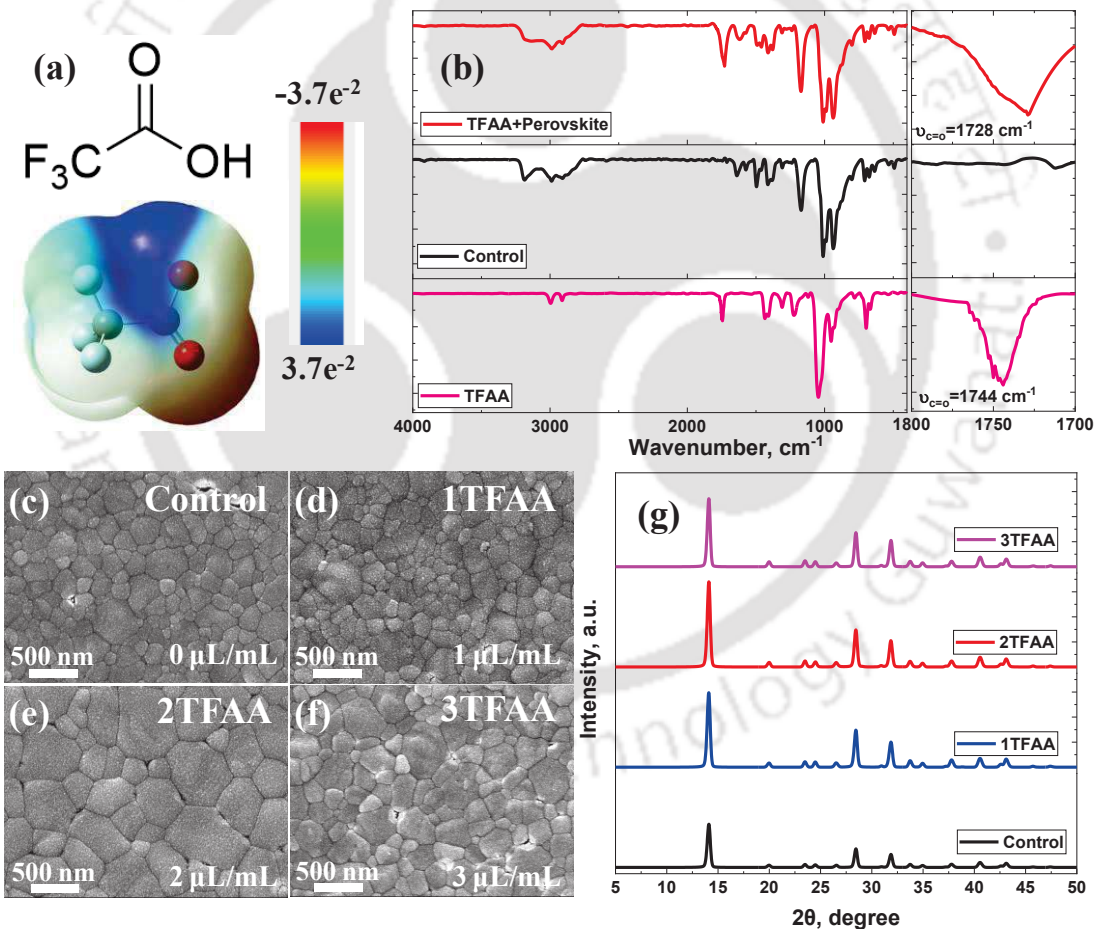

Figure 4.1: (a) Chemical structure and ESP profile of TFAA, (b) FTIR spectra of TFAA, Control and TFAA+Perovskite, FESEM images of (c) control, (d) 1TFAA, (e) 2TFAA, (f) 3TFAA, and (g) XRD of all perovskite films.

Thereafter, varying concentration of TFAA was introduced in the precursor solution and the perovskite films were coated using the one-step anti-solvent method (explained in details in the experimental section of the supplemental file). Field emission scanning electron microscopy (FESEM) and x-ray diffraction (XRD) study was performed to confirm the role of TFAA in the formation of good quality film with improved crystallinity (Figure 4.1c-g). From FESEM, it is clear that TFAA in small quantity can be helpful in modulating the perovskite grain size. It was observed that the control film, without any TFAA, exhibited small grain size which initially increased slightly with small addition of TFAA (1TFAA). With increasing concentration up to 2TFAA, the films displayed larger grain size. TFAA resulted in merger of grains through defects passivation at the grain boundaries, hence increasing the grain size. However, on further increasing the concentration, up to 3TFAA, reduced grain size was formed, likely due to overcrowding of TFAA molecules in the perovskite precursor. Likewise, all the perovskite films displayed the polycrystalline perovskite peaks for 110, 220 and 310 planes at 14.10˚, 28.44˚ and 31.86˚ 2θ values, respectively. However, the peak intensity for 2TFAA film was the highest confirming it to be the most crystalline among its counterparts. Thus the defect-free perovskite films display improved crystallinity as observed in this case. The increase in the grain size due to TFAA-incorporation is possibly due to the recrystallization process.

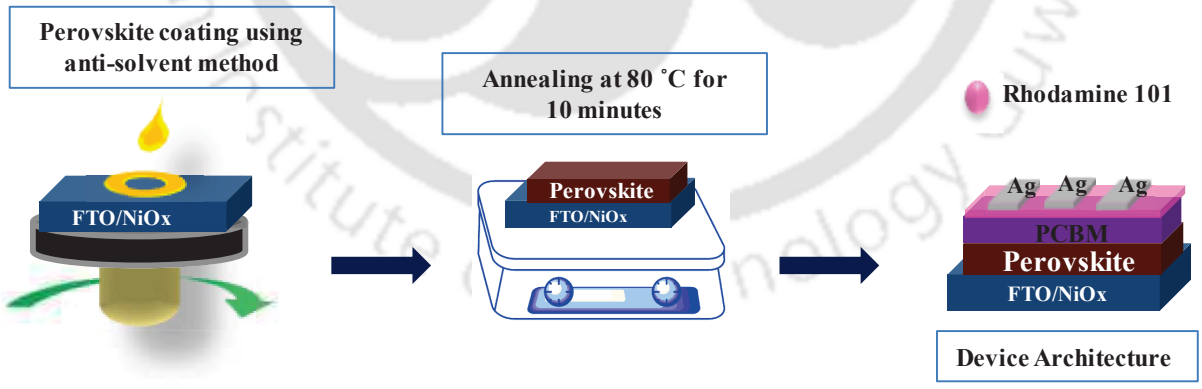

Figure 4.2: Steps of perovskite solar cell device fabrication with and without TFAA.

After confirming that TFAA plays a key role in modulating the grain size, film quality and crystallinity of perovskite films, p-i-n architecture solar cell devices were fabricated (Figure 4.2, details present in experimental section). The control device displayed

a highest PCE of 15.08% with *J*sc = 21.25 mA cm^{-2}, *V*oc = 1.001 V and FF = 71%. The PCE increased on increasing the concentration of TFAA and the champion PCE of 20.10% (*J*sc = 23.83 mA cm^{-2}, *V*oc = 1.086 V and FF = 78%) was obtained for 2TFAA device. There was improvement in all the device parameters due to formation of better quality perovskite films with large grains and enhanced crystallinity on addition of TFAA. However, for 3TFAA the PCE reduced to 18.11% which exhibited a drop in *J*sc and FF, while the *V*oc improved slightly compared to 2TFAA (Figure 4.3a, Table 4.1). The drop in *J*sc and FF for higher concentration of TFAA may be attributed to the reduction in the grain size of the perovskite film due to overcrowding of the additives. External quantum efficiency (EQE) measurement of the control and 2TFAA device confirmed that more number of photo-generated charges gets collected at the electrodes for the modified device (Figure 4.3b). The integrated *J*sc values were calculated from the EQE spectra for control and TFAA-modified device and the result was well-correlated to the *J*sc values of the *J*-*V* graph. This confirms that the charge transport improved as a result of TFAA interaction with perovskite and passivation of defects.

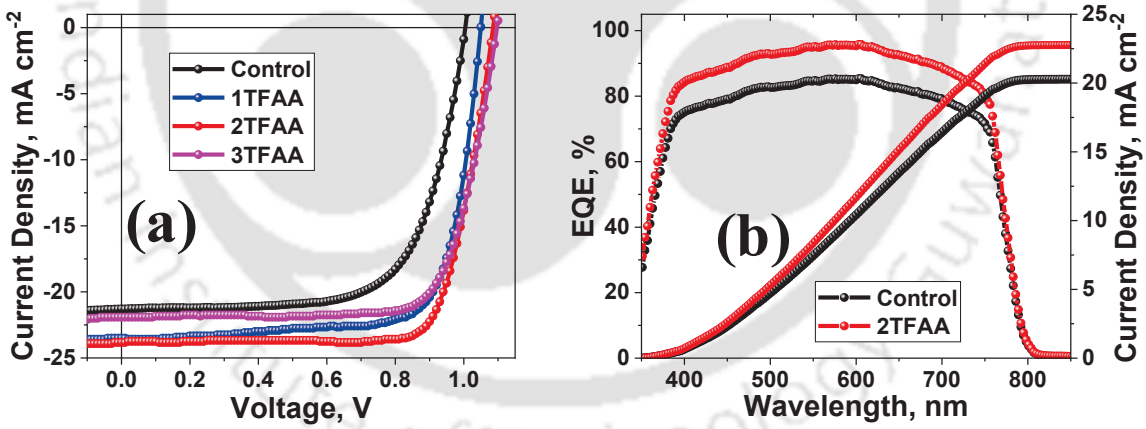

Figure 4.3: (a) *J*-*V* graphs of the best devices of each type, and (b) EQE and Integrated *J*sc spectra of control and 2TFAA.

Box chart (Figure 4.4) shows the variation of 15 devices of each type and confirmed that 2TFAA device displayed highest PCE and the improvement in PCE was a result of increase in all three device parameters, i.e., *J*sc, *V*oc and FF. *J*sc and FF improved due to enhanced grain size, while film quality and *V*oc improved due to reduced recombination as an outcome of defect passivation.

Table 4.1: Photovoltaic parameters of the fabricated devices.

Device	*J*sc, mA-cm^{-2}	*V*oc, V	FF, %	PCE (average)[a], %
Control	21.25	1.001	70.9	15.08 (13.55±0.69)
1TFAA	23.50	1.051	74.9	18.49 (17.51±0.49)
2TFAA	23.83	1.086	77.7	20.10 (19.54±0.25)
3TFAA	21.92	1.097	75.3	18.11 (16.71±0.49)
2AA	21.38	1.061	70.5	15.98 (15.17±0.61)

[a]Average and standard deviation of 15 devices.

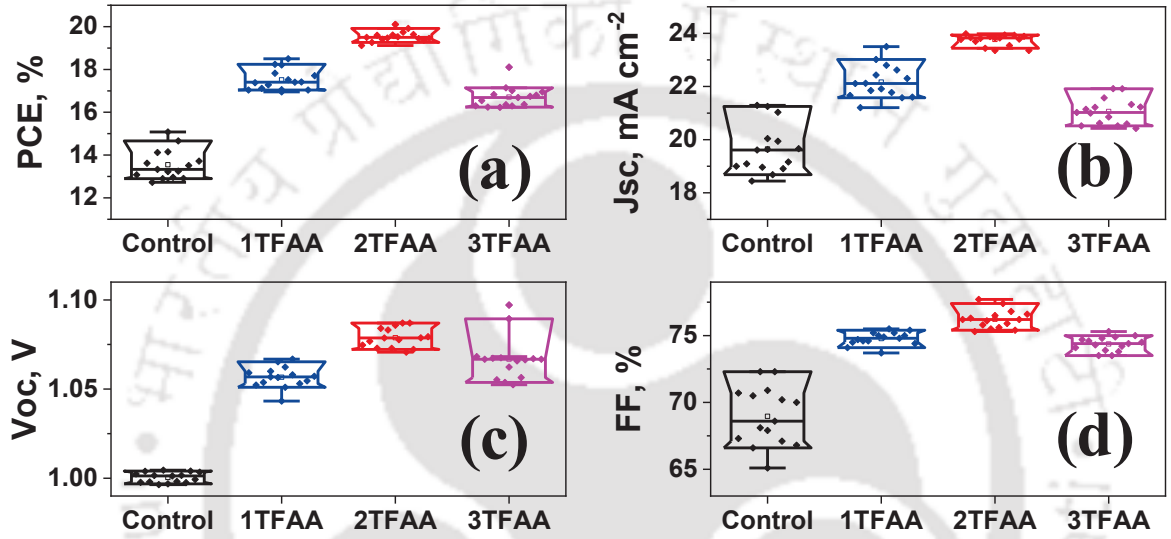

Figure 4.4: Box chart presenting device parameters variation for 15 devices of each type (a) PCE, (b) *J*sc, (c) *V*oc, and (d) FF.

Again, solar cell device was fabricated with acetic acid (2AA) for comparison with 2TFAA, and to confirm whether improvement in the photovoltaic parameters was due to the carboxylic acid group or the fluoro groups or both groups helped in the process. The highest PCE obtained for 2AA device was 15.98% (Figure 4.5a, Table 4.1), slightly more than the report from literature with AA, but certainly lower than the TFAA champion device.[39] This confirmed that both the functional groups played key roles in achieving PCE beyond 20%. FESEM for 2AA film (Figure 4.5b) showed increase in the grain size, which largely overlapped with each other. Also, these non-uniform grains would have resulted in recombination of the charges. Hence, lower FF and *V*oc were obtained for 2AA device compared to 2TFAA. The box-chart also confirms that the variation in the 2AA devices were more compared to the 2TFAA devices which may be due to the non-uniformity of the 2AA-perovskite film (Figure 4.5c).

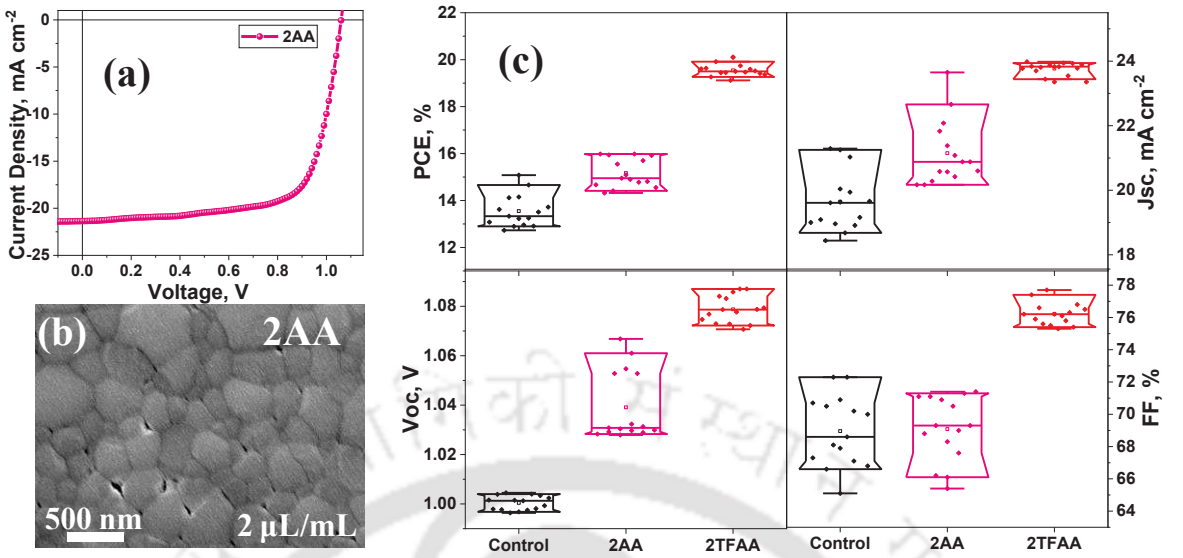

Figure 4.5: (a) *J-V* graph of 2AA, (b) FESEM image of 2AA, and (c) Box chart for comparing the results of 2AA with control & 2TFAA.

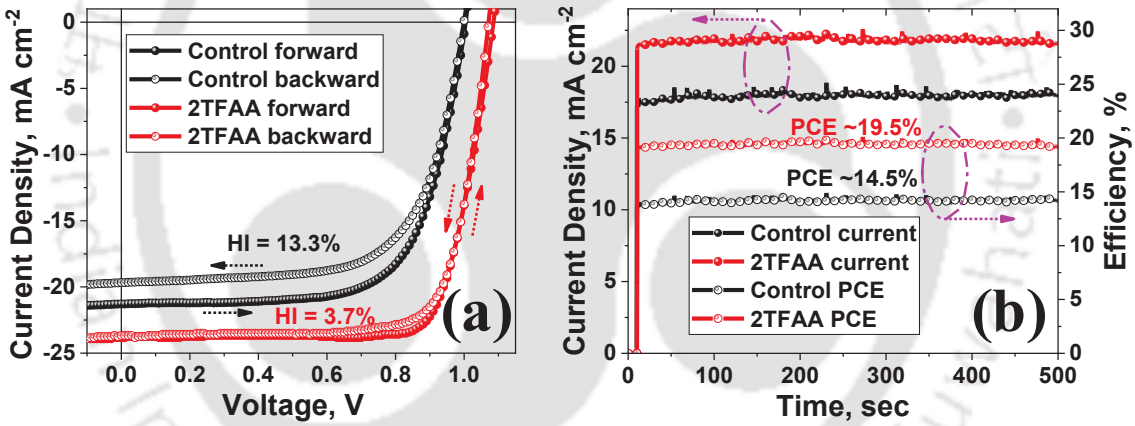

Figure 4.6: (a) Hysteresis study of control and 2TFAA, and (b) Steady state analysis of control and 2TFAA.

A major problem of perovskite solar cells is ion-migration which results in hysteresis in the forward and reverse scans of *J-V* results. To confirm if TFAA is assisting in minimizing ion-migration of the device, hysteresis study was performed by taking the forward and reverse scans of *J-V* (Figure 4.6a). It can be observed that the difference between the directional scans reduced drastically for the modified device as a result of defect passivation and the hysteresis index (HI) calculated for the modified device was only 3.7% which was lesser compared to the control device with HI = 13.3%. Thereafter, steady state current analysis (Figure 4.6b) also confirmed a stable PCE of >19.5% for the TFAA-

modified device for 500 sec. Even the control device displayed a stable PCE of ~14.5% confirming the device was well optimized before modifying it with TFAA.

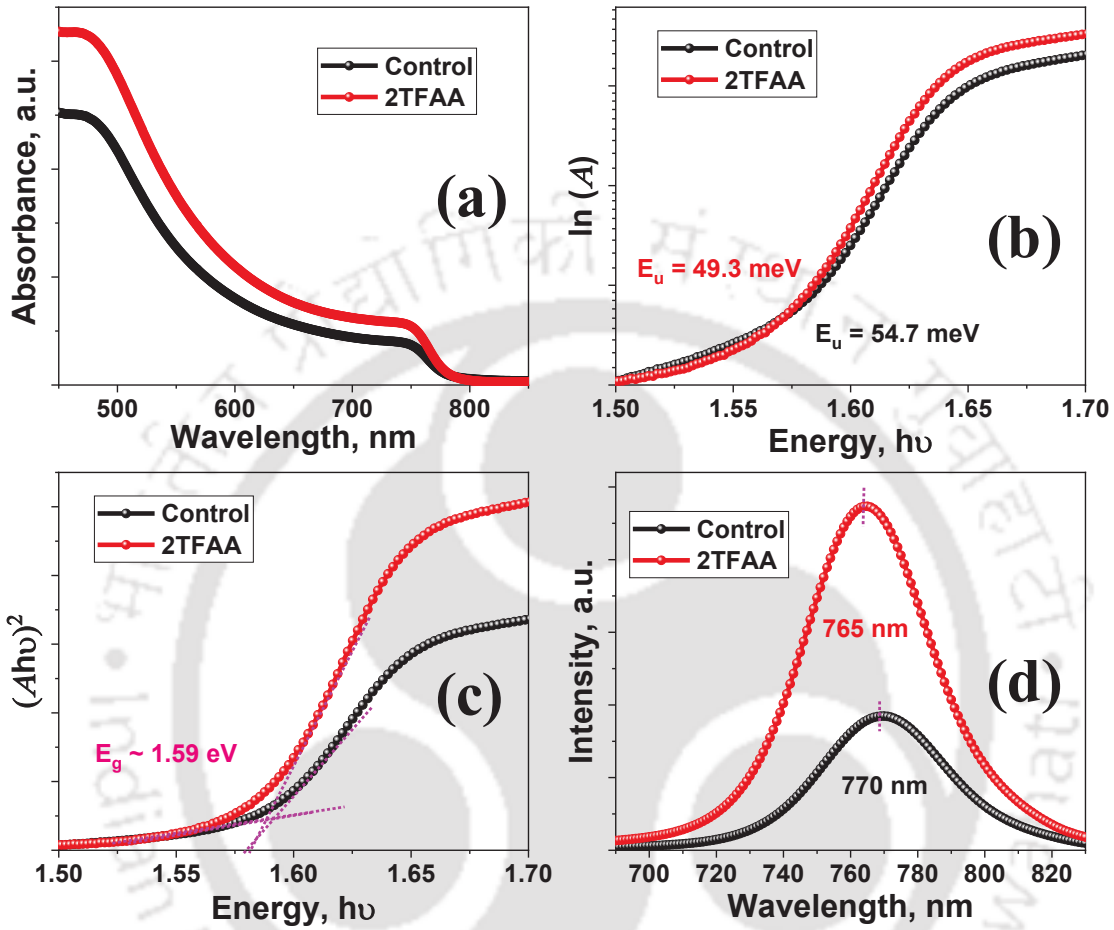

Figure 4.7: (a) UV-absorption profile, (b) ln (*A*) versus energy plot, (c) Tauc plot, and (d) Steady state PL.

Thereafter, various experimental comparative studies were carried out to understand the improvement in the device performance of 2TFAA compared to the control. Firstly, UV-vis absorption profiles (Figure 4.7a) of both films were taken and it was observed that the spectra were of typical $MAPbI_3$ type. The TFAA-modified film showed improved absorption compared to control which can be attributed to the improved quality of the perovskite film. This resulted in better photon harvesting due to which an enhancement in *J*sc of the 2TFAA device compared to the control device was recorded.[49] From the ln (*A*) versus photon energy plot the Urbach energy (E_u) was calculated from the inverse slope at the band-edge (Figure 4.7b). The E_u for the control and 2TFAA perovskite film was found to be 54.7 and 49.3 meV, respectively. The reduction in the Eu value for the 2TFAA films confirms that the defect

states in the perovskite has reduced with the incorporation of TFAA and as a consequence improved PCE is obtained compared to the control device.[50] Thereafter, Tauc plot (Figure 4.7c) was taken to ensure that there is no change in the bandgap of the perovskite without and with TFAA incorporation and it was found to be similar of ~1.59 eV. An increase in photoluminescence (PL) was also obtained for TFAA-modified film compared to the control film suggesting curtailment in non-radiative recombination of the photo-generated charges (Figure 4.7d). The slight blue-shift of the TFAA-modified film to 765 nm from 770 nm of the control film indicates passivation of the perovskite film.[51]

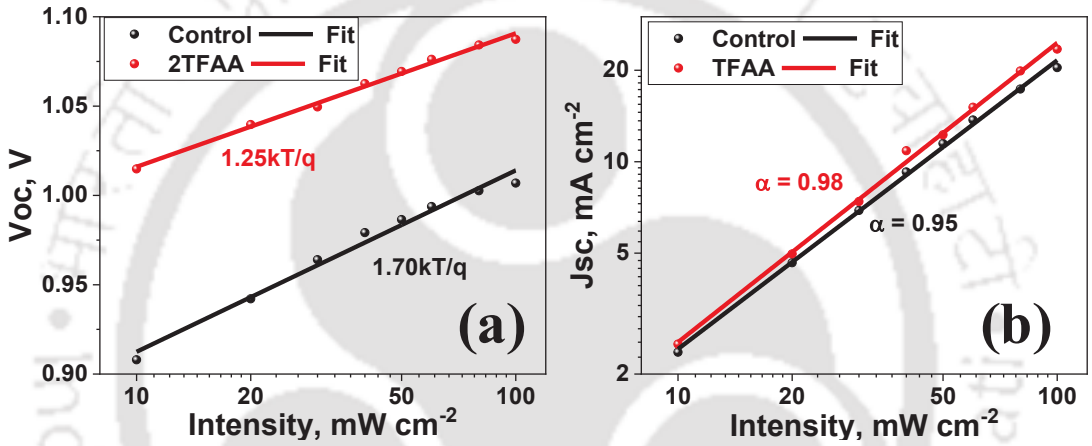

Figure 4.8: a) *V*oc versus light intensity plot, and (b) *J*sc versus light intensity plot.

Various experiments were then carried out to study in detail about the traps, recombination and charge transport. Firstly, light intensity dependent *V*oc and *J*sc variation were done (Figure 4.8a, b) and from the respective plots the value of ideality factor (n) and α were estimated for the device without and with TFAA. The values of n for control and TFAA-modified device were computed to be 1.70 and 1.25 respectively. For the control device higher n value (closer to 2) suggests presence of Shockley–Read–Hall recombination mechanism mostly due to deep trap states. However, TFAA-modified device had lower n value (closer to 1) which suggests presence of molecular or bimolecular recombination likely due to the shallow trap states. From the log-log plot of *J*sc and light intensity, the α value was computed to be 0.95 and 0.98 for control and TFAA-modified device. TFAA-modified device displayed α value closer to 1 compared to control suggesting minimum bimolecular or non-radiative recombinational loss.[52]

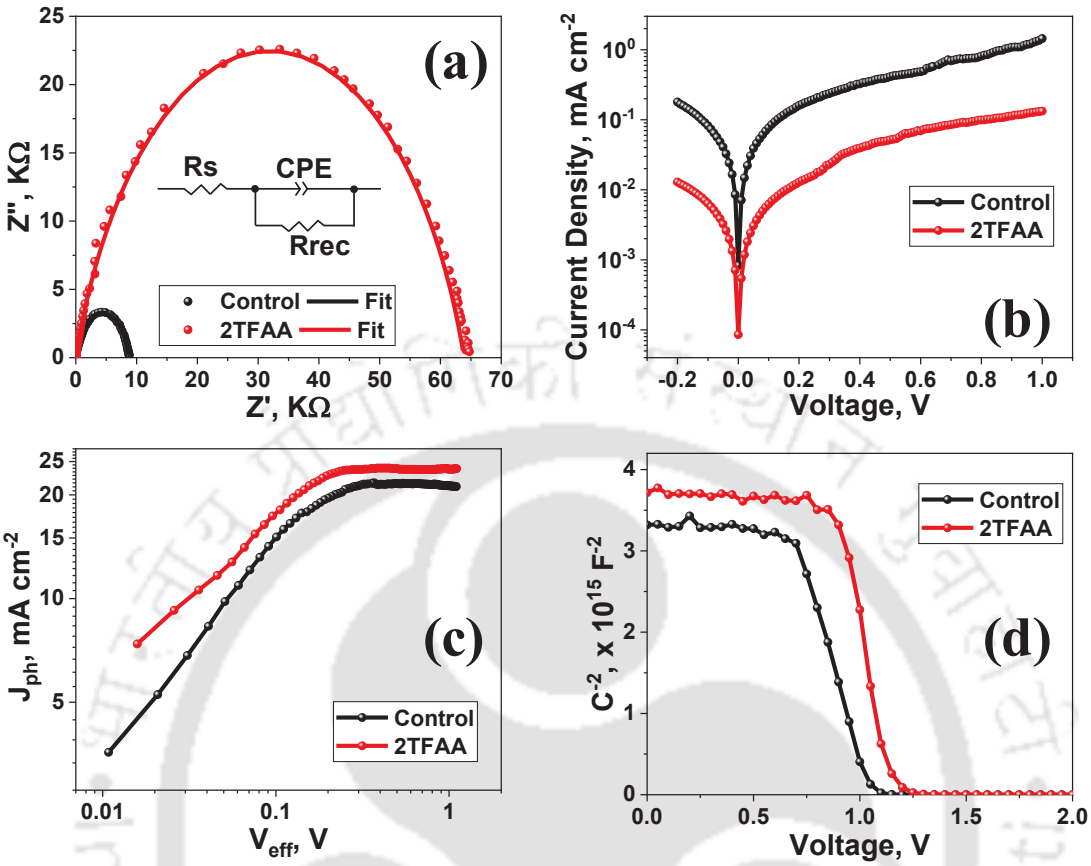

Figure 4.9: (a) EIS spectra, (b) Dark *J-V* graphs, (c) J_{ph} versus V_{eff} plots.and (d) Mott-Schottky plot.

To understand in detail about transport of the photo-generated charges, at first, EIS spectra (Figure 4.9a) for the control and modified device was recorded at 0.75 V. The spectra were fitted with the circuit as shown in the inset of the figure. It can be well-observed that the recombination resistance for the modified device increased many folds with respect to the control device ensuring least recombinational current loss due to the reduced defects and trap density. The increase in recombination resistance could be a possible reason for improvement of *V*oc in the TFAA-modified device.[53, 54] The dark *J-V* graphs (Figure 4.9b) of the PSC device also showed lower reverse saturation current for 2TFAA compared to control device. The photonic current (J_{ph}) calculated from the difference of the light and dark *J-V* graphs also showed higher J_{ph} for 2TFAA with respect to control device (Figure 4.9c). This confirms higher generation rate of the photo-generated charges in the TFAA-modified devices. Later, from the Mott-Schottky (MS) plot (Figure 4.9d) the residual charge density (N) was calculated from the slope. The values of N for the control and 2TFAA devices were

estimated to be 3.10 x 10^{16} and 2.02 x 10^{16} cm^{-3}, respectively. Thus, it can be easily concluded that TFAA-modified device has better charge transport compared to the control device. This was due to the reduced recombinational loss in the modified device which displayed good perovskite film formation, reduced defect and trap density. Also, from the MS plot it can be concluded that the built-in potential of the TFAA-modified device has increased which may be a reason for increase in the *V*oc of the 2TFAA solar cell devices.[55]

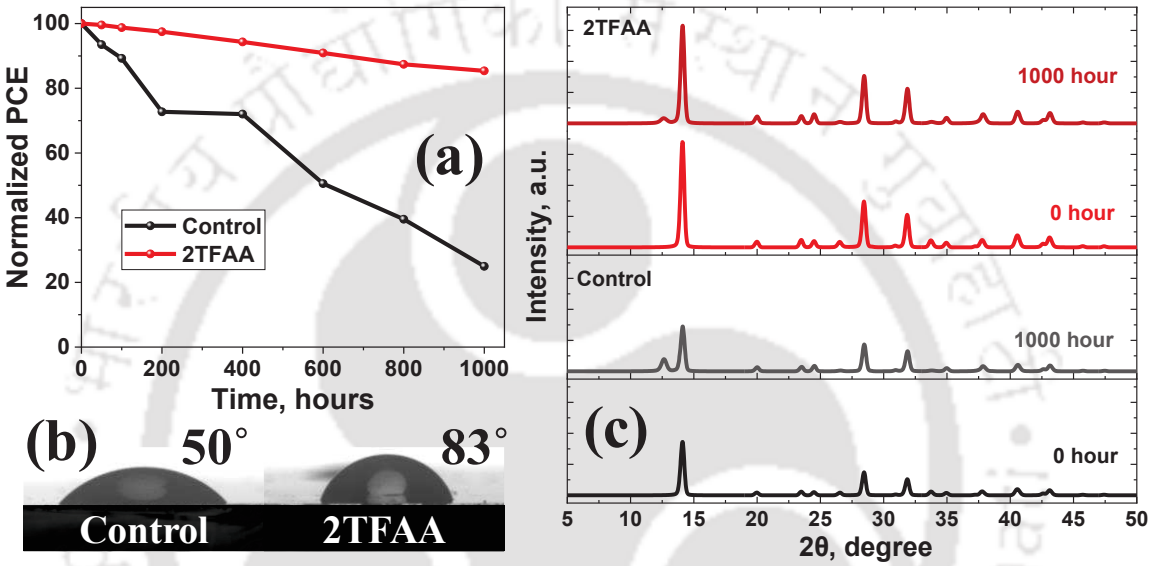

Figure 4.10: (a) Ambient stability study of the control and 2TFAA device, (b) Contact angles, and (c) XRD of the perovskite films kept in ambient condition.

Finally, the issue of stability in the perovskite device was addressed using TFAA modification. Stability study (Figure 4.10a) was performed at relative humidity of 40±5% and the TFAA-modified device was found to be superior to the control device under ambient conditions (room temperature, relative humidity 40±5%). After 1000 hours, the TFAA-modified device retained 85% of its initial PCE, whereas the control device reduced to less than 25% of its initial PCE. Contact angle analysis was performed to confirm the stability of the perovskite films with water droplet (Figure 4.10b). It was found that the TFAA-modified film was more hydrophobic than the control, hence more moisture resistance was observed in the 2TFAA device. Likewise, the XRD spectra of the perovskite films (Figure 4.10c) kept in ambient confirmed presence of PbI_2 peak with more intensity for control, which was very small in scale for 2TFAA.[42]

4.4 Conclusion

In summary, multifunctional TFAA has been utilized as a perovskite passivating agent that significantly improved the quality of the film and its crystallinity. TFAA-modified perovskite was also used in fabricating p-i-n architecture solar cell device and champion PCE>20% was obtained. This was improved from 15.08% PCE for the control device without any TFAA. The photovoltaic results were highly repeatable with least variation of all parameters. It was also proven that both the carboxylic acid and the fluoro groups had individual role in improving the device parameters and achieving PCE beyond 20%. The modified device displayed improved absorbance, reduced defects and non-radiative recombination of the charges. Various trap studies confirmed the presence of deep trap states for the control device which was reduced for the TFAA-modified device confirming trap passivation of the perovskite. This resulted in reduced hysteresis in the modified PSC device. Also, the photo-generated charges increased and the charge transport improved for the 2TFAA device compared to the control device. Consequently, the device with 2TFAA displayed superior ambient stability due to the increased hydrophobicity of the perovskite film. Hence, this method is a very useful technique in passivating PSC device using multifunctional economical small molecules and achieving high PCE and stability.

References

1. A. Kojima, K. Teshima, Y. Shirai and T. Miyasaka, *J. Am. Chem. Soc.*, 2009, **131**, 6050-6051.
2. National Renewable Energy Laboratory, Best research-cell efficiencies chart, https://www.nrel.gov/pv/assets/pdfs/best-research-cell-efficiencies.20200104.pdf, (accessed 28.04.2021).
3. N. K. Tailor, M. Abdi-Jalebi, V. Gupta, H. Hu, M. I. Dar, G. Li and S. Satapathi, *J. Mater. Chem. A*, 2020, **8**, 21356-21386.
4. S. D. Stranks, G. E. Eperon, G. Grancini, C. Menelaou, M. J. P. Alcocer, T. Leijtens, L. M. Herz, A. Petrozza and H. J. Snaith, *Science*, 2013, **342**, 341.
5. X. Hu, Z. Huang, X. Zhou, P. Li, Y. Wang, Z. Huang, M. Su, W. Ren, F. Li, M. Li, Y. Chen and Y. Song, *Adv. Mater.*, 2017, **29**, 1703236.
6. H. Zhang, J. Cheng, F. Lin, H. He, J. Mao, K. S. Wong, A. K. Y. Jen and W. C. H. Choy, *ACS Nano*, 2016, **10**, 1503-1511.
7. Y. Hu, S. Si, A. Mei, Y. Rong, H. Liu, X. Li and H. Han, *Solar RRL*, 2017, **1**, 1600019.
8. R. K. Gupta, R. Garai, M. Hossain, A. Choudhury and P. K. Iyer, *ACS Sustainable Chemistry & Engineering*, 2021, **9**, 7993-8001.
9. D. Wang, M. Wright, N. K. Elumalai and A. Uddin, *Sol. Energy Mater. Sol. Cells.*, 2016, **147**, 255-275.
10. G. Grancini, C. Roldán-Carmona, I. Zimmermann, E. Mosconi, X. Lee, D. Martineau, S. Narbey, F. Oswald, F. De Angelis, M. Graetzel and M. K. Nazeeruddin, *Nat. Commun.*, 2017, **8**, 15684.
11. N. J. Jeon, J. H. Noh, Y. C. Kim, W. S. Yang, S. Ryu and S. I. Seok, *Nat. Mater.*, 2014, **13**, 897-903.
12. N. J. Jeon, J. H. Noh, W. S. Yang, Y. C. Kim, S. Ryu, J. Seo and S. I. Seok, *Nature*, 2015, **517**, 476-480.
13. Q. Chen, H. Zhou, Z. Hong, S. Luo, H.-S. Duan, H.-H. Wang, Y. Liu, G. Li and Y. Yang, *J. Am. Chem. Soc.*, 2014, **136**, 622-625.
14. X. Li, D. Bi, C. Yi, J.-D. Décoppet, J. Luo, S. M. Zakeeruddin, A. Hagfeldt and M. Grätzel, *Science*, 2016, **353**, 58.
15. M. Xiao, F. Huang, W. Huang, Y. Dkhissi, Y. Zhu, J. Etheridge, A. Gray-Weale, U. Bach, Y.-B. Cheng and L. Spiccia, *Angew. Chem., Int. Ed.*, 2014, **53**, 9898-9903.
16. D. Lan, *Prog. Photovoltaics Res. Appl.*, 2020, **28**, 533-537.
17. T. Zhang, H. Chen, Y. Bai, S. Xiao, L. Zhu, C. Hu, Q. Xue and S. Yang, *Nano Energy*, 2016, **26**, 620-630.
18. H. Kim, J. Lee, B. Kim, H. R. Byun, S. H. Kim, H. M. Oh, S. Baik and M. S. Jeong, *Sci. Rep.*, 2019, **9**, 15461.
19. H. Zhao, S. Wang, M. Sun, F. Zhang, X. Li and Y. Xiao, *J. Mater. Chem. A*, 2018, **6**, 10825-10834.
20. L. A. Frolova, A. I. Davlethanov, N. N. Dremova, I. Zhidkov, A. F. Akbulatov, E. Z. Kurmaev, S. M. Aldoshin, K. J. Stevenson and P. A. Troshin, *J. Phys. Chem. Lett.*, 2020, **11**, 6772-6778.
21. M. A. Afroz, R. K. Gupta, R. Garai, M. Hossain, S. P. Tripathi and P. K. Iyer, *Org. Electron.*, 2019, **74**, 172-178.

22. H. Tan, A. Jain, O. Voznyy, X. Lan, F. P. García de Arquer, J. Z. Fan, R. Quintero-Bermudez, M. Yuan, B. Zhang, Y. Zhao, F. Fan, P. Li, L. N. Quan, Y. Zhao, Z.-H. Lu, Z. Yang, S. Hoogland and E. H. Sargent, *Science*, 2017, **355**, 722.
23. L. Zhang, L. Xu, Q. Li, J. Su and J. Li, *Sol. Energy Mater. Sol. Cells.*, 2018, **186**, 349-355.
24. K. Zhu, S. Cong, Z. Lu, Y. Lou, L. He, J. Li, J. Ding, N. Yuang, M. H. Rümmeli and G. Zou, *J. Power Sources*, 2019, **428**, 82-87.
25. H. Li, R. Zhang, Y. Li, Y. Li, H. Liu, J. Shi, H. Zhang, H. Wu, Y. Luo, D. Li, Y. Li and Q. Meng, *Adv. Energy Mater.*, 2018, **8**, 1802012.
26. X. Zheng, B. Chen, J. Dai, Y. Fang, Y. Bai, Y. Lin, H. Wei, Xiao C. Zeng and J. Huang, *Nat. Energy*, 2017, **2**, 17102.
27. Q. Jiang, Y. Zhao, X. Zhang, X. Yang, Y. Chen, Z. Chu, Q. Ye, X. Li, Z. Yin and J. You, *Nat. Photonics*, 2019, **13**, 460-466.
28. L. Lin, J. T.-W. Wang, T. W. Jones, M. Grigore, A. Cook, D. W. deQuilettes, R. Brenes, B. C. Duck, K. F. Anderson, N. W. Duffy, B. Wenger, V. Bulović, J. Pu, J. Li, B. Chi, H. J. Snaith and G. J. Wilson, *J. Mater. Chem. A*, 2019, **7**, 25511-25520.
29. F. Xie, C.-C. Chen, Y. Wu, X. Li, M. Cai, X. Liu, X. Yang and L. Han, *Energy Environ. Sci.*, 2017, **10**, 1942-1949.
30. H. Dong, Z. Wu, J. Xi, X. Xu, L. Zuo, T. Lei, X. Zhao, L. Zhang, X. Hou and A. K. Y. Jen, *Adv. Funct. Mater.*, 2018, **28**, 1704836.
31. Y. Guo, J. Ma, H. Lei, F. Yao, B. Li, L. Xiong and G. Fang, *J. Mater. Chem. A*, 2018, **6**, 5919-5925.
32. C. Liu, Z. Huang, X. Hu, X. Meng, L. Huang, J. Xiong, L. Tan and Y. Chen, *ACS Appl. Mater. Interfaces*, 2018, **10**, 1909-1916.
33. L. Zuo, H. Guo, D. W. deQuilettes, S. Jariwala, N. De Marco, S. Dong, R. DeBlock, D. S. Ginger, B. Dunn, M. Wang and Y. Yang, *Sci. Adv.*, 2017, **3**, e1700106.
34. Y. Zhou, S. Mei, D. Sun, N. Liu, W. Shi, J. Feng, F. Mei, J. Xu, Y. Jiang and X. Cao, *Micromachines*, 2019, **10**.
35. T. Niu, J. Lu, R. Munir, J. Li, D. Barrit, X. Zhang, H. Hu, Z. Yang, A. Amassian, K. Zhao and S. Liu, *Adv. Mater.*, 2018, **30**, 1706576.
36. T. Wu, Y. Wang, X. Li, Y. Wu, X. Meng, D. Cui, X. Yang and L. Han, *Adv. Energy Mater.*, 2019, **9**, 1803766.
37. M. Adil Afroz, N. Ghimire, K. M. Reza, B. Bahrami, R. S. Bobba, A. Gurung, A. H. Chowdhury, P. K. Iyer and Q. Qiao, *ACS Appl. Energy Mater.*, 2020, **3**, 2432-2439.
38. R. Garai, R. K. Gupta, A. S. Tanwar, M. Hossain and P. K. Iyer, *Chem. Mater.*, 2021, **33**, 5709-5717.
39. Q. Zhao, G. R. Li, J. Song, Y. Zhao, Y. Qiang and X. P. Gao, *Sci. Rep.*, 2016, **6**, 38670.
40. Y. Li, J. Shi, J. Zheng, J. Bing, J. Yuan, Y. Cho, S. Tang, M. Zhang, Y. Yao, C. F. J. Lau, D. S. Lee, C. Liao, M. A. Green, S. Huang, W. Ma and A. W. Y. Ho-Baillie, *Adv. Sci.*, 2020, **7**, 1903368.
41. J. Xia, C. Liang, S. Mei, H. Gu, B. He, Z. Zhang, T. Liu, K. Wang, S. Wang, S. Chen, Y. Cai and G. Xing, *J. Mater. Chem. A*, 2021, **9**, 2919-2927.
42. S. Zhao, J. Xie, G. Cheng, Y. Xiang, H. Zhu, W. Guo, H. Wang, M. Qin, X. Lu, J. Qu, J. Wang, J. Xu and K. Yan, *Small*, 2018, **14**, 1803350.

43. J. Yang, C. Liu, C. Cai, X. Hu, Z. Huang, X. Duan, X. Meng, Z. Yuan, L. Tan and Y. Chen, *Adv. Energy Mater.*, 2019, **9**, 1900198.
44. R. Garai, M. A. Afroz, R. K. Gupta and P. K. Iyer, *Adv. Sustainable Syst.*, 2020, **4**, 2000078.
45. H. Zhang, Y. Wu, C. Shen, E. Li, C. Yan, W. Zhang, H. Tian, L. Han and W.-H. Zhu, *Adv. Energy Mater.*, 2019, **9**, 1803573.
46. M.-S. Lee, S. Sarwar, S. Park, U. Asmat, D. T. Thuy, C.-h. Han, S. Ahn, I. Jeong and S. Hong, *Sustainable Energy Fuels*, 2020, **4**, 3318-3325.
47. J. Chen, S.-G. Kim, X. Ren, H. S. Jung and N.-G. Park, *J. Mater. Chem. A*, 2019, **7**, 4977-4987.
48. T. Xu, K. Zou, S. Lv, H. Tang, Y. Zhang, Y. Chen, L. Chen, Z. Li and W. Huang, *ACS Appl. Mater. Interfaces*, 2021, **13**, 16485-16497.
49. M. Hossain, R. Garai, R. K. Gupta, R. N. Arunagirinathan and P. K. Iyer, *J. Mater. Chem. C*, 2021, **9**, 10406-10413.
50. W. Zhang, L. Wan, S. Fu, X. Li and J. Fang, *J. Mater. Chem. A*, 2020, **8**, 6546-6554.
51. Y. Shao, Z. Xiao, C. Bi, Y. Yuan and J. Huang, *Nat. Commun.*, 2014, **5**, 5784.
52. R. K. Gupta, R. Garai, M. A. Afroz and P. K. Iyer, *J. Mater. Chem. C*, 2020, **8**, 8191-8198.
53. X. Cao, C. Li, Y. Li, F. Fang, X. Cui, Y. Yao and J. Wei, *Nanoscale*, 2016, **8**, 19804-19810.
54. A. Choudhury, R. K. Gupta, R. Garai and P. K. Iyer, *Adv. Mater. Interfaces*, 2021, **8**, 2100574.
55. M. Zou, X. Xia, Y. Jiang, J. Peng, Z. Jia, X. Wang and F. Li, *ACS Appl. Mater. Interfaces*, 2019, **11**, 33515-33524.

[This page was intentionally left blank]

Chapter 5

Dual-passivation Strategy for Improved Ambient Stability of Perovskite Solar Cells

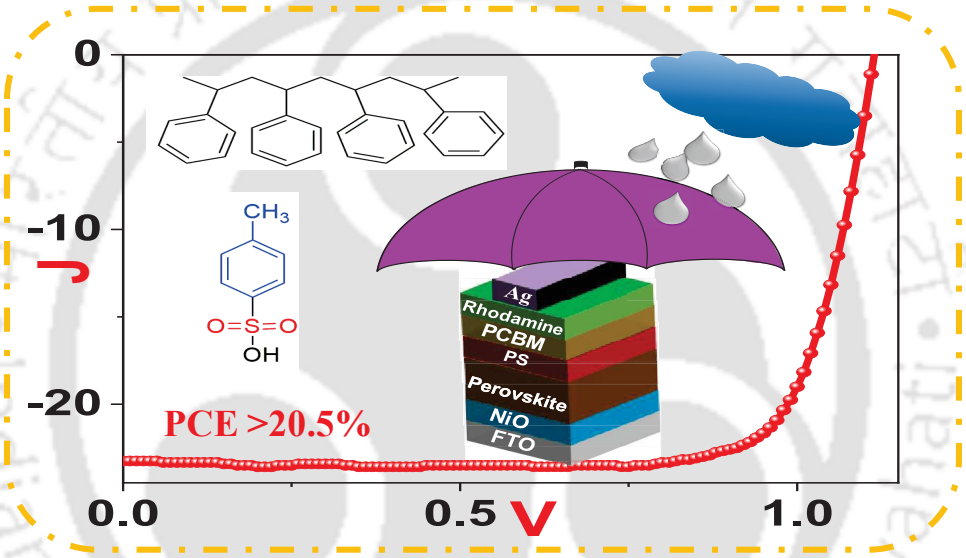

Manuscript: Ritesh Kant Gupta, Rabindranath Garai, Parameswar Krishnan Iyer, "Dual-passivation Strategy for Improved Ambient Stability of Perovskite Solar Cells", *ACS Appl. Energy Mater.*, **2021**, 4, 10025–10032.

[This page was intentionally left blank]

Abstract

Dual-passivation of $MAPbI_3$-based perovskite using p-toluenesulfonic acid (PTSA) in the bulk, and hydrophobic polystyrene (PS) at the surface significantly diminishes the trap-density, and improves the device performances substantially. Sulphonic acid functional group of PTSA interacts with the defects in perovskite and passivates the trap-states while PS repairs the surface defects and increases the moisture resistance of perovskites. Thus, improvement in perovskite crystallinity and formation of larger grain size occurs due to dual-passivation, thereby enhancing the power conversion efficiency (PCE) to 20.62% from 15.14% of the device without passivation. Notably, the large-area dual-passivated device also displays PCE ~18.5%. The modified device (PTSA2PS2) showcases reduced hysteresis and a steady state output of >20%. The PTSA2PS2-based devices exhibit higher photo-generated charges, lower charge recombination, reduced trap-density and better charge transport than the control devices. The modified device retains 93% of the original PCE after 1000 hours under ambient condition.

5.1 Overview

In only over a decade, the state-of-the-art perovskite solar cells (PSCs) have achieved new heights in the field of photovoltaic devices to compete with the currently utilized inorganic photovoltaic technology.[1, 2] Perovskite materials offer various advantages such as long carrier lifetimes, broad absorption, color tunability, long diffusion length, etc. which has pushed the power conversion efficiency (PCE) of PSC beyond 25%.[3-5] Since, PSCs can be easily solution-processed for complete fabrication, various sustainable approaches have now been integrated to develop large-area devices as well.[6-10] Many modifications are being attempted in the bulk perovskite on its surface or as interlayer to increase both the PCE and stability of the solar cell devices.[11-19] Anti-solvent treatment of the perovskite film is one of the most common methods to reduce the defects, however, only anti-solvent treatments do not ensure defect-free perovskite films for stable solar cell applications.[20-24] Among the many other strategies, addition of organic molecules in very small quantity into the precursor solution is found to be one of the most useful techniques to reduce the perovskite defects further.[25-28] A very thin layer of such materials (polymers or small molecules) is sometimes coated on top of the perovskite layer to realize the necessary passivation.[29-34] In both these approaches it has been observed that the trap-density in the perovskite reduces, which in turn provides improvement in the device stability and performance.

Organic functional molecule-assisted perovskite crystallization control has been explored for application in PSCs development. Among these molecules, acid functional groups, e.g. carboxylic acid, sulphonic acid and phosphonic acid etc. containing compounds have been largely investigated till date.[35-40] These acid groups reduce the ion-migration in the perovskite by interacting with the defects present in them, thus reducing the hysteresis of the PSCs, and also increasing their PCE as well. Sulphonic acid is also a very good anti-oxidant which tends to increase the ambient stability of the PSCs.[39] Another method to increase the moisture resistance of perovskite and the device performance of PSCs has been the use of economical hydrophobic polymers as dopant in the precursor solution or as an individual layer on top of perovskite film.[41-44] This technique has been so effective that a double layer of the hydrophobic polymer has also been coated on either side of perovskite film to provide the necessary surface passivation and charge transport for increasing the device PCE and stability.[45] However, the dual roles of (a) dopant organic molecule in the precursor solution,

and (b) thin film of hydrophobic polymer fabricated on top of perovskite layer together in one common device system using solution processing techniques have never been utilized to realize remarkable stability enhancement as well as efficiencies including those in large-area devices.

Subsequently, in this work, dual passivation of the perovskite has been strategized using p-toluenesulfonic acid (PTSA) in the precursor solution and polystyrene (PS) as a top surface layer judiciously. The sulfonic acid functional group of PTSA neutralized the defects present in the perovskite when introduced as an additive in bulk, whereas the hydrophobicity of PS assisted in making the perovskite layer moisture resistant. Varying concentration of PTSA was added in the precursor solution and a thin layer of PS was coated on top of the perovskite film by varying its concentration (Table 5.1). The films were characterized with Field emission scanning electron microscopy (FESEM) and X-ray diffraction (XRD) study to understand the modulation of grain size and crystallinity due to the dual passivation of perovskite in the bulk and at the surface. PSCs were fabricated with this approach and highest PCE of 20.62% was obtained for PTSA2PS2 device which improved from 15.14% for the control device without any passivation. The modified device showcased reduced hysteresis and steady state efficiency of >20% under illumination. The modified device also exhibited reduced recombination current which improved the charge transport due to decreased trap density of states (DOS). The PTSA2PS2 device also displayed enhanced ambient stability due to the high hydrophobicity of the modified film. Large-area dual-passivated device also demonstrated a PCE of ~18.5% confirming its utilization in future commercialization.

Table 5.1: Device/Film type based of the concentration of PTSA and PS for dual passivation strategy.

Device/Film Type	PTSA (mg/mL)	PS (mg/mL)
Control	0	0
PTSA1PS2	1	2
PTSA1PS4	1	4
PTSA2PS2	2	2
PTSA2PS4	2	4
PTSA3PS2	3	2
PTSA3PS4	3	4

5.2 Experimental Section

5.2.1 Materials

Fluorine doped tin oxide (FTO) coated glass (7Ω/sq.), Lead iodide (PbI_2,99%), p-toluene sulphonic acid (PTSA, >99%), Polystyrene (PS, >99%), anhydrous DMF, anhydrous DMSO, Rhodamine-101 and silver was purchased from Sigma Aldrich. Methylammonium iodide (MAI, 99%) was purchased from Greatcell Solar. (6,6)-Phenyl-C61-butyric Acid Methyl Ester (PCBM, >99.5%) was purchased from LUMTEC for electron transport layer. Poly(3,4-ethylenedioxythiophene)-poly(styrenesulfonate) (PEDOT:PSS, PVP AI 4083) was procured from Clevios for hole-transporting layer. All the materials were used as received until otherwise specified.

5.2.2 Device Fabrication

The solar cell devices were fabricated on FTO coated glass which was pre-patterned and cleaned sequentially in soap solution, de-ionized water, acetone and isopropanol. The substrate was then dried under N_2 gas and UV-ozone treated before further processing. NiOx precursor solution for hole-transporting layer was prepared by dissolving 1M Nickel nitrate hexahydrate and 1M Ethylenediamine in 1mL Ethylene Glycol. Then the NiOx layer was coated as hole transporting layer on the cleaned FTO. NiOx precursor solution was spin coated onto the FTO substrates at 3000 rpm for 40 sec. Afterwards the substrates were post-annealed at 300 °C for 60 min in ambient air. The $MAPbI_3$ precursor solution was prepared in a glovebox by dissolving MAI and PbI_2 was mixed in the ratio 1:1 (Molar concentration 1.26) in γ-Butyrolactone and DMSO (7:3, v/v). The solution was heated overnight prior to spin coating. For the modified device, different concentrations of PTSA additive were added to the precursor solution [1 mg/mL, 2 mg/mL and 3 mg/mL]. PS was coated on top of perovskite layer with either 2 mg/mL or 4 mg/mL concentration in chlorobenzene. The precursor solution was spin coated on the NiOx coated FTO in a two-step spin coating process i.e. 750 rpm for 20 sec and 4000 rpm for 60 sec. In the second step 160 mL anhydrous Toluene was dripped after 20 sec as antisolvent and after that the substrates were annealed at 80° C for 10 min. 12 mg/mL PCBM in chlorobenzene was used as electron transport layer which was spin-coated at 1200 rpm for 30 sec on top of perovskite. Lastly,

thin layer of rhodamine-101 in isopropanol was spin-coated at 4000 rpm for 30 sec. 100 nm of Ag as cathode metal was vacuum deposited at 10^{-6} mbar pressure. The overall device architecture was FTO/NiOx/Perovskite/PCBM/Rhodamine-101/Ag.

5.2.3 Characterization

The perovskite films were characterized by X-ray diffraction (XRD, Rigaku Micromax-007HF diffractometer equipped with Cu Kα1 irradiation [λ =1.54184 Å]), UV–vis absorption spectroscopy (PerkinElmer Lambda-35), field emission scanning electron microscopy (FESEM, JEOL JSM-7610F), and. The current density−voltage (J−V) characteristic curves were recorded with a Keithley 2400 source meter in argon atmosphere for dark characterization. All light characterization was done by illuminating the device with a solar simulator (Newport, Oriel Sol 3A solar simulator, AM 1.5G, 100 mW cm^{-2}). The steady state current analysis, Mott-Scottky and impedance spectroscopic measurement were performed using an electrochemical workstation (CH Instruments 760D). An Oriel IQE-200 instrument was used to record the incident photon-to-current efficiency (IPCE) in ambient condition.

5.3 Results and Discussions

The dual passivation of perovskite layer was carried out carefully (Figure 5.1a), where PTSA was introduced in the precursor solution for passivating the bulk and PS was spin coated above it for protecting the perovskite layer from moisture. FESEM images of all the dual passivated and control films (Figure 1b-h) showed that the grain size of the control film (without any passivation) was very small in size. However, prominent grain size increment occurred for all the modified films with largest grain size for PTSA2PS2 and PTSA2PS4 films. The film quality for the modified films improved due to the recrystallization of the perovskite grains as a result of dual passivation approach.[11] The crystallinity of all the films was verified using the XRD study (Figure 1i). All the perovskite films displayed the polycrystalline $MAPbI_3$ peaks for 110, 220 and 310 planes at 14.10º, 28.44º and 31.86º 2θ values, respectively confirming appropriate perovskite formation. Also, the improvement in the grain size of the perovskite films can be attributed to the increased crystallinity as evident for the peak intensities of the XRD spectra.

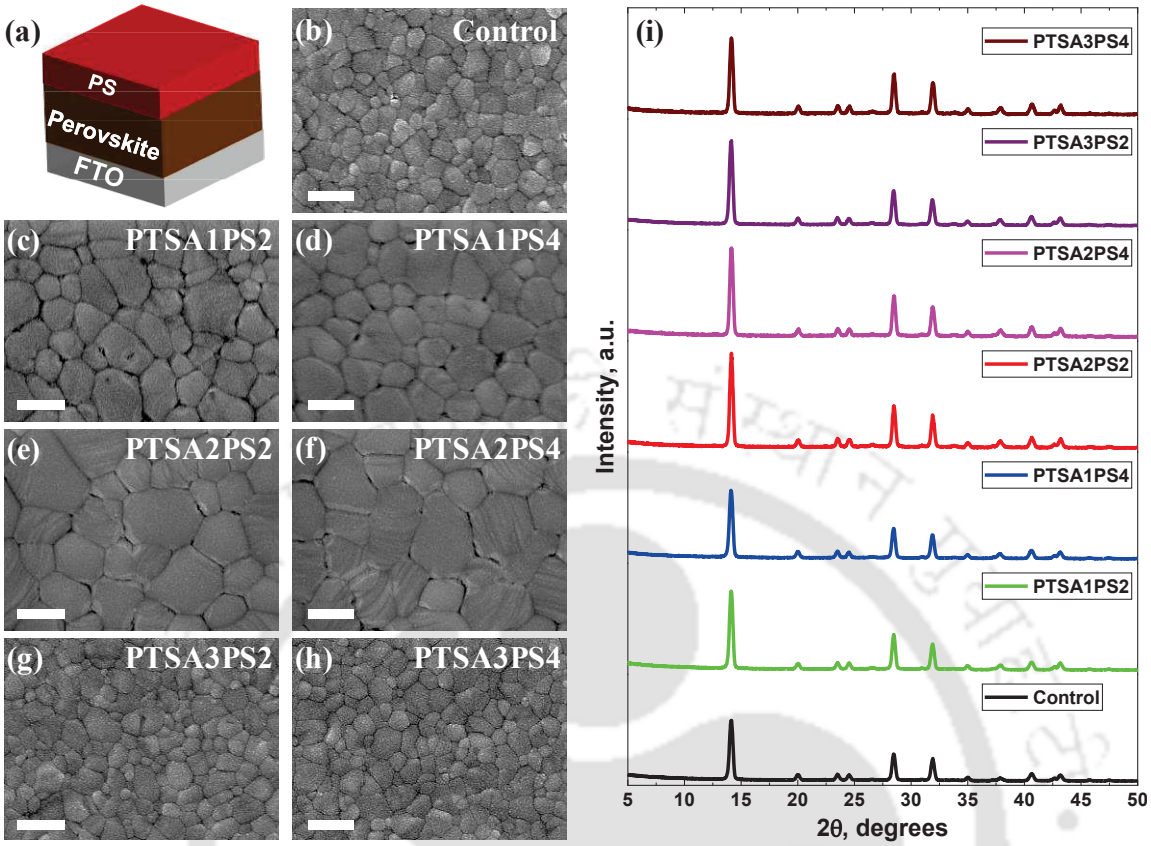

Figure 5.1: (a) Schematic representation of dual-passivation coating, FESEM images (scale bar = 500 nm) of (b) control, (c) PTSA1PS2, (d) PTSA1PS4, (e) PTSA2PS2, (f) PTSA2PS4, (g) PTSA3PS2, (h) PTSA3PS4, and (i) XRD patterns of all perovskite films.

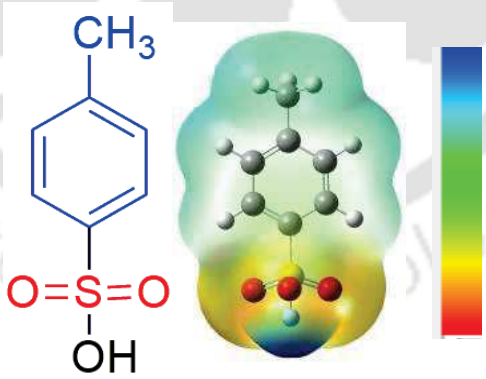

Figure 5.2: Electro-static profile of PTSA.

Electrostatic potential profile (Figure 5.2) confirms that the sulphonyl groups being electronegative can interact with the perovskite and assists in the formation of defect-free crystalline perovskite films. 15 devices of each type having the p-i-n architecture of FTO/NiO_x/Perovskite/PS/PCBM/Rhodamine-101/Ag were fabricated. The control device

was also fabricated without any PTSA additive or PS layer. The variation in each type of device parameters is presented in the box-chart (Figure 5.3). It is clearly evident that the variation in the device results minimized with the dual passivation strategy and was the minimum for PTSA2PS2 device. For any given concentration of PTSA, the PCE is higher for the device with PS concentration 2 mg/mL (PS2) compared to 4 mg/mL (PS4) as all device parameters decreased for higher PS concentration. The reduction in device PCE at higher concentration of PS was most likely due to the slightly thicker insulating nature of the layer which opposes the carrier transport from the perovskite to the electron-transport layer through tunneling.[44]

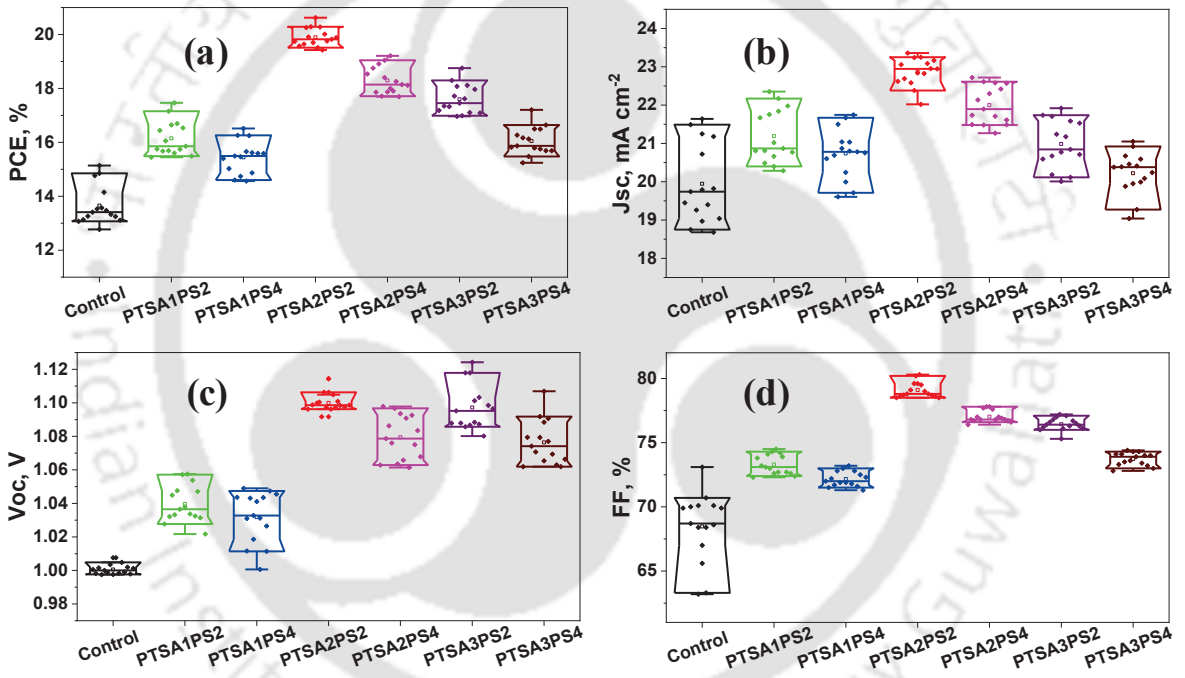

Figure 5.3: Box chart showing variation in (a) PCE, (b) *J*sc, (c) *V*oc, and (d) FF for 15 devices of each type.

The typical *J*-*V* graphs for the best devices of each type are presented in Figure 5.4a and the photovoltaic results with the statistical parameters are given in Table 5.2. The control device without any passivation resulted in a maximum PCE of 15.14% (average 13.65%) with *J*sc = 21.25 mA cm^{-2}, *V*oc = 1.008 V and FF = 70.7 %. With the dual passivation of the perovskite layer, the PCE improved significantly to 20.62% (average 19.90%) with *J*sc = 23.25 mA cm^{-2}, *V*oc = 1.114 V and FF = 79.6 %. Only PTSA (PTSA2) and only PS (PS2) devices were also fabricated and highest PCE of 18.51% and 18.31%, respectively were

obtained (Figure 5.4b). Hence, it can be confirmed that both PTSA and PS played significant role in improving PCE beyond 20%.

Table 5.2: Photovoltaic parameters of all types of fabricated using dual-passivation approach.

Device Type	*J*sc, mA cm^{-2}	*V*oc, V	FF, %	PCE (average)[a], %
Control	21.25	1.008	70.7	15.14 (13.65±0.73)
PTSA1PS2	22.17	1.057	74.3	17.47 (16.15±0.63)
PTSA1PS4	21.67	1.041	73.2	16.51 (15.44±0.60)
PTSA2PS2	23.25	1.114	79.6	20.62 (19.90±0.34)
PTSA2PS4	22.58	1.094	77.8	19.21 (18.29±0.49)
PTSA3PS2	21.92	1.124	76.1	18.75 (17.60±0.54)
PTSA3PS4	20.92	1.107	74.3	17.21 (16.05±0.51)
PTSA2	23.39	1.071	73.9	18.51 (17.36±0.69)
PS2	22.88	1.053	76.0	18.31 (17.11±0.68)

[a]Average and standard deviation of 15 devices.

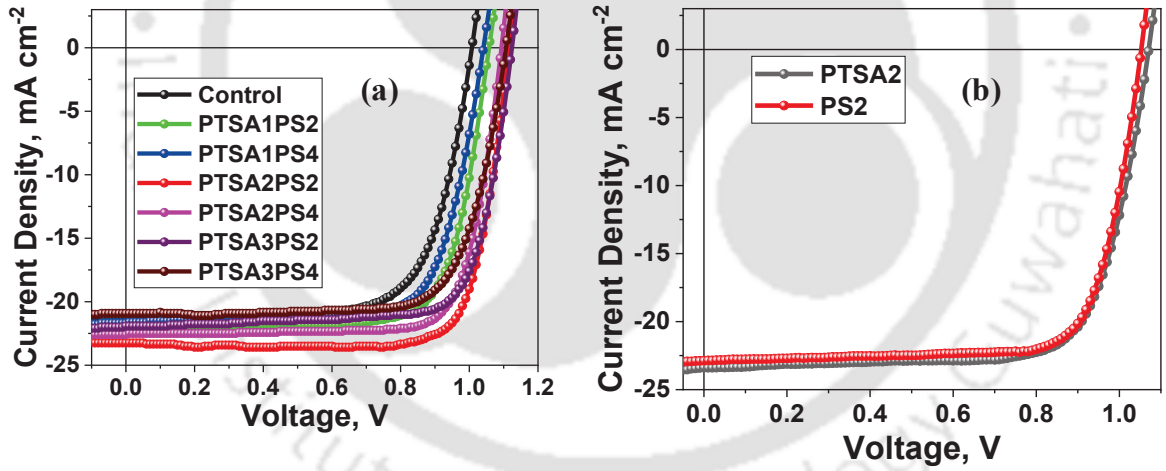

Figure 5.4: *J–V* curves of the (a) dual-passivated & control devices, and (b) only PTSA and only PS passivated devices.

This improvement in the *J*sc for the dual-passivated device can be ascribed to the increase in grain size of the modified perovskite layer which resulted in enhanced absorption compared to the control film (Figure 5.5a). The photon harvesting of the PTSA2PS2 perovskite was improved which resulted in higher charge generation in the photo-active layer. Again, the Tauc plot (Figure 5.5b) confirmed that the bandgap of the perovskite film

was barely altered which further confirmed that the *V*oc loss of the dual passivated PSC device was minimized.

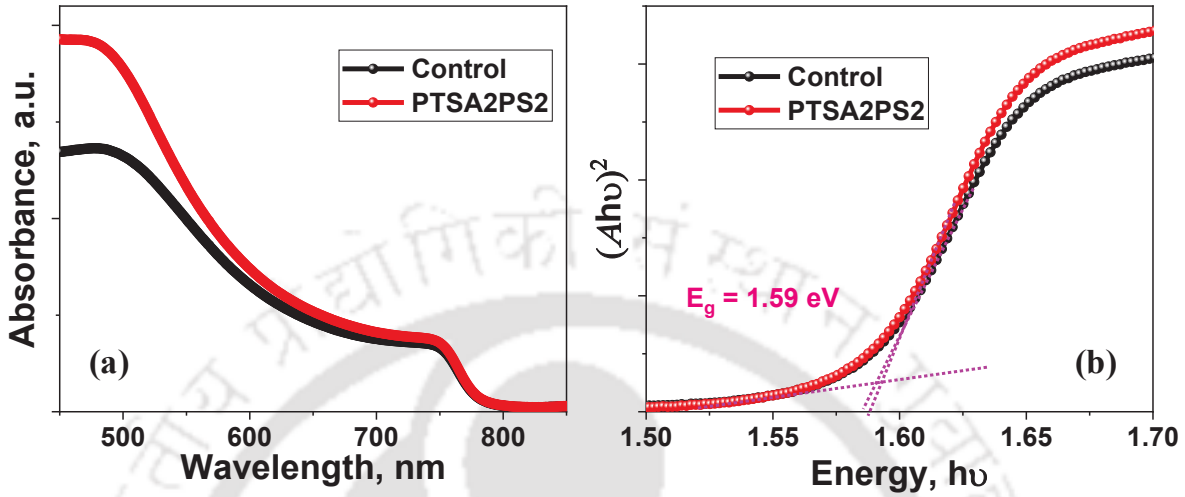

Figure 5.5: (a) UV-vis absorbance, and (b) Tauc plot.

Since the defects were passivated in the perovskite layer due to the dual passivation strategy, the ion-migration reduced and the hysteresis in the *J-V* forward and reverse scans narrowed for the PTSA2PS2 device as compared to the control device (Figure 5.6a). The hysteresis index (HI) (difference between the forward and reverse scan PCEs) calculated for the control and modified devices were 13.4% and 3.6%, respectively. The external quantum efficiency (EQE) of both the control and PTSA2PS2 devices was broad in nature (Figure 5.6b). However, the EQE of PTSA2PS2 solar cell device was higher in magnitude compared to the control throughout the spectrum and was similar to the UV-vis spectrum. The integrated *J*sc was also computed from the EQE spectra of both the control and PTSA2PS2 devices and the results were well-matched with the measured *J*sc values obtained from the *J-V* graphs. Steady state analysis (Figure 5.6c) was performed on the solar cell devices to confirm its stability under light. It can be seen that both the control and PTSA2PS2 devices were almost stable under light for 500 seconds. The steady-state PCE obtained from the control was >14.5%, whereas the same for PTSA2PS2 was >20%. PTSA2PS2-based large area devices (~2.5 cm^2) were also fabricated and their utility confirmed for commercial applications (Figure 5.6d). A very high PCE of ~18.5% was obtained for this large area device, confirming the influence of dual passivation for practical utility.

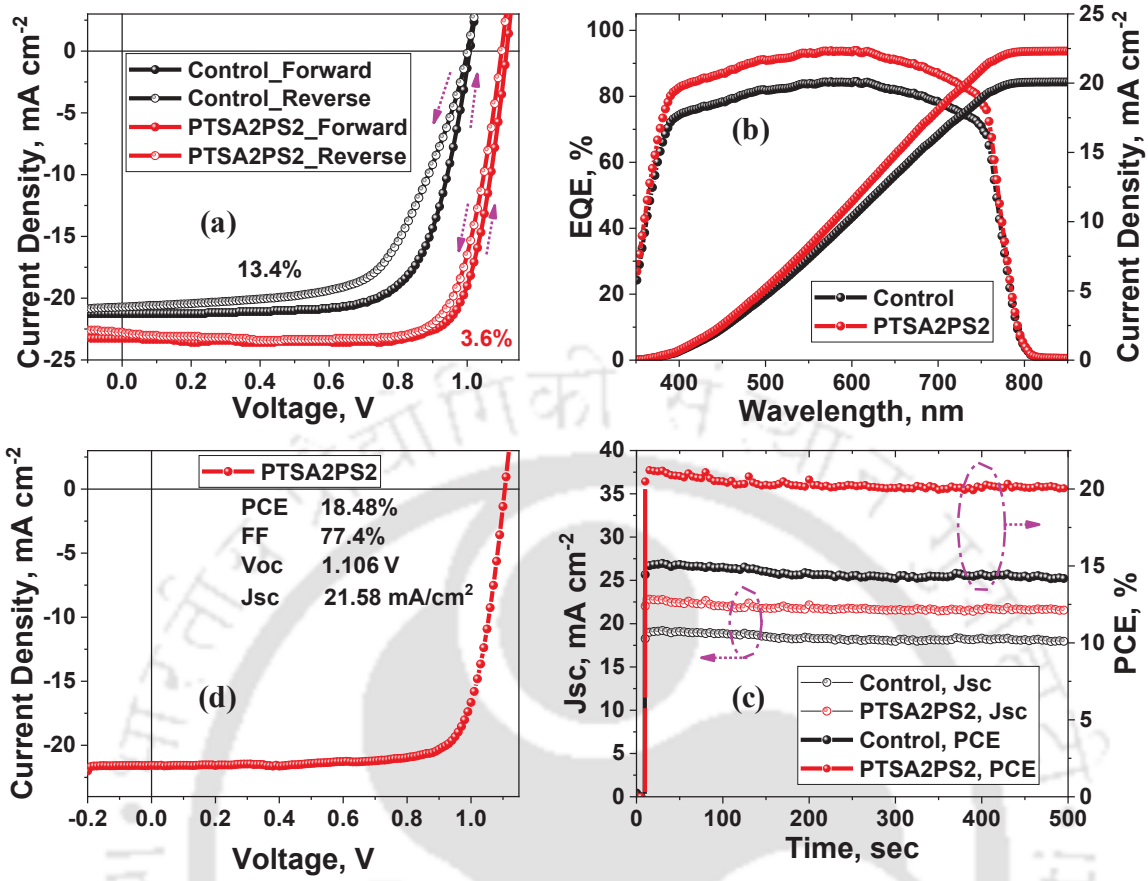

Figure 5.6: (a) Hysteresis study of control and PTSA2PS2 device, (b) EQE and integrated *J*sc spectra of control and PTSA2PS2, (c) Steady state analysis of control and PTSA2PS2, and (d) *J-V* of large-area PTSA2PS2 device.

Impedance spectroscopy (Figure 5.7a) was performed to study the charge recombination dynamics of the photovoltaic devices. The larger semi-circle of the PTSA2PS2 device confirms that the resistance of recombination (R_{rec}) was larger in this case as compared to the control. On fitting this data to the equivalent circuit present in the inset, the R_{rec} was found to be ~48 KΩ and ~8 KΩ for PTSA2PS2 and control devices, respectively. The higher value of R_{rec} for PTSA2PS2 confirms that the current due to the recombination of charges reduced and hence, loss of the photo-generated carriers was minimized as a result of the dual passivation strategy. Lower recombination in the device having dual-passivation would have resulted in higher *V*oc than control.[46] Thereafter, Mott-Schottky (MS) analysis confirmed that the built-in potential of the dual passivated device was higher than the control (Figure 5.7b). This can also be a probable reason for improved *V*oc of the modified device.[47] The residual charge density calculated from the slope of the

MS plots was found to be 3.55 x 10^{16} and 1.84 x 10^{16} cm^{-3} for control and dual-passivated device, respectively. This confirms smooth charge transfer process from the perovskite layer to the electrodes through the transport layers for the dual-passivated devices.

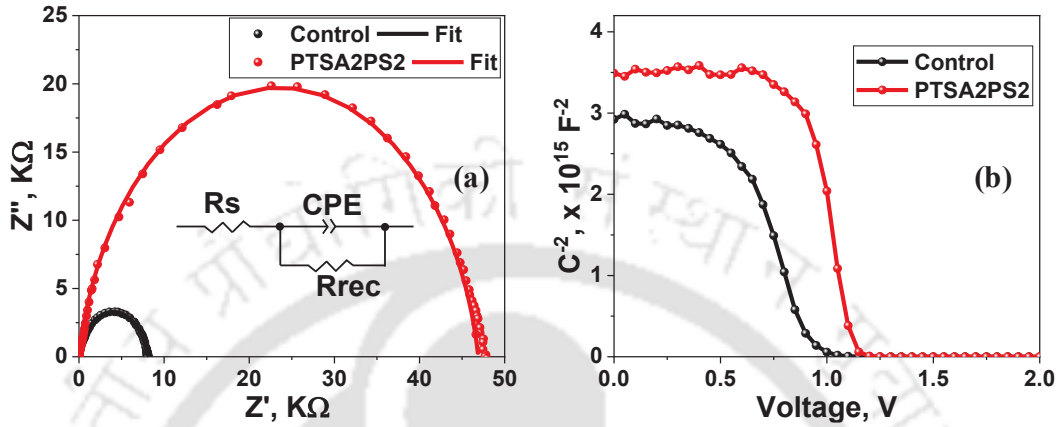

Figure 5.7: a) Impedance Spectroscopy, and (b) Mott-Schottky analysis.

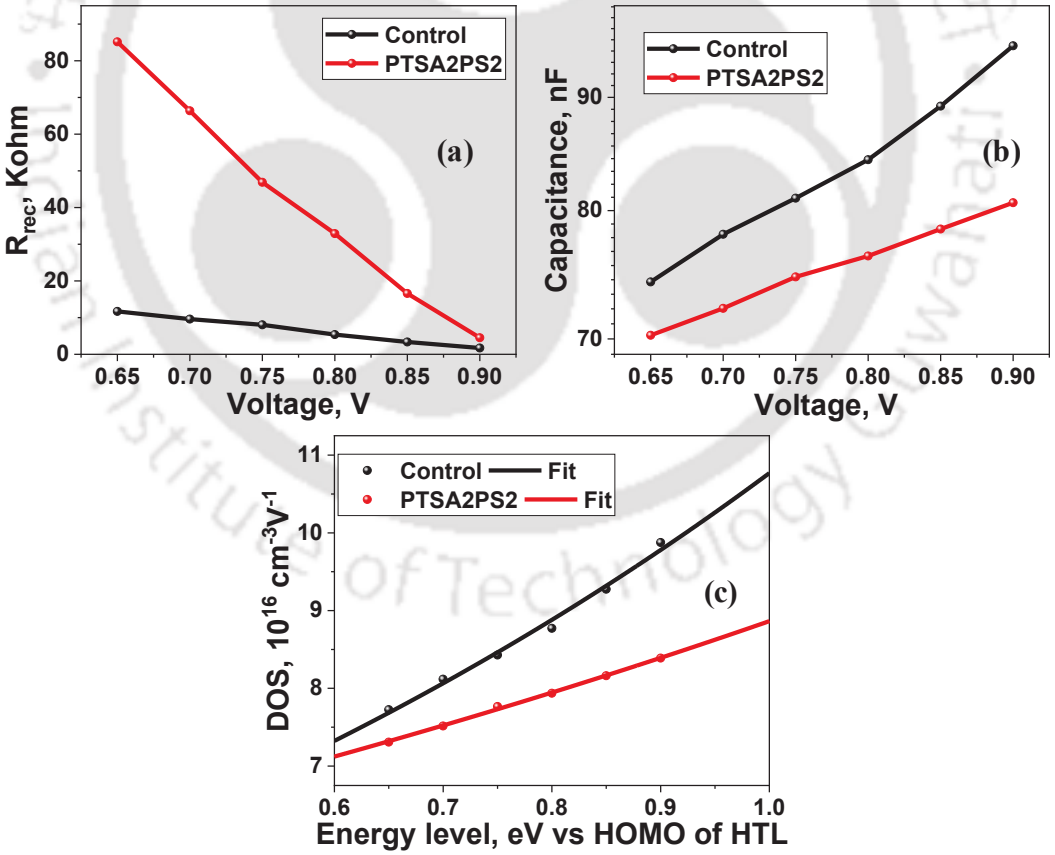

Figure 5.8: (a) Recombination resistance versus voltage plot (b) Capacitance versus voltage plot, and (c) Trap DOS versus energy level plot.

Impedance spectra was also recorded for varying voltages and the R_{rec} and capacitance values were obtained from fitting the equivalent circuit for each voltage. R_{rec} was higher for all voltages for the modified device confirming that the loss due to charge recombination was restrained for them (Figure 5.8a). The capacitance, arising from the accumulated charges in the device, was lower for the dual-passivated device, which assures that the photo-generated charges are transported conveniently resulting in enhanced *J*sc values (Figure 5.8b). The density of states (DOS) due to the trap-states was calculated from exponentially fitting the capacitance data obtained at various voltages (Figure 5.8c). Expectedly, DOS for the modified device was lower and its distribution was narrower compared to control.[35, 48] This ensured lower recombination and better charge transport in the PTSA2PS2 resulting in improved *V*oc and *J*sc, hence higher PCE than the device without any modification.

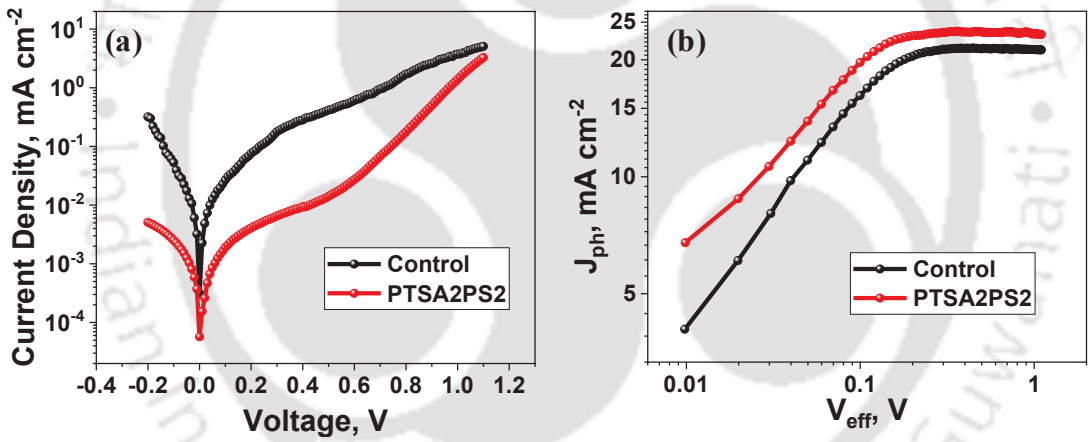

Figure 5.9: (a) Dark *J*-*V* plots of the solar cell devices, and (b) J_{ph} versus V_{eff} plot.

For more detailed trap-related studies, first the dark *J*-*V* curves for control and PTSA2PS2 were recorded and analyzed (Figure 5.9a). The dual-passivated device displayed lower reverse saturation current than control confirming lower leakage current in the device. Thereafter, photo-current (J_{ph}) versus effective voltage (V_{eff}) plot was studied by taking the difference of *J*-*V* curves under light and dark (Figure 5.9b). For PTSA2PS2, the value of J_{ph} was more for all V_{eff} which concludes that the generation rate of the charges was higher which contributed to the current. This was due to the smooth quality perovskite film with

reduced trap-states formed as a result of dual-passivation which accounted for enhanced photon harvesting.

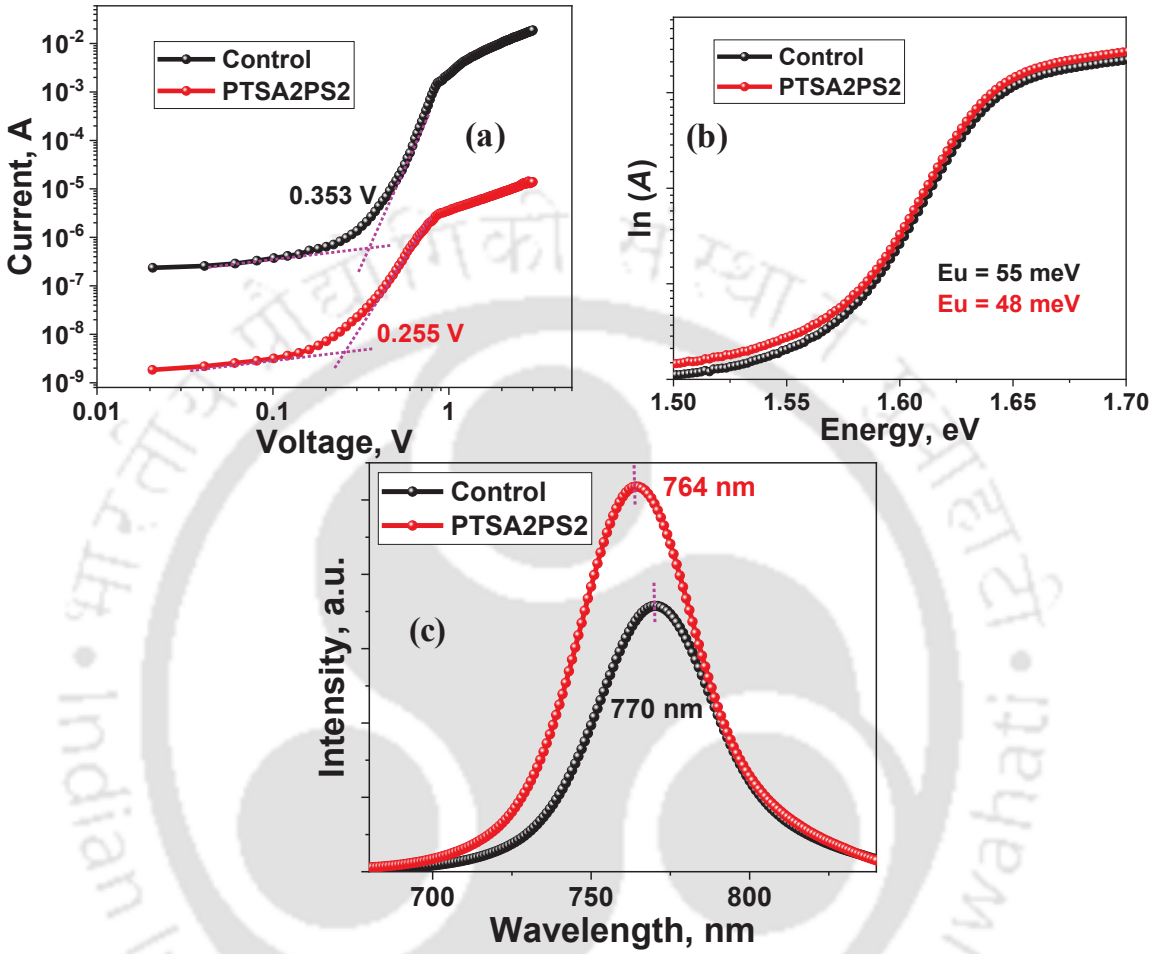

Figure 5.10: (a) Dark *J-V* curve of hole-only device, (b) ln(*A*) versus energy plot to estimate Urbach energy, and (c) PL spectra of the perovskite films.

The trap-density was calculated by fabricating a hole-only device of the architecture FTO/NiO_x/Perovskite/MoO_3/Cu and recording the V_{TFL} value from the dark *J-V* graphs (Figure 5.10a). V_{TFL} is directly proportional to the trap-density and found to be lower for PTSA2PS2 (3.95×10^{15} cm^{-3}) than control (5.47×10^{15} cm^{-3}).[49] Urbach energy (E_u) was calculated from the inverse slope of ln(absorption coefficient, *A*) versus photon energy plot (obtained from the UV-vis results) for both the perovskite films to quantify the defects at the tail-states of the absorbance onset (Figure 5.10b). E_u was calculated to be ~55 meV for the control film, whereas it reduced to ~48 meV for PTSA2PS2 which validated that the defects

in the modified perovskite was effectively passivated. The lower non-radiative recombination for reduction of defects was confirmed by enhanced intensity of the steady state photoluminescence study (Figure 5.10c). The blue-shifted dual-passivated film was observed at 764 nm from 770 nm of the control film which verified trap-passivation of the perovskite. This confirms that the deep trap in the perovskites have reduced which minimizes the trap-density that resulted in higher device performance.[50, 51]

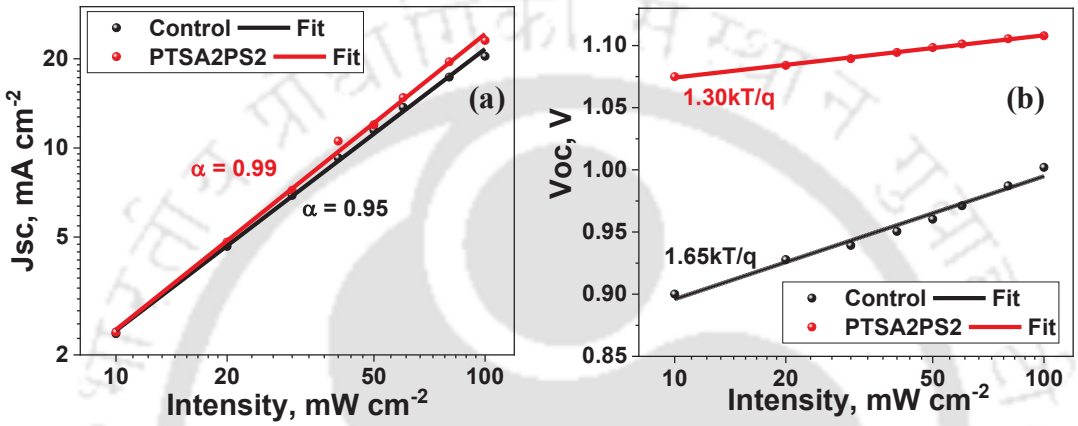

Figure 5.11: (a) *J*sc variation with light intensity, and (b) *V*oc variation with light intensity.

Furthermore, light dependence on *J*sc and *V*oc were studied to understand more about the nature of recombination due to the deep trap states (Figure 5.11a, b). From the slope of the log-log plot of light intensity versus *J*sc, the value of α was estimated. Bimolecular or non-radiative recombination in the device is said to be zero, if the value of α is 1 and a typical solar cell device has α ~1 for minimum photo-generated charge loss. PTSA2PS2 device displayed an α value of 0.99 compared to 0.95 for the control which signifies that non-radiative recombination is minimized as a result of dual-passivation due to the reduction in the defect sites of the perovskite. Ideality factor (n) was projected from the semi-log plot of light intensity versus *V*oc. Generally, the value of n lies in between 1 and 2 for a typical device. If the value of n is closer to 1, then the recombination is lower while the recombination increases due to presence of deep trap sites once the value of n moves closer to 2. The value of n for the control and PTSA2PS2 device was found to be 1.30 and 1.65, respectively. Thus, it can be concluded that the dual-passivation strategy resulted in lower deep trap sites in the perovskite which in turn reduces the recombination losses in the solar cell device.[52, 53]

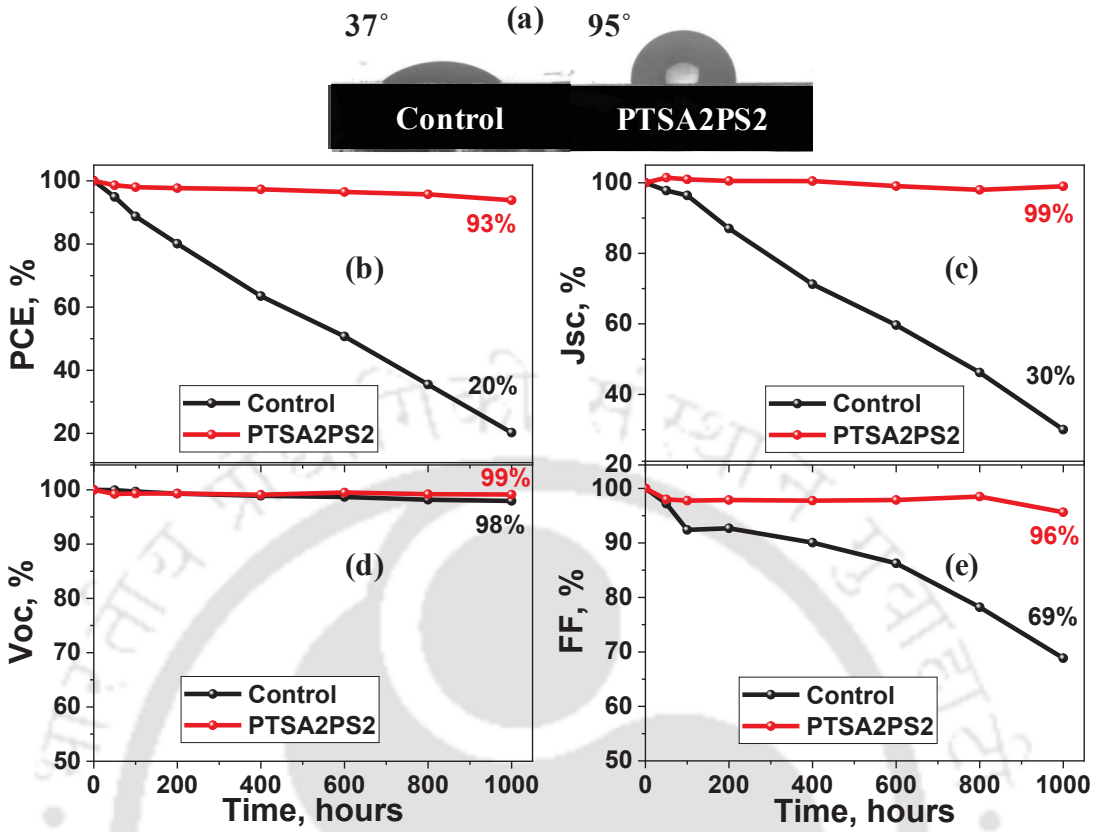

Figure 5.12: (a) Contact angle measurement, Normalized device parameters variation when put through ambient stability (b) PCE, (c) *J*sc, (d) *V*oc, and (e) FF.

Finally, both perovskite films and solar cell devices were put through ambient stability test at room temperature and relative humidity of 50±5%. Expectedly, the hydrophobicity increased tremendously for the dual-passivated film with respect to the control as observed from the contact angle measurement (Figure 5.12a). The dual-passivated device outperformed the ambient stability test and was found to retain 93% of its initial PCE after 1000 hours of study (Figure 5.12b). However, the control device could only manage to maintain 20% of its preliminary PCE at the end of 1000 hours. The other parameters were also plotted to check the main contributor of the device degradation process (Figure 5.12c-e). It was observed that there was not much of decay in the *V*oc of either device at ambient conditions, however, both *J*sc and FF reduced rapidly. Anti-oxidant sulphonic acid group of PTSA and hydrophobic PS helps to delay the degradation process of the devices when kept in ambient.[39, 44] Also, films with pin-holes and smaller grain size are known to degrade faster compared to the one showing larger grain size and fewer pin-holes.[54] To know more about

the degradation process, XRD analysis was performed for the control and dual-passivated films after 1000 hours and compared to the freshly prepared films (Figure 5.13). It was observed that a large PbI_2 peak at 12.6º appears for the control film after 1000 hours, which was missing from the dual-passivated film. Both PTSA and PS assisted in increasing the hydrophobicity of the perovskite and facilitated in maintaining the ambient stability of the modified device.

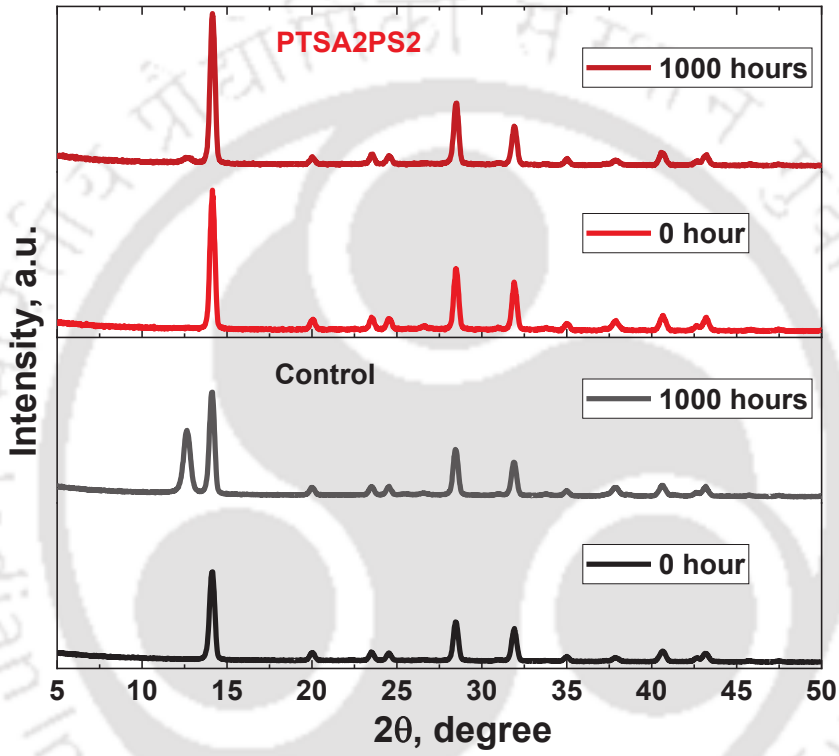

Figure 5.13: XRD patterns of the perovskite films to check ambient stability.

5.4 Conclusion

In summary, a novel dual-passivation approach using PTSA and PS polymer has been developed to simultaneously increase the hydrophobicity, crystallinity, sustainability and long-term stability of the perovskite film. Morphology studies suggested that the grain size of the dual-passivated film increased and also displayed fewer pin-holes. Photovoltaic devices fabricated using the dual-passivation strategy showed highly repeatable PCE and the overall parameters displayed minimum variation. The champion PCE of 20.62% was recorded for the PTSA2PS2 device which has improved significantly from the control device bearing

15.14% efficiency. The modified device showed reduced hysteresis, and a steady state PCE of >20% was also recorded under illumination. Dual-passivated large-area photovoltaic device (~2.5 cm^2) also displayed highest PCE ~18.5%. The dual-passivation resulted in reduced recombination, improved charge transport and lower trap density compared to the control. Due to the increased hydrophobicity the ambient stability of the solar cell device also improved as a result of dual-passivation approach. Overall, this procedure demonstrates that even the smallest incremental changes within a layer and above, turn economical molecules into choicest materials for sustainable devices that not only increase the stability remarkably, but also crosses the PCE barrier for large-area devices. This dual-passivation approach leading to stable and efficient perovskite could help for future commercialization of this solar cell technology.

References

1. J. J. Yoo, G. Seo, M. R. Chua, T. G. Park, Y. Lu, F. Rotermund, Y.-K. Kim, C. S. Moon, N. J. Jeon, J.-P. Correa-Baena, V. Bulović, S. S. Shin, M. G. Bawendi and J. Seo, *Nature*, 2021, **590**, 587-593.
2. L. Gil-Escrig, M. Roß, J. Sutter, A. Al-Ashouri, C. Becker and S. Albrecht, *Solar RRL*, 2021, **5**, 2000553.
3. National Renewable Energy Laboratory, Best research-cell efficiencies chart, https://www.nrel.gov/pv/assets/pdfs/best-research-cell-efficiencies.20200104.pdf, (accessed 16.05.2021, 2021).
4. S. D. Stranks, G. E. Eperon, G. Grancini, C. Menelaou, M. J. P. Alcocer, T. Leijtens, L. M. Herz, A. Petrozza and H. J. Snaith, *Science*, 2013, **342**, 341.
5. A. Kojima, K. Teshima, Y. Shirai and T. Miyasaka, *J. Am. Chem. Soc.*, 2009, **131**, 6050-6051.
6. P. Zhao, B. J. Kim, X. Ren, D. G. Lee, G. J. Bang, J. B. Jeon, W. B. Kim and H. S. Jung, *Adv. Mater.*, 2018, **30**, 1802763.
7. C. Li, J. Yin, R. Chen, X. Lv, X. Feng, Y. Wu and J. Cao, *J. Am. Chem. Soc.*, 2019, **141**, 6345-6351.
8. D.-K. Lee, D.-N. Jeong, T. K. Ahn and N.-G. Park, *ACS Energy Lett.*, 2019, **4**, 2393-2401.
9. H. B. Lee, N. Kumar, M. M. Ovhal, Y. J. Kim, Y. M. Song and J.-W. Kang, *Adv. Funct. Mater.*, 2020, **30**, 2001559.
10. R. K. Gupta, R. Garai, M. Hossain, A. Choudhury and P. K. Iyer, *ACS Sustainable Chemistry & Engineering*, 2021, **9**, 7993-8001.
11. M. A. Afroz, R. K. Gupta, R. Garai, M. Hossain, S. P. Tripathi and P. K. Iyer, *Org. Electron.*, 2019, **74**, 172-178.
12. W. Yang, R. Su, D. Luo, Q. Hu, F. Zhang, Z. Xu, Z. Wang, J. Tang, Z. Lv, X. Yang, Y. Tu, W. Zhang, H. Zhong, Q. Gong, T. P. Russell and R. Zhu, *Nano Energy*, 2020, **67**, 104189.
13. H. Wang, J. Song, Z. Li, L. Li, J. Li, X. Li, J. Qu and W.-Y. Wong, *J. Mater. Chem. A*, 2020, **8**, 11728-11733.
14. T. Liu, Y. Jiang, M. Qin, J. Liu, L. Sun, F. Qin, L. Hu, S. Xiong, X. Jiang, F. Jiang, P. Peng, S. Jin, X. Lu and Y. Zhou, *Nat. Commun.*, 2019, **10**, 878.
15. T. Bu, J. Li, W. Huang, W. Mao, F. Zheng, P. Bi, X. Hao, J. Zhong, Y.-B. Cheng and F. Huang, *J. Mater. Chem. A*, 2019, **7**, 6793-6800.
16. H. Ren, S. Yu, L. Chao, Y. Xia, Y. Sun, S. Zuo, F. Li, T. Niu, Y. Yang, H. Ju, B. Li, H. Du, X. Gao, J. Zhang, J. Wang, L. Zhang, Y. Chen and W. Huang, *Nat. Photonics*, 2020, **14**, 154-163.
17. G. Wang, W. Dong, A. Gurung, K. Chen, F. Wu, Q. He, R. Pathak and Q. Qiao, *J. Power Sources*, 2019, **432**, 48-54.
18. S. Wu, J. Zhang, Z. Li, D. Liu, M. Qin, S. H. Cheung, X. Lu, D. Lei, S. K. So, Z. Zhu and A. K. Y. Jen, *Joule*, 2020, **4**, 1248-1262.
19. S.-W. Lee, S. Kim, S. Bae, K. Cho, T. Chung, J.-K. Hwang, I. Song, W. Lee, S. Park, J. Jung, J. Chun, Y. J. Lee, Y. J. Moon, H.-S. Lee, D. Kim, C. B. Mo and Y. Kang, *Org. Electron.*, 2018, **63**, 343-348.

20. S. Jin, Y. Wei, F. Huang, X. Yang, D. Luo, Y. Fang, Y. Zhao, Q. Guo, Y. Huang and J. Wu, *J. Power Sources*, 2018, **404**, 64-72.
21. C. Dong, X. Han, Y. Zhao, J. Li, L. Chang and W. Zhao, *Solar RRL*, 2018, **2**, 1800139.
22. S. Paek, P. Schouwink, E. N. Athanasopoulou, K. T. Cho, G. Grancini, Y. Lee, Y. Zhang, F. Stellacci, M. K. Nazeeruddin and P. Gao, *Chem. Mater.*, 2017, **29**, 3490-3498.
23. M. Zhang, Z. Wang, B. Zhou, X. Jia, Q. Ma, N. Yuan, X. Zheng, J. Ding and W.-H. Zhang, *Solar RRL*, 2018, **2**, 1700213.
24. A. D. Taylor, Q. Sun, K. P. Goetz, Q. An, T. Schramm, Y. Hofstetter, M. Litterst, F. Paulus and Y. Vaynzof, *Nat. Commun.*, 2021, **12**, 1878.
25. K. M. Reza, A. Gurung, B. Bahrami, A. H. Chowdhury, N. Ghimire, R. Pathak, S. I. Rahman, M. A. R. Laskar, K. Chen, R. S. Bobba, B. S. Lamsal, L. K. Biswas, Y. Zhou, B. Logue and Q. Qiao, *Solar RRL*, 2021, **5**, 2000740.
26. M. A. R. Laskar, W. Luo, N. Ghimire, A. H. Chowdhury, B. Bahrami, A. Gurung, K. M. Reza, R. Pathak, R. S. Bobba, B. S. Lamsal, K. Chen, M. T. Rahman, S. I. Rahman, K. Emshadi, T. Xu, M. Liang, W.-H. Zhang and Q. Qiao, *Adv. Funct. Mater.*, 2020, **30**, 2000778.
27. Z. Wu, S. R. Raga, E. J. Juarez-Perez, X. Yao, Y. Jiang, L. K. Ono, Z. Ning, H. Tian and Y. Qi, *Adv. Mater.*, 2018, **30**, 1703670.
28. H. Zheng, L. Zhu, L. Hu, S. Yang, S. Chen, A. Alsaedi, T. Hayat, Y. Huang, X. Pan and S. Dai, *J. Mater. Chem. A*, 2018, **6**, 9930-9937.
29. T. Wu, Y. Wang, X. Li, Y. Wu, X. Meng, D. Cui, X. Yang and L. Han, *Adv. Energy Mater.*, 2019, **9**, 1803766.
30. Q. Jiang, Y. Zhao, X. Zhang, X. Yang, Y. Chen, Z. Chu, Q. Ye, X. Li, Z. Yin and J. You, *Nat. Photonics*, 2019, **13**, 460-466.
31. X. Jiang, S. Chen, Y. Li, L. Zhang, N. Shen, G. Zhang, J. Du, N. Fu and B. Xu, *ACS Appl. Mater. Interfaces*, 2021, **13**, 2558-2565.
32. F. Bella, G. Griffini, J.-P. Correa-Baena, G. Saracco, M. Grätzel, A. Hagfeldt, S. Turri and C. Gerbaldi, *Science*, 2016, **354**, 203.
33. E. H. Jung, N. J. Jeon, E. Y. Park, C. S. Moon, T. J. Shin, T.-Y. Yang, J. H. Noh and J. Seo, *Nature*, 2019, **567**, 511-515.
34. M. Hossain, R. Garai, R. K. Gupta, R. N. Arunagirinathan and P. K. Iyer, *J. Mater. Chem. C*, 2021, DOI: 10.1039/D1TC02335G.
35. R. Garai, M. A. Afroz, R. K. Gupta and P. K. Iyer, *Adv. Sustainable Syst.*, 2020, **4**, 2000078.
36. M. Adil Afroz, N. Ghimire, K. M. Reza, B. Bahrami, R. S. Bobba, A. Gurung, A. H. Chowdhury, P. K. Iyer and Q. Qiao, *ACS Appl. Energy Mater.*, 2020, **3**, 2432-2439.
37. E. Akman, A. E. Shalan, F. Sadegh and S. Akin, *ChemSusChem*, 2021, **14**, 1176-1183.
38. X. Li, M. Ibrahim Dar, C. Yi, J. Luo, M. Tschumi, S. M. Zakeeruddin, M. K. Nazeeruddin, H. Han and M. Grätzel, *Nat. Chem.*, 2015, **7**, 703-711.
39. Q. Tai, X. Guo, G. Tang, P. You, T.-W. Ng, D. Shen, J. Cao, C.-K. Liu, N. Wang, Y. Zhu, C.-S. Lee and F. Yan, *Angew. Chem., Int. Ed.*, 2019, **58**, 806-810.
40. R. Garai, R. K. Gupta, A. S. Tanwar, M. Hossain and P. K. Iyer, *Chem. Mater.*, 2021, **33**, 5709-5717.

41. I. Hwang, I. Jeong, J. Lee, M. J. Ko and K. Yong, *ACS Appl. Mater. Interfaces*, 2015, **7**, 17330-17336.
42. X.-X. Gao, D.-J. Xue, D. Gao, Q. Han, Q.-Q. Ge, J.-Y. Ma, J. Ding, W. Zhang, B. Zhang, Y. Feng, G. Yu and J.-S. Hu, *Solar RRL*, 2019, **3**, 1800232.
43. H. Zhang, J. Shi, L. Zhu, Y. Luo, D. Li, H. Wu and Q. Meng, *Nano Energy*, 2018, **43**, 383-392.
44. M. Li, X. Yan, Z. Kang, Y. Huan, Y. Li, R. Zhang and Y. Zhang, *ACS Appl. Mater. Interfaces*, 2018, **10**, 18787-18795.
45. J. Peng, J. I. Khan, W. Liu, E. Ugur, T. Duong, Y. Wu, H. Shen, K. Wang, H. Dang, E. Aydin, X. Yang, Y. Wan, K. J. Weber, K. R. Catchpole, F. Laquai, S. De Wolf and T. P. White, *Adv. Energy Mater.*, 2018, **8**, 1801208.
46. X. Cao, C. Li, Y. Li, F. Fang, X. Cui, Y. Yao and J. Wei, *Nanoscale*, 2016, **8**, 19804-19810.
47. J. Yang, S. Xiong, J. Song, H. Wu, Y. Zeng, L. Lu, K. Shen, T. Hao, Z. Ma, F. Liu, C. Duan, M. Fahlman and Q. Bao, *Adv. Energy Mater.*, 2020, **10**, 2000687.
48. A. Choudhury, R. K. Gupta, R. Garai and P. K. Iyer, *Adv. Mater. Interfaces*, 2021, DOI: https://doi.org/10.1002/admi.202100574, 2100574.
49. G. Liu, H. Zheng, H. Xu, L. Zhang, X. Xu, S. Xu and X. Pan, *Nano Energy*, 2020, **73**, 104753.
50. Y. Shao, Z. Xiao, C. Bi, Y. Yuan and J. Huang, *Nat. Commun.*, 2014, **5**, 5784.
51. G. Liu, H. Zheng, L. Zhang, H. Xu, S. Xu, X. Xu, Z. Liang and X. Pan, *Chem. Eng. J.*, 2021, **407**, 127204.
52. R. K. Gupta, R. Garai, M. A. Afroz and P. K. Iyer, *J. Mater. Chem. C*, 2020, **8**, 8191-8198.
53. T. Singh and T. Miyasaka, *Adv. Energy Mater.*, 2018, **8**, 1700677.
54. C.-H. Chiang and C.-G. Wu, *ChemSusChem*, 2016, **9**, 2666-2672.

Chapter 6

Summary and Prospects

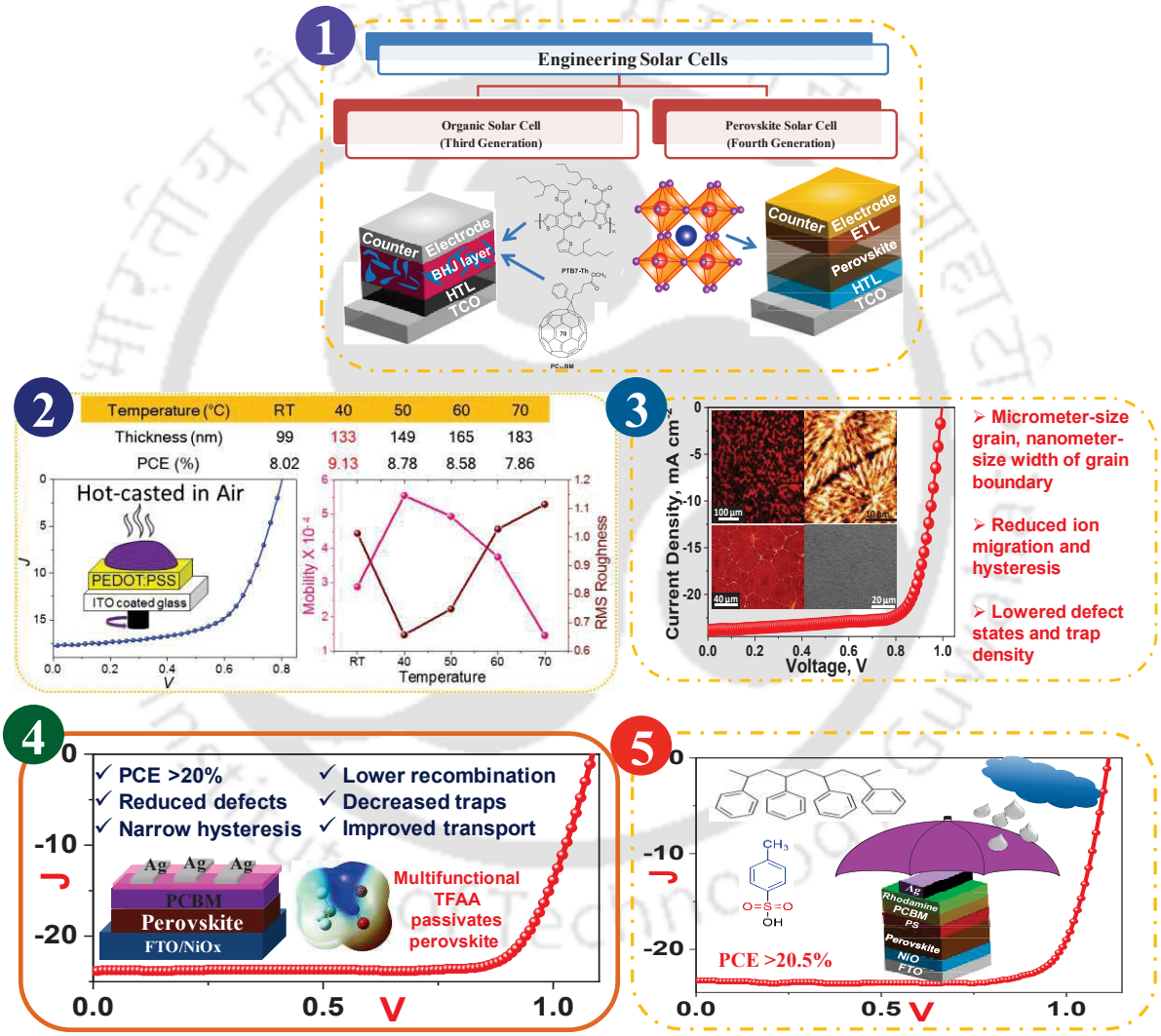

[This page was intentionally left blank]

6.1 Summary

The growing demand for clean energy sources due to the ever increasing pollution from the fossil fuels have prioritized to growth of solar energy exploration. Both organic solar cells (OSCs) and perovskite solar cells (PSCs) have shown promising growth in terms of efficiency and stability to challenge the other photovoltaic technologies towards commercialization. This thesis is focused on engineering the active layer of OSC and PSC towards improving the solar cell device performance. Initially, hot-casting technique has been used in modulating the morphology of the active layer in the OSC and PSC. Finally, bulk and surface passivation of perovskite using additive engineering was carried out to reduce the defects in the perovskite and improve the solar cell device performance.

The first chapter of this thesis discussed the need for energy, a brief history of the development of solar cell, the solar cell device parameters and techniques used to define solar cell performance, generations of solar cells, working principle and device architecture of OSC and PSC has been presented. The chapter also covers various device engineering techniques that have been used across the globe in the development of high-performance OSCs and PSCs.

In the second chapter, the role of hot-casting technique in modulating the thickness and morphology of the active layer for OSC fabrication has been studied. A detailed study of absorption, crystallinity, morphology and solar cell performance has been carried out. Active layer mobility and photovoltaic parameters loss due to presence of traps have been also covered. It has been proved that the hot-casting technique can be employed to develop thick active layer OSCs without comprising on the device performance.

Chapter three demonstrated crystallization and grain growth regulation through the addition of methyl ammonium lead bromide (MABr) in mixed-halide perovskite precursor solution for application in hot-casted PSC. The addition of MABr reduced the halide defects and mitigated ion migration. Micrometer-sized grains and millimeter-sized grain boundary was formed reducing the recombination centers in perovskite.

Chapter four described the use of trifluoro acetic acid (TFAA) with both fluoro and carboxylic acid group for crystallization control of perovskite films. TFAA modulated the

crystallization process to enable enlargement of grains and minimize the grain boundaries. The detailed study on how TFAA controls the perovskite formation along with device performance and stability has been presented.

Finally, chapter five elucidated the dual-passivation of perovskite in the bulk and at the surface using p-toluenesulphonic acid (PTSA) and polystyrene (PS), respectively to enhance the efficiency and ambient stability of the solar cell device. This strategy of dual-passivation shows the effectiveness of this technique in achieving good morphology perovskite films with reduced trap states and ion migration.

6.2 Prospects

Extensive studies on molecular engineering of donor and acceptor materials have been carried out to solve many issues en route high efficiency OSC. Also, various other device engineering including varying the donor-acceptor ratio, thermal annealing and solvent vapor treatment of active layer has been attempted to further minimize the losses and improve the device performance. The hot-casting technique developed in this thesis for OSC can be further combined with other device engineering to further understand the modulation of active layer property for solar cell application. This technique can also be utilized with other donor and acceptor systems (both fullerene and non-fullerene) to further enhance the efficiency and develop thick OSCs.

The last decade is considered as the growth of PSC in the field of photovoltaic technology. The power conversion efficiency (PCE) has reached beyond 25% and is challenging its inorganic counterpart which has already seen the success of commercialization. But, there are a few unanswered questions that are hindering its way towards commercialization. Thus, for further growth the following strategies and challenges could be considered.

The PCE of a PSC can be further improved by understanding the recombination mechanism in the bulk and at the interfaces of the perovskite. Thereafter, the recombination can be minimized by passivation of the traps. The composition of the perovskite can also be varied to double/triple cations in structural evolution of perovskite crystal. Additionally, the

hot-casting technique can also be employed to develop large grain perovskite films using various compositional engineering.

Other than the PCE, stability of the PSCs is another important criterion to strengthen the purpose of commercialization for this photovoltaic technology. A perovskite with ideal cubic structure is required for better structural and operational stability. The tolerance factor of the perovskite crystal should be closer to unity to facilitate high stability. The solution processed perovskite fabrication results in many defects and strains in the film. Fabrication of perovskite films with minimum crystal strain and desired orientation along with more air-stable facets is anticipated. This is expected to raise the intrinsic stability of perovskite films and also of the solar cell devices significantly. Further, the poor stability against humidity is being controlled by the use of large size cation to form 2D or 2D/3D mixed perovskites. More insights are required to understand the interaction of these large cations in perovskite crystal to increase the stability. This will allow simultaneous enhancement of PCE and operation stability of the solar cell devices. Finally, investigation and development of other materials used in the fabrication of perovskites (including the transport layers) and for sealing/encapsulation should establish a significant step towards overall long-term stability.

Toxicity of lead poses a potential threat to commercialization of lead-based perovskite photovoltaics. Although, tin-based perovskites have shown the possibility to be used in solar cells, their stability is far behind the lead-based perovskites. Some additives (SnF_2, $SnCl_2$, etc) are being used to enhance the stability of tin-based perovskites, but the result is not promising enough to be considered for commercial application. Further exploration to understand tin-based perovskites might lead to improvement in the performance and stability of these Pb-free PSCs.

For commercialization, both OSC and PSC need to be demonstrated on large-area devices and modules. Therefore, the device engineering developed through this thesis can be merged with the printing techniques such as doctor-blading or inkjet printing or spray coating to develop large-area solar cell devices/modules. This will help in understanding the problems that occurs in fabrication of solar modules for commercial usage.

In summary, the work presented in this thesis demonstrates the strategy to develop thick film OSC. It also shows the approaches to prepare high quality perovskite films with large grains, less grain boundaries, and minimized trap states. These strategies were designed with the aim to improve the performances as well as stability of solar cells.

Outcomes

Publications

1. **Ritesh Kant Gupta**, Rabindranath Garai, Parameswar Krishnan Iyer, "Ambient Stable Perovskite Solar Cell through Trifluoro Acetic Acid-mediated Multifunctional Anchoring", *ACS Appl. Energy Mater.*, **2022**, 5, 1571–1579.
2. **Ritesh Kant Gupta**, Rabindranath Garai, Parameswar Krishnan Iyer, "Dual-passivation Strategy for Improved Ambient Stability of Perovskite Solar Cells", *ACS Appl. Energy Mater.*, **2021**, 4, 10025-10032.
3. **Ritesh Kant Gupta**, Rabindranath Garai, Maimur Hossain, Anwesha Choudhury, Parameswar Krishnan Iyer, "Halide Engineering for Mitigating Ion Migration and Defect-States in Hot-Cast Perovskite Solar Cells", *ACS Sustainable Chem. Eng.*, **2021**, 9, 7993-8001.
4. **Ritesh Kant Gupta**, Rabindranath Garai, Maimur Hossain, Mohammad Adil Afroz, Dibashmani Kalita, Parameswar Krishnan Iyer, "Engineering Polymer Solar Cells: Advancement in Active Layer Thickness and Morphology", *J. Mater. Chem. C*., **2021**, 9, 8746-8775.
5. **Ritesh Kant Gupta**, Rabindranath Garai, Mohammad Adil Afroz, Parameswar Krishnan Iyer, "Regulating Active Layer Thickness and Morphology for High Performance Hot-casted Polymer Solar Cells", *J. Mater. Chem. C*, **2020**, 8, 8191-8198.
6. Rabindranath Garai, **Ritesh Kant Gupta**, Anwesha Choudhury, Parameswar Krishnan Iyer, "Triple passivation approach to laminate perovskite layer for augmented UV and ambient stable photovoltaics". (Revised manuscript submitted)
7. Anwesha Choudhury, **Ritesh Kant Gupta**, Rabindranath Garai, Parameswar Krishnan Iyer, "Tuning Polymer Semiconductor Morphology through Additive Engineering for Stable Phototransistor", *ACS Appl. Electron. Mater.*, **2021**, 3, 5393–5401.
8. Rabindranath Garai, **Ritesh Kant Gupta**, Maimur Hossain, Parameswar Krishnan Iyer, "Surface recrystallized stable 2D-3D graded perovskite solar cells for efficiency beyond 21%", *J. Mater. Chem. A*, 9, 26069-26076.
9. Maimur Hossain, Rahul Narasimhan Arunagirinathan, Rabindranath Garai, **Ritesh Kant Gupta**, Parameswar Krishnan Iyer, "Enhancing Efficiency and Ambient Stability of

Perovskite Solar Cells via Multifunctional Trap Passivation Molecule", *J. Mater. Chem. C*, **2021**, 9, 14309-14317.

10. Mohammad Adil Afroz, Rabindranath Garai, **Ritesh Kant Gupta**, Parameswar Krishnan Iyer, "Additive assisted defect passivation for minimization of open circuit voltage loss and improved perovskite solar cell performance" *ACS Appl. Energy Mater.*, **2021**, 4, 10468–10476.
11. Rabindranath Garai, **Ritesh Kant Gupta**, Arvin Sain Tanwar, Maimur Hossain, Parameswar Krishnan Iyer, "Conjugated Poly-electrolyte Passivated Stable Perovskite Solar Cells for Efficiency Beyond 20%", *Chem. Mater.*, **2021**, 33, 5709–5717.
12. Anwesha Choudhury, **Ritesh Kant Gupta**, Rabindranath Garai, Parameswar Krishnan Iyer, "Tailoring trap density of states through Impedance analysis for flexible organic field-effect transistors", *Adv. Mater. Interfaces*, **2021**, 8, 2100574.
13. Maimur Hossain, Rabindranath Garai, **Ritesh Kant Gupta**, Rahul Narasimhan Arunagirinathan, Parameswar Krishnan Iyer, "Fluoroarene Derivative based Passivation of Perovskite Solar Cell Exhibiting Excellent Ambient and Thermo-Stability Achieving Efficiency > 20%", *J. Mater. Chem. C*, **2021**, 9, 10406-10413.
14. Rabindranath Garai, Mohammad Adil Afroz, **Ritesh Kant Gupta**, Parameswar Krishnan Iyer, "Efficient Trap Passivation of $MAPbI_3$ via Multifunctional Anchoring for High-Performance and Stable Perovskite Solar Cells", *Adv. Sustainable Syst.*, **2020**, 4, 2000078.
15. Rabindranath Garai, Mohammad Adil Afroz, **Ritesh Kant Gupta**, Anwesha Choudhury, Parameswar Krishnan Iyer, "High-Performance Ambient-Condition-Processed Polymer Solar Cells and Organic Thin-Film Transistors", *ACS Omega*, **2020**, 5, 2747-2754.
16. Mohammad Adil Afroz, **Ritesh Kant Gupta**, Rabindranath Garai, Maimur Hossain, Suyashpati Tripathi, Parameswar Krishnan Iyer, "Crystallization and grain growth regulation through Lewis acid-base adduct formation in hot cast perovskite-based solar cells", *Org. Electron.*, **2019**, 74, 172-178.
17. Radhakrishna Ratha, Ashish Singh, Mohammad Adil Afroz, **Ritesh Kant Gupta**, Martin Baumgarten, Klaus Müllen, Parameswar Krishnan Iyer, "6,7-Di(thiophen-2-yl)naphtho[2,3-c][1,2,5]thiadiazole and 4,6,7,9-tetra (thiophen-2-yl)naphtho[2,3-c][1,2,5]thiadiazole as new acceptor units for D-A type co-polymer for polymer solar cells", *Synth. Met.,* **2019**, 252, 113-121.

18. Radhakrishna Ratha, Mohammad Adil Afroz, **Ritesh Kant Gupta**, Parameswar Krishnan Iyer, "Substituting non-conjugating ester group on benzothiadiazole side chain in donor-acceptor polymer improves the solar cell performance", *New J. of Chem.*, **2019**, 43, 4242-4252.
19. Rahul Kumar, Rakesh K Meena, **Ritesh Kant Gupta**, Parameswar Krishnan Iyer, M Arun Tej, Shabari Nath, "Battery Charging of Smart Phones using Organic Solar Cells", *2nd IEEE International Conference on Power Electronics, Intelligent Control and Energy Systems (ICPEICES)*, **2018,** 1-5.
20. Anwesha Choudhury, Priyanka Dogra, Biki Teron, **Ritesh Kant Gupta,** Anamika Dey, Ashish Singh, Rabindranath Garai, Parameswar Krishnan Iyer, "Morphology Control of Mixed Halide Perovskite for its Application in Low-cost Thin Film Transistor", *2nd IEEE International Conference on Power Electronics, Intelligent Control and Energy Systems (ICPEICES)*, **2018,** 743-747.
21. Ashish Singh, Telugu Bhim Raju, Anamika Dey, **Ritesh Kant Gupta,** Parameswar Krishnan Iyer, "Effect of Dual Cathode Buffer Layer on Ternary Organic Solar Cell", *IEEE 44th Photovoltaic Specialist Conference (PVSC)*, **2017,** 1034-1036.

Book Chapter

1. **Ritesh Kant Gupta**, Rahul Narasimahan Arunagirinathan, Mohammad Adil Afroz, Rabindranath Garai, Anwesha Choudhury, Maimur Hossain, Ramesh Babu Yathirajula, Parameswar Krishnan Iyer, "Functional Materials for Various Organic Electronic Devices", *Chemical Solution Synthesis for Materials Design and Thin Film Device Applications: Soumen Das, Sandip Dhara* (Eds.), **2021**, 119-165, Elsevier, Paperback ISBN: 9780128197189, eBook ISBN: 9780128231708.

Patents Filed

1. Parameswar Krishnan Iyer, **Ritesh Kant Gupta**, Mohammad Adil Afroz, Rabindranath Garai,"A High Efficiency Polymer Solar Cell and a Process for Fabricating the same", 2020, Ref. No. 201931019186, Appl. No. 201931019186 A.
2. Parameswar Krishnan Iyer, Rabindranath Garai, Mohammad Adil Afroz, **Ritesh Kant Gupta**, "PTB7-Th donor polymer based Donor- acceptor (D-A) conducting polymer (CPs) suitable for polymer solar cells (PSC) and devices thereof", 2020, Ref. No. 201931020744, Appl. No. 201931020744 A.

Conferences & Workshops

Conferences

1. Research and Industrial Conclave (**RIC2022**) held at Indian Institute of Technology Guwahati, Assam, India during January 20-23, 2022 (**Best Oral Presentation Award**)
2. 7th International Conference on Advanced Nanomaterials and Nanotechnology (**ICANN2021**) held at Indian Institute of Technology Guwahati, Assam, India during December 14-17, 2021
3. International Conference on Progress and Challenges In Modern Day Science (**PCMDS2021**) organized by B. Barooah College, Guwahati, Assam, India during 17-18 June, 2021
4. International Symposium on Organic Iontronics for Sustainable Future organized by Materials Research Society of Japan (**MRSJ**) during December 9-11, 2020
5. Virtual conference on Materials for Energy Harvesting and Catalysis (**MEHC2020**) jointly organized by Tata Institute of Fundamental Research and Indian Institute of Science Education and Research Kolkata, India during May 1-3, 2020
6. International Conference on Nano Science and Technology (**ICONSAT2020**) organized by S. N. Bose National Centre for Basic Sciences, India during March 5-7, 2020
7. 6th International Conference on Advanced Nanomaterials and Nanotechnology (**ICANN2019**) held at Indian Institute of Technology Guwahati, Assam, India during December 18-21, 2019
8. 2nd IEEE International Conference on Power Electronics, Intelligent Control and Energy Systems (**ICPEICES2018**) held at Delhi Technological University, India during October 22-24, 2018
9. 5th International Conference on Advanced Nanomaterials and Nanotechnology (**ICANN2017**), held at Indian Institute of Technology Guwahati, Assam during December 18-21, 2017

Short Term Courses/Workshops/Seminars

1. **RSC Desktop Seminar Lectureship with EES (Joseph Hupp and Yana Vaynzof)** organized by RSC Publishing Webinars on March 31, 2021.
2. **Out in the cold: CryoTEM** organized by Jeol on January 12, 2021.

3. **6th National Workshop on MEMS/NEMS and Theranostic Devices (NWNTD2018)** organized by Centre for Nanotechnology, IIT Guwahati, Assam during December 1-3, 2020.
4. **Nature Nano – High Resolution AFM Imaging for Polymer Science** organized by Database Group @ Springer Nature on October 28, 2020.
5. **Research level understanding and Hands-on Training on SCAPS-1D for the TCAD designing of solar cells** organized by Chitkara University Punjab during September 22-25, 2020.
6. **International Day of Light (IDL-2020)** organized by IEEE Photonics Society and SPIE student chapters, Department of Physics, IIT Guwahati on May 16, 2020.
7. **5th National Workshop on MEMS/NEMS and Theranostic Devices (NWNTD2019)** organized by Centre for Nanotechnology, IIT Guwahati, Assam during February 21-23, 2019.
8. **2-Day INUP Familiarization Workshop On Nanofabrication Technologies** organized jointly by National Institute of Technology Silchar and Indian Institute of Technology Bombay during January 28-29, 2019.
9. **4th National Workshop on MEMS/NEMS and Theranostic Devices (NWNTD2018)** organized by Centre for Nanotechnology, IIT Guwahati, Assam during February 26-28, 2018.
10. **Biomedical Device Technology: Quick look of Technologies** held at Indian Institute of Technology Guwahati on December 18, 2017.
11. **Vacuum Technology and its Application** in Optical Science organized by SPIE IIT Guwahati Student Chapter and Pfeiffer Vacuum Pvt. Ltd. In association with Department of Physics, IIT Guwahati on August 19, 2017 at IIT Guwahati.
12. **Flexible Electronics** organized by Samtel Center for Display Technologies (SCDT), Indian Institute of Technology Kanpur and Ministry of Electronics & Information Technology during July 03-08, 2017 at IIT Kanpur.
13. **3rd National Workshop on MEMS/NEMS and Theranostic Devices (NWNTD2017)** organized by Centre for Nanotechnology, IIT Guwahati, Assam during February 21-23, 2017.